UNIVERSITY OF CALIFORNIA, SAN DIEGO

Dynamics of Electron Transfer at the Localized-to-Delocalized Transition of Mixed Valency

A dissertation submitted in partial satisfaction of the requirements for the degree

Doctor of Philosophy in Chemistry

by

Starla Demorest Glover

Committee in charge:

Professor Clifford P. Kubiak, Chair
Professor Seth M. Cohen
Professor José Onuchic
Professor Kimberly A. Prather
Professor William C. Trogler

2011

The dissertation of Starla Demorest Glover is approved and it is in acceptable quality and form for publication on microfilm and electronically:

_____

_____

_____

_____

_____

Chair

University of California San Diego

2011

DEDICATION

This work is dedicated to my family
and friends who are no longer with me.

TABLE OF CONTENTS

LIST OF FIGURES

LIST OF TABLES

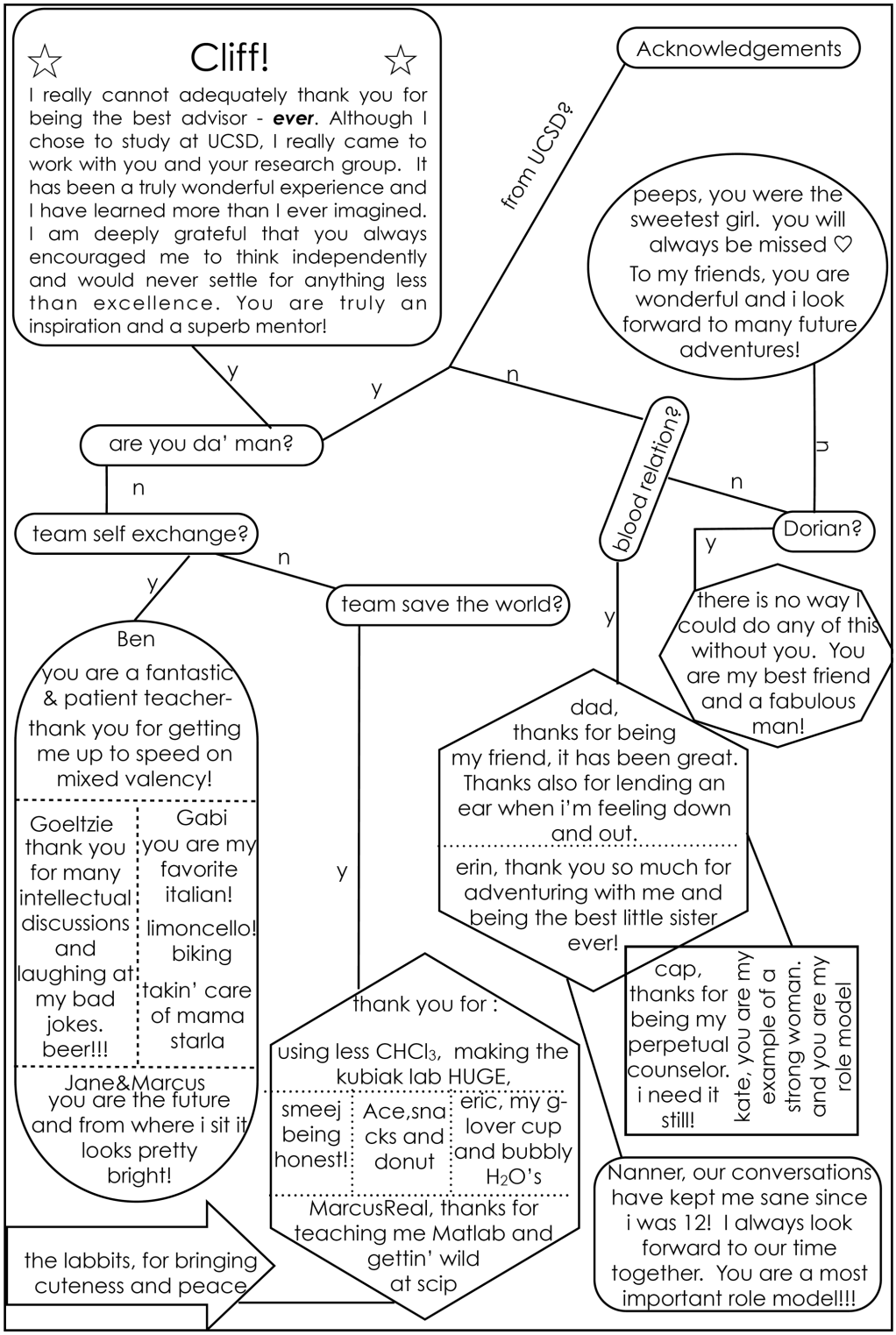
Cliff!
I really cannot adequately thank you for being the best advisor - ever. Although I chose to study at UCSD, I really came to work with you and your research group. It has been a truly wonderful experience and I have learned more than I ever imagined. I am deeply grateful that you always encouraged me to think independently and would never settle for anything less than excellence. You are truly an inspiration and a superb mentor!
Acknowledgements
from UCSD?
peeps, you were the sweetest girl. you will always be missed ♡
To my friends, you are wonderful and i look forward to many future adventures!
y
y
n
are you da' man?
n
blood relation?
n
Dorian?
y
team self exchange?
n
y
team save the world?
y
there is no way I could do any of this without you. You are my best friend and a fabulous man!
Ben
you are a fantastic & patient teacher- thank you for getting me up to speed on mixed valency!
dad, thanks for being my friend, it has been great. Thanks also for lending an ear when i'm feeling down and out.
erin, thank you so much for adventuring with me and being the best little sister ever!
Goeltzie thank you for many intellectual discussions and laughing at my bad jokes. beer!!!
Gabi you are my favorite italian! limoncello! biking takin' care of mama starla
Jane&Marcus you are the future and from where i sit it looks pretty bright!
y
thank you for :
using less $CHCl_3$, making the kubiak lab HUGE,
smeej being honest!
Ace,snacks and donut
eric, my g-lover cup and bubbly H_2O's
MarcusReal, thanks for teaching me Matlab and gettin' wild at scip
cap, thanks for being my perpetual counselor. i need it still!
kate, you are my example of a strong woman. and you are my role model
Nanner, our conversations have kept me sane since i was 12! I always look forward to our time together. You are a most important role model!!!
the labbits, for bringing cuteness and peace

Specific Chapter Acknowledgements:

Chapter 2: This chapter is derived from two published manuscripts; S.D. Glover, B.J. Lear, J.C. Salsman, C.H. Londergan, C.P. Kubiak "Electron transfer and the Class II/III borderline of mixed valency: dependence of rates on solvent dynamics and observations of a localized to delocalized transition in freezing solvents" *Philosophical Transactions of the Royal Society A*, **2008**, *366*, 177-185, and B.J. Lear, S.D. Glover, J.C. Salsman, C.H. Londergan, C.P. Kubiak " Solvent dynamical control of ultrafast ground state electron transfer: implications for class II/III mixed valency" *Journal of the American Chemical Society*, **2007**, *129*, 12772-12779.

Chapter 3: This chapter is a full reproduction of published material from "Persistence of the three-state description of mixed valency at the localized-to-delocalized transition." *Journal of the American Chemical Society*, **2011**, *accepted* by S.D. Glover, C.P Kubiak.

VITA

2005	Bachelor of Science with Honors in Chemistry Portland State University
2007	Master of Science in Chemistry University of California, San Diego
2005-2006	Teaching Assistant Department of Chemistry and Biochemistry University of California, San Diego
2005-2011	Research Assistant University of California, San Diego
2011	Doctor of Philosophy in Chemistry University of California, San Diego

PUBLICATIONS

S.D. Glover, C.P Kubiak "Persistence of the three-state description of mixed valency at the localized-to-delocalized transition." *Journal of the American Chemical Society*, **2011**, *accepted*

J.C. Goeltz, S.D. Glover, J. Hauk, C.P. Kubiak "Basic ruthenium acetate and mixed valence derivatives" *Inorganic Synthesis*, **2011**, *35*, 156-159.

S.D. Glover, J.C. Goeltz, B.J. Lear, C.P. Kubiak "Inter- or intramolecular electron transfer between ruthenium clusters: we'll cross that bridge when we come to it" *Coordination Chemistry Reviews*, **2010**, *254*, 331-345.

B. Bechlars, D.M. D'Alessandro, D.M. Jenkins, A.T. Iavarone, S.D. Glover, C.P. Kubiak, J.R. Long "High-spin ground states via electron delocalization in mixed-valence imidazolate-bridged divanadium complexes" *Nature Chemistry*, **2010**, *2*, 362-368.

P.A. Dreyse, M.A. Isaacs, P.E. Iturriaga, D.A. Villagra, M.J. Aguirre, C.P. Kubiak, S.D. Glover, J.C. Goetlz "Electrochemical preparation of conductive films of tetrapyridylporphyrins coordinated to four $[Ru(5\text{-}NO_2\text{-}phen)_2Cl]^+$ groups" *Journal of Electroanalytical Chemistry*, **2010**, *648*, 98-104.

S.D. Glover, J.C. Goeltz, B.J. Lear, C.P. Kubiak "Mixed Valency at the Nearly Delocalized Limit: Fundamentals and Forecast" *European Journal of Inorganic Chemistry*, **2009**, *48*, 4763-4767.

S.D. Glover, B.J. Lear, J.C. Salsman, C.H. Londergan, C.P. Kubiak "Electron transfer and the Class II/III borderline of mixed valency: dependence of rates on solvent dynamics and observations of a localized to delocalized transition in freezing solvents" *Philosophical Transactions of the Royal Society A*, **2008**, *366*, 177-185.

B.J. Lear, S.D. Glover, J.C. Salsman, C.H. Londergan, C.P. Kubiak " Solvent dynamical control of ultrafast ground state electron transfer: implications for class II/III mixed valency" *Journal of the American Chemical Society*, **2007**, *129*, 12772-12779.

ABSTRACT OF THE DISSERTATION

Dynamics of Electron Transfer at the Localized-to-Delocalized Transition of Mixed Valency

by

Starla Demorest Glover

Doctor of Philosophy in Chemistry

University of California, San Diego 2011

Professor Clifford P. Kubiak, Chair

Investigations into the dynamics of picosecond electron transfer in a series of mixed valence systems of the type $[Ru_3(\mu_3\text{-}O)(OAc)_6(py)(CO)–(\mu_2\text{-}BL)–Ru_3(\mu_3\text{-}O)(OAc)_6(py)(CO)]^{-1}$, where BL = 1,4-pyrazine or 4,4'-bipyridine and py = 4-dimethylaminopyridine, pyridine, or 4-cyanopyridine are described. Solvent and temperature dependence into the rate of ground state intramolecular electron transfer is probed by infrared analysis of ν(CO) bandshapes where simulated rate constants yield to rates ranging from 4×10^{11} to 3×10^{12} s^{-1}. Correlations between rate constants and solvent properties including solvent reorganization energy, optical and static dielectric constants, microscopic solvent polarity, viscosity, principal rotational moments of inertia, and solvent dipolar relaxation times, have been examined. Correlations revealed a marked lack of dependence on electron transfer rates with respect to solvent thermodynamic parameters, and a strong dependence on solvent dynamic parameters. This is consistent with electron transfers having very low activation barriers that approach zero. Temperature dependent studies revealed electron transfer rates accelerated as the freezing points of solvent solutions were

approached with a sharp increase in the rate of electron transfer upon freezing. This has been attributed to a localized-to-delocalized transition in these mixed valence ions at the solvent phase transition. This non-Arrhenius behavior is explained in terms of decoupling the slower solvent motions involved in the frequency factor, ν_N, which weights faster vibrational promoter modes that increase the value of ν_N. Solvent and temperature dependence of optically induced intramolecular electron transfer is probed by analysis of intervalence charge transfer bands in NIR spectra. The application of a semi-classical three-state model for mixed valency best describes the electronic spectra wherein is the appearance of two intervalence bands; a band which has metal-to-metal-charge-transfer character and another having metal-to-ligand-charge-transfer character. This three-state model fully captures the observed spectroscopic behavior where the MBCT transition increases in energy and the MMCT band decreases in energy as electronic communication increases through the series of mixed valence ions. The solvent and temperature dependence of the MBCT and MMCT electronic transitions is found to persist as coalescence of infrared vibrational spectra suggest ground state delocalization on the vibrational timescale. The solvent and temperature dependence of the MBCT and MMCT electronic transitions defines the mixed valence complexes as lying at the borderline of delocalization. Fine tuning the electronic coupling in the series of dimers has allowed for the resolution of a full Class II, early Class II/III, late Class II/III to Class III systems and the influence of solvent dynamics in each regime. These investigations have prompted the redefinition of borderline Class II/III mixed valency to account for outer sphere (solvent) contributions to electron transfer; in nearly delocalized systems, solvent dynamics localized otherwise delocalized electronic ground states. Further, studies explore the origins and dynamics behind spectral coalescence of vibrational ν (CO) bandshapes in [$Ru_3(\mu_3$-

O)(OAc)$_6$(py)(CO)–(μ_2-BL)–Ru$_3$(μ_3-O)(OAc)$_6$(py)(CO)]$^{-1}$ systems and a picosecond isomerization in square pyramidal Ru(S$_2$C$_4$F$_6$)(P(C$_6$H$_5$)$_3$)$_2$(CO) system.

Chapter 1

Electron transfer in the nearly delocalized regime

1.1 Introduction

Electron transfer is everywhere. It is ubiquitous in biological, physical, and chemical processes. Photosynthesis and respiration are two very important examples of essential life processes driven by electron transfer reactions. Also, all chemical reactions that involve bond breaking or bond forming must manage the movement of one or more electrons. Electrons are the smallest and most negative participants of every chemical reaction, and are often glossed over in many mechanistic descriptions, but they are always involved.

The study of electron transfer reactions is of widespread interest in the scientific community today. One eminently important example of is the study of solar energy conversion.[1-7] Plants are the most efficient terrestrial solar energy converters, having had millions of years to evolve the best light energy to chemical energy scheme - photosynthesis. The photosynthetic cycle involves many consecutive electron transfer reactions[3] to convert water and carbon dioxide to sugar and dioxygen. Having a thorough understanding of the kinetics and mechanics of the electron transfer

reactions involved in natural photosynthetic systems will lead to greater efficiency in the design of manmade solar energy converters.[1]

Electron transfer chain reactions in natural systems are very complex, involving multiple photon capture and subsequent electron transfer events.[3] Before such mechanisms can be understood in larger systems, simpler examples must be studied in order to grasp the fundamentals of electron transfer. In the 1950's, Rudolph A. Marcus laid the foundation for electron transfer theory,[8,9] of which the earliest studies were on very simple exchange reactions involving isotopically labeled metal ions in aqueous solution,[10] where no bonds are formed or broken. These initial studies opened wide the field of electron transfer,[11] and created a language with which scientists could communicate about electron transfer reactions. There is a body of exciting literature available covering the many aspects of electron transfer theory that cannot all be covered here.[12-19] This chapter serves as an introduction to the concepts of electron transfer theory, in order to frame the concepts appearing in later chapters.

1.2 Marcus-Hush Theory: kinetics and thermodynamics of electron transfer

The simplest form of an electron transfer reaction is one where an electron is traded between two identical sites, where the only distinguishing characteristic between the two sites is their difference in charge. One such electron transfer reaction can be represented by $D^- + A \rightarrow D + A^-$, where D^- is the electron donor and A is the electron acceptor. In Rudy A. Marcus' preeminent initial studies the electron transfer was between two aqueous metal ions[11]

$$Ce^{3+} + {}^*Ce^{4+} \rightarrow Ce^{4+} + {}^*Ce^{3+}$$

where the reaction can be observed by virtue of the isotopic labeling denoted by "*".

This reaction represents a bimolecular intermolecular electron transfer between two units. Many electron transfer reactions occur by an intramolecular pathway, and such an example is given in Figure 1.1 for methyl viologen.[20] This is a unimolecular reaction of the form $DA \rightarrow D^+A^-$.

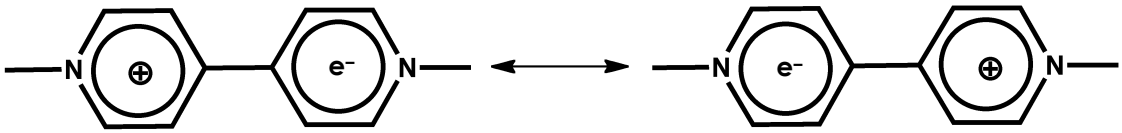

Figure 1.1 The stable form of methyl viologen, or paraquat, is a dication, methyl viologen dichloride. A singly reduced methyl viologen is a monocation where an unpaired exchanging electron moves between the two halves of the molecule.

In both intramolecular and intermolecular electron transfer reactions, the free energies of the donor and acceptor states can be reasonably approximated by a simple harmonic oscillator along a reaction coordinate.[16,19] Figure 1.2a shows free energy surfaces for the electron donor, G_d, and electron acceptor, G_a.

$$G_d = \lambda x^2 \qquad (1)$$

$$G_a = \lambda(x-1)^2 + \Delta G_0 \qquad (2)$$

The reaction coordinate, x, or nuclear coordinate encompasses all the atomic coordinates, bond angles, and outer sphere coordinates that are involved in the electron transfer reaction. In a symmetric electron transfer system the minima of G_d and G_a have the same energy, and the standard free energy difference, ΔG_0, is equal to zero.[21] When donor and acceptor are asymmetric, ΔG_0 will have a non-zero value. All the electron transfer systems considered in this dissertation are symmetric, and as such, the symmetric case is considered throughout. The most probable initial site for an electron on the donor coordinate is at the minimum G_d. From this picture there are two pathways for an electron to transfer from the donor to acceptor surface. Introducing a sufficient amount of optical energy to the system will vertically excite the

electron to the acceptor surface. This type of electron transfer is often termed "optically induced" electron transfer, as the energy provided for the electron excitation is provided by light.[11] Since electron excitation is instantaneous with respect to nuclear motion, the transferred electron exists in such a state that nuclear coordinates will be in an unfavorable, high energy, configuration.[22] Subsequent vibrational relaxation and outer sphere reorientation will land the electron in the minimum of G_a. The energy required for optically induced electron transfer is termed the total reorganization energy, and is denoted λ. Another manner in which the electron can transfer from surface is by a rearrangement of inner sphere and outer sphere coordinates such that the donor and acceptor have identical configurations and the electron can then pass from G_d to G_a without a change in energy. This type of electron transfer is termed "dark" or thermal electron transfer, because dynamic

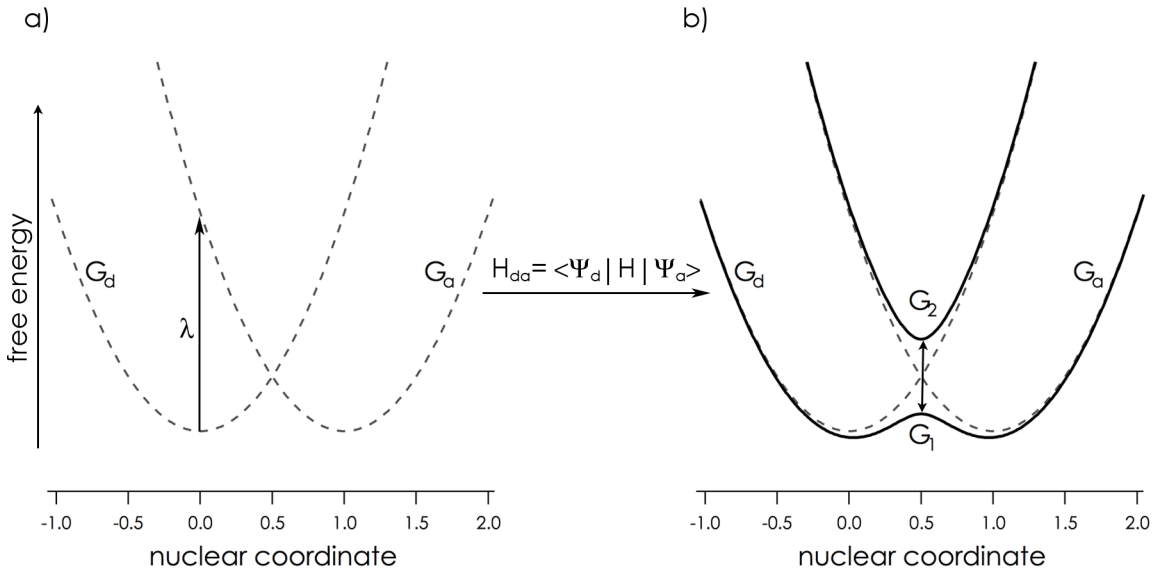

Figure 1.2 a) Potential energy surfaces for electron donor, G_d, and electron acceptor, G_a. λ is termed the total reorganization energy, and is equal to the optical excitation energy. This arrangement is in the absence of electronic coupling and the surfaces are diabatic. **b)** When electron donor and acceptor wavefunctions overlap, electronic coupling produces two new adiabatic surfaces; the ground state surface G_1 and an excited state G_2. The separation between surfaces in the cross over region, x = 0.5, is equal to $2H_{da}$, or twice the electronic coupling constant.

fluctuations of the system promote electron transfer.[11] For electron transfer to occur, the nuclear configuration of the reactants and outer sphere media must distort from the equilibrium state (minimum of G_d) such that there is no difference in energy between donor and acceptor. In Figure 1.2a this nuclear configuration is accessed at the intersection of G_d and G_a, where the nuclear coordinate is equal to 0.5. Figure 1.2a shows the case where donor and acceptor are non-interacting (i.e the donor and acceptor are devoid of electronic communication). In this configuration, potential energy surfaces are called diabatic, literally a "two bath" case.

In the case where the electron donor and electron acceptor can interact electronically, thier wavefunctions can mix, leading to electronic communication.[16,23] The electronic coupling matrix element, H_{da}, physically describes the degree of wavefunction overlap between donor and acceptor and serves to quantify the degree of electronic communication in a donor acceptor (DA) system. Depicted in Figure 1.2b are potential energy surfaces for a DA system where electronic coupling is present. These potential energy curves are called adiabatic surfaces. By solving the secular determinant of the 2 x 2 matrix for the eigenvalue, E,

$$\begin{vmatrix} G_d - E & H_{ad} \\ H_{da} & G_a - E \end{vmatrix} = 0 \qquad (3)$$

the eigenvalues, G_1 and G_2, of the electronically coupled system can be obtained.[15,16]

$$G_1 = \frac{1}{2}\{(G_d + G_a) - [(G_d - G_a)^2 + 4H_{da}^2]^2\} \qquad (4)$$

$$G_2 = \frac{1}{2}\{(G_d + G_a) + [(G_d - G_a)^2 + 4H_{da}^2]^2\} \qquad (5)$$

The difference in energy between G_1 and G_2 at the intersection, x = 0.5, is equal to $2H_{da}$ and represents twice the energetic stabilization gained by the electronically coupling the diabatic surfaces. It can be seen from Figure 1.2b that H_{da} creates a favorable situation for the G_1 state as it becomes stabilized in energy (compared to the diabatic

surfaces). Increasing the electronic coupling in an electron transfer system has a number of implications for the adiabatic free energy surfaces. As G_1 becomes more stabilized in energy, the minima of donor and acceptor sites will move closer together along the nuclear coordinate toward x = 0.5 by $1/2 * \left[1 \pm [1 - 4(H_{da}/\lambda)^2]\right]$, and the activation barrier, ΔG_λ^* will decrease in energy from $\Delta G_\lambda^* = \lambda/4$ (diabatic) to $\Delta G_\lambda^* = [(\lambda - 2H_{da})^2/4\lambda]$ (adiabatic). Additionally, as H_{da} increases G_2 will increase in energy, thus the difference in energy between the adiabatic surfaces increases by $(G_2 - G_1) = [(G_a - G_d)^2 + 4H_{da}^2]^{1/2}$.[16,19] Lowering the activation barrier will have the important consequence of allowing the dark, ground state reaction to proceed with less resistance. In the same turn, because there is greater separation of adiabatic surfaces, the optically induced electron transfer which proceeds from G_1 to G_2 will require more energetic light to transfer the electron.

In the general expression for the rate of electron transfer reaction, is given by

$$k_{et} = \kappa_{el} v * exp[-\Delta G^*/RT] \qquad (6)$$

where v is a pre-exponential factor and κ_{el} is the electronic transmission coefficient.[10,19] The electronic transmission coefficient, termed κ_{el}, takes into account the probability of an electron transfer reaction occurring once the system attains coordinates of the intersection region (i.e., x = 0.5).[19,24] For a weakly coupled diabatic system $\kappa_{el} < 1$, meaning that for a system whose nuclear coordinate crosses the intersection region, the electron has some probability of remaining on the G_d surface and *not* transferring to G_a. In contrast, for an increasingly adiabatic system, $\kappa_{el} \rightarrow 1$, meaning that once the system reaches the intersection region, the probability of electron transfer from the reactant state to the product state is close to unity. When electron transfer is adiabatic, κ_{el} is taken to be equal to one.

The nuclear frequency factor, v, also needs to be considered separately for diabatic and adiabatic systems. In weakly electronically coupled systems v depends

on the electron hopping (or tunneling) frequency, which is proportional to $H_{da}^2/\sqrt{\lambda}$.[19] In strongly coupled systems, the nuclear frequency factor is referred to as v_N, and depends on nuclear coordinate frequencies.[24] The nuclear frequency factor is composed of nuclear modes that participate in the system reorganization through the intersection region of the free energy surface. Specifically, these modes are the weighted intramolecular modes (inner sphere) and solvent modes (outer sphere), and v_N can be represented by the following expression[24]

$$v_N = [\sum_i v_i^2 E_i / \sum_i E_i]^{\frac{1}{2}} \qquad (7)$$

where the term v_i corresponds to a single harmonic frequency of a nuclear mode that contributes to the activation barrier.

When the activation energy is given in terms of electronic coupling and reorganization energy, $\Delta G_\lambda^* = [(\lambda - 2H_{da})^2/4\lambda]$,[21] and substitution into the rate expression gives:

$$k_{et} = \kappa_{el} v_N * exp[-(\lambda - 2H_{da})^2/4\lambda RT] \qquad (8)$$

In this form of the rate expression it can be deduced that when $H_{da} \rightarrow \lambda/2$ the activation barrier approaches zero and the exponential portion of the rate expression approaches unity.[16] In this limit the rate of electron transfer depends solely on the pre-exponential nuclear frequency factor. The weighting in this equation implies that under the proper conditions, faster modes (i.e., vibrations) will dominate v_N, and by extension, k_{et}.[24] Typical solvent frequencies range from 10^{12} – 10^{13} s^{-1} while vibrational frequencies are from 10^{12} – 10^{15} s^{-1} leading to the approximation that v_N ~ 10^{13} s^{-1}.[16] The weighting of different frequency modes has implications for electron transfer rates.[25-28] This aspect of electron transfer theory will be explored in more detail in Chapters 2 and 3.

The last parameter in the rate expression to discuss is λ, the total reorganization energy. Where the pre-exponential portion of the rate expression describes the frequency dependence of electron transfer rates, λ accounts for the energetic requirement of reconfiguring the nuclear coordinates to favorable positions following electron transfer.[10] As has already been discussed, the players in the simplest electron transfer reaction are the surrounding solvent and molecular coordinates, and as such the total reorganization energy can be separated into inner sphere and outer sphere contributions

$$\lambda = \lambda_i + \lambda_o \tag{9}$$

where λ_i and $\lambda_o$describe the inner sphere and outer sphere reorganization energies, respectively.[21] The vibrational term, λ_i, is realized by considering the force constants that arise upon changing inner sphere mode coordinates from donor and acceptor species.[19,29,30]

$$\lambda_i = \sum_j \frac{{k_j}^D k_j^A}{{k_j}^D + k_j^A} ({Q_j}^D - {Q_j}^A)^2 \tag{10}$$

Here, ${k_j}^D$ and k_j^A are the force constants of a jth vibrational mode, and $({Q_j}^D - {Q_j}^A)^2$ accounts for the change in bond lengths and angles between donor and acceptor.

There are several theories that describe λ_o, but the most widely applied, by far is, based upon the Marcus dielectric continuum model of solvation.[10] In this model the outer sphere reorganization energy is described electrostatically by

$$\lambda_o = \Delta e^2 \left(\frac{1}{\varepsilon_{op}} - \frac{1}{\varepsilon_s}\right) \int (D_d - D_a)^2 \, d\tau \tag{11}$$

where Δe^2 is the charge transferred, D_d and D_a describe radial separation of donor and acceptor, and ε_{op} and ε_s are the optical and static dielectric constants of the solvent. The term $\left(\frac{1}{\varepsilon_{op}} - \frac{1}{\varepsilon_s}\right)$ assumes a dielectric continuum in which multiple solvent dipoles are treated as a whole, to create a dipolar gradient about the electron transfer system.[21]

This description greatly simplifies the treatment of the outer sphere, as each solvent molecule's dipole (and there may be a great many) need not be considered individually. While the continuum model for solvation has been applied successfully for many electron transfer systems, as will be demonstrated by work presented in this dissertation, this description is not valid for systems exhibiting pre-exponentially determined rates of electron transfer.[25-27]

There are a multitude of known electron transfer reactions, and it is in the best interest of people who study them to understand their behavior in the face of changing electronic (H_{da}), energetic (λ), and pre-exponential parameters. The next section describes a systematic methodology by which all electron transfer systems can be classified.

1.3 Mixed valence classifications

Many systems undergoing electron transfer reactions can be called mixed valence complexes, as by definition, a mixed valence complex is one in which there are two or more sites that differ in electronic charge. In reality there exists a spectrum of electron transfer reactions spanning the diabatic limit to the strongly adiabatic limit. A methodology to categorize electron transfer reactions is desirable and will lead to increased general understanding. The currently accepted classification scheme was devised by Robin and Day in 1967, which assigns mixed valence complexes based on their optical and electronic properties.[23,31] The classification scheme is built upon the principal that there are discernible differences in electronic and optical behavior of an electron transfer system when electronic coupling is some critical proportion of the reorganization energy.

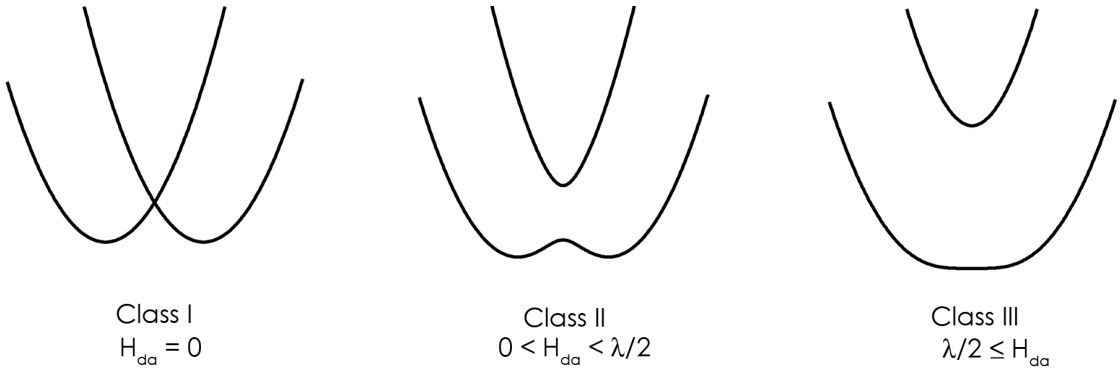

Figure 1.3 Potential energy surfaces for two-state mixed valence complexes with increasing electronic communication. When there is no electronic communication present, a mixed valence system is considered Class I. With moderate electronic coupling a mixed valence system is Class II. Class III systems are delocalized over the two states.

Figure 1.3 summarizes the three general classes of mixed valency.[16] A Class I complex is considered to possess no electronic coupling and exists in the diabatic limit. A Class I system is entirely "charge localized" and an electron existing on the donor surface will have no awareness of the acceptor surface. A Class II complex is considered moderately to strongly coupled with $0 \leq H_{da} \leq \lambda/2$. Class II complexes are also considered charge localized species, but depending on the degree of electronic communication, the localization is associated with some timescale. Class III mixed valence complexes are those for which $H_{da} \geq \lambda/2$, wherein G_1 has collapsed to a single well and an electron can experience unhindered movement between donor and acceptor sites. In this configuration the electronic charge is averaged over the two sites and an exchanging electron is considered to be fully delocalized.

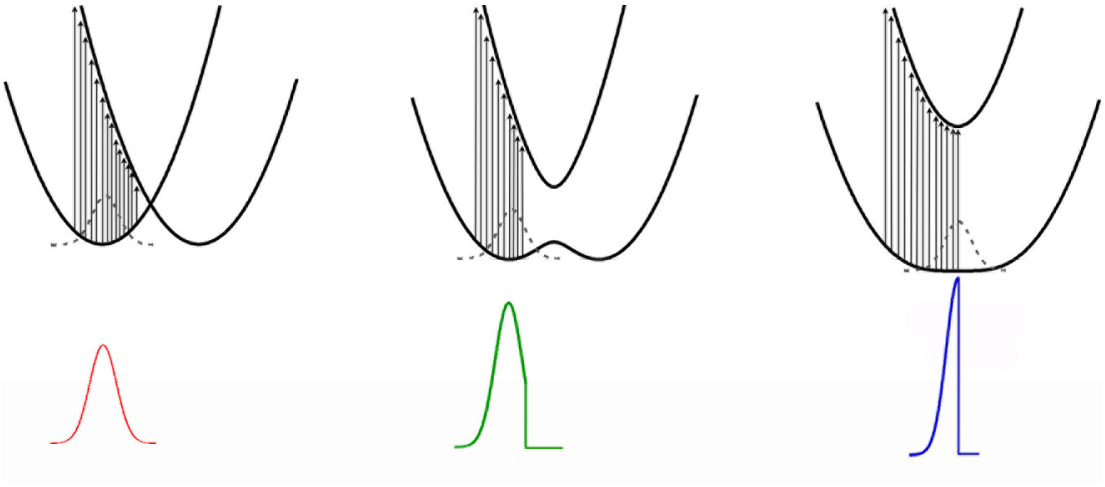

Figure 1.4 The effect of increased electronic coupling (left to right) on energy, intensity and bandshape for the IVCT bands (shown beneath the corresponding potential energy surface). A Boltzmann distribution is assumed for the population in G_1 and is represented by the dotted Gaussian lineshape. With increased electronic communication IVCT bands blue-shift, intensify, and display a cutoff on the low energy side. The shape of the ground state adiabatic surface will greatly affect the shape of the IVCT band.

The potential energy surfaces like those shown in Figures 1.2 and 1.3 can be used to predict optical transition bandshape (also termed intervalence charge transfer band or IVCT band) behavior for each mixed valence class. Assuming a Boltzmann distribution in quantum vibrational levels for a set of mixed valence systems in the donor configuration, a manifold of optical transitions will give rise to an IVCT band.[16] In the face of changing H_{da} or λ, IVCT transitions of different energies, intensities and bandshapes will be observed.[16] Qualitatively depicted in Figure 1.4 are changes in bandshapes and energies that will be observed as H_{da} increases. It can be seen that an increase in electronic coupling will cause bandshape maxima to experience a hypsochromic shift in energy. What is not intuitive from the Figure 1.4 is that as H_{da} increases, intervalence charge transfer bands will intensify when the ground and excited state potential energy surfaces (PES) experience greater energy separation, $(G_2 - G_1)$. This effect can be understood by considering overlap of ground and excited

state vibrational wavefunctions, (i.e. the Franck-Condon overlap integral).[32] With greater electronic communication, G_1 is more parabolic in shape and the ground state Boltzmann population will have more favorable vibrational wavefunction overlap with excited state vibrational levels, thus there is a greater probability of an excited electron populating the excited state surface G_2, which in turn leads to increased IVCT intensity.[17,33] Another consequence of increasing electronic coupling is that intervalence charge transfer band shapes will display an increasingly pronounced asymmetry by a "cutoff" on the low energy side of the bandshape. The origin of the cutoff bandshape is readily apparent from PES of the Class III system, where the vertical energy difference between the minima of G_1 and G_2 is the smallest possible. Analysis of the IVCT optical transition can thus be extremely informative with regard to the shape of the underlying adiabatic potential energy surface.

In the same year that mixed valence classifications were realized, Noel S. Hush developed a formalism which accounts for the key relationship between IVCT bandshapes and the implicit underlying potential energy surface that depends on the electronic coupling.[17,33] The relationship between optical properties and electronic coupling is given by

$$\varepsilon_{max} = \frac{2.36\times10^{3} H_{da}^{2} r_{da}^{2}}{\nu_{max} \nu_{1/2}^{0}} \qquad (12)$$

Rearranging the above equation gives the widely applied Mulliken-Hush expression for electronic coupling in terms of spectral quantities.

$$H_{da} = 2.06\times10^{-2} \frac{\left(\nu_{max} \varepsilon_{max} \nu_{1/2}^{0}\right)^{\frac{1}{2}}}{r_{da}} \qquad (13)$$

Here ν_{max} is the energy of the IVCT band maximum, ε_{max} is the molar absorptivity, and $\nu_{1/2}^{0}$ is the full width at half-maximum. The quantity r_{da} defines the electron transfer distance. The beauty of this equation lies in its simplicity; most of the necessary values can be obtained directly by analysis of the IVCT bandshapes. There is great utility in this

relationship, for it has been applied successfully to many mixed valence systems. However, the bandshape behavior illustrated in Figure 1.4 shows that there is clearly a limit to its ability to predict electronic coupling constants.[16] Specifically, the above equation assumes that the full-width at half max, $v_{1/2}^{0}$, is derived from a Gaussian bandshape. As can clearly be seen from Figure 1.4, significant electronic coupling causes the bandshape to lose width on the low energy side, and at the Class III limit, the width of the bandshape appears as one half of a full Gaussian width. As a result of this cutoff effect the value of H_{da} is underestimated when a Class II complex approaches the Class III limit. Another complication with this equation concerns the determination of the electron transfer distance, r_{da}. In the completely diabatic case, the exchanging electron must traverse from the minimum donor nuclear coordinate to the minimum acceptor nuclear coordinate. This distance, r_{da}, can be quantified as the hard sphere radial geometric distance between the donor and acceptor orbitals.[17] In the case of electronic coupling, however, donor and acceptor wavefunctions can mix. New molecular orbitals are formed that in principal reduce the electron transfer distance between donor and acceptor, making r_{da} a very difficult parameter to quantify.[23] Stark spectroscopy has proven useful in surmounting this difficulty and has made possible the determinination of effective electron transfer distances.[34] For systems which are highly electronically coupled, but not yet fully delocalized, the Mulliken-Hush relationship cannot be reliably used to predict the electronic coupling constant. Although there is great utility in the application of this equation, it is not possible to strictly identify values for H_{da} in a strongly coupled Class II system. The answer, by comparison, is satisfyingly simple in the Class I and Class III case: in the Class I limit, the IVCT energy is equal to λ, and $H_{da} = 0$; in the Class III limit the IVCT energy is $\lambda = 2H_{da}$.[16,19] These relationships become clear when the free

energy equations (insert numbers) are solved with the above conditions, and can be understood by the potential energy curves in Figures 1.2 and 1.3.

Despite these limitations in the determination of H_{da}, some general guidelines concerning the mixed valence classes can be outlined by optical and electronic behavior. From Marcus theory we have also anticipated the solvent contributions to the reorganization energy, so the solvent dependence may be included in the discussion.[16,19,21,23] In Class II systems the exchanging electron and solvent are localized with respect to nuclear motion.[23] This means that solvent and electron motion are slower than nuclear motions and electron transfer is within the thermodynamic regime (rather than the pre-exponential regime). This predicts that optical transitions will depend on the solvent environment as given in the equation for λ_o. In a Class III system, electron exchange is so "fast" that it is delocalized and solvent motion will appear averaged with respect to the electron motion.[23] Therefore, in a delocalized system, the electron motion is taken to be solvent independent by virtue of the electron transfer being entirely under pre-exponential control. In reality there are no discrete cutoffs between Class I, Class II and Class III, rather there exists a continuum of mixed valency. In particular, the transition between Class II and Class III complexes has presented a persistent problem in the mixed valency community for over thirty years.[15,16,23,28]

An additional classification, Class II/III, has been proposed for complexes that are in localized-to-delocalized limbo.[23] The quintessential example of a complex residing near this borderline is the Creutz-Taube ion,[13] $[(NH_3)_5Ru^{II}\text{-pz-}Ru^{III}(NH_3)_5]^{3+}$, where pz = pyrazine. The Creutz-Taube (C-T) ion was the first of many intentionally synthesized mixed valence complexes. The classification of the C-T ion by its optical, solvent and vibrational qualities proved to be *the* great challenge for the mixed valency community, as it took nearly 40 years to resolve the issue. The C-T system has been

investigated by electronic spectroscopy,[13] Stark spectroscopy,[34] resonance Raman spectroscopy,[12,35] and DFT.[36] These studies point to solvent independence, but strong interplay of symmetric bridging vibrational modes in electron propagation. The monumental effort to understand the C-T ion, which is today believed to be electronically delocalized with vibronically enhanced bridging ligand modes, substantially advanced the field of mixed valence chemistry.

The mixed valence research presented in this dissertation will focus on complexes with donor and acceptor units composed of Ru_3-μ^3-O cores bridged by pyrazine or 4,4'-bipyridine.[38] Electron transfer studies of these systems have proven a valuable resource for elucidating mixed valency through a Class II to Class III transition.[26]

1.4 Bridged trinuclear ruthenium clusters; an ideal system for investigations of ultrafast mixed valency

Complexes of the form $[Ru_3O(OAc)_6(CO)(py)\text{-}pz\text{-}Ru_3O(OAc)_6(CO)(py)]^-$, (pz = pyrazine and py = pyridyl) have been under investigation for the last 15 years largely because of their ultrafast electron transfer behavior.[39] A series of three complexes are shown in Figure 1.5 below. A brief account of their electronic, vibrational and optical behavior is given here to familiarize the reader with this particular mixed valence system.

The dimers of the trinuclear ruthenium clusters depicted in Figure 1.5 are neutral, but upon a single electronic reduction, form stable charge transfer complexes with overall −1 charge.[39] In this state the unpaired electron can be shared between the coupled Ru_3 clusters via the bridging pyrazine ligand. Electrochemical investigations can provide insight into the electronic character of these systems. In the anodic region **1** – **3** show concerted two electron oxidations, meaning that one

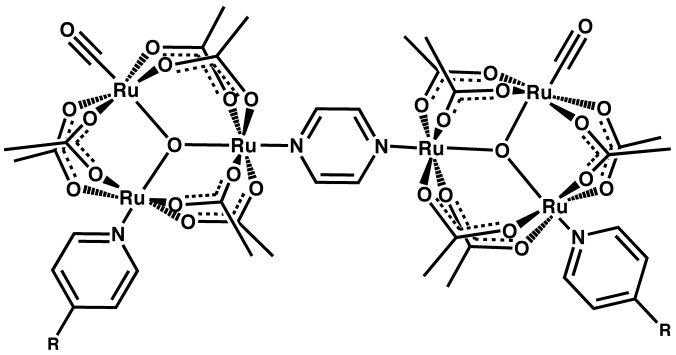

R = N(CH$_3$)$_2$ R = H R = CN
1 2 3

Figure 1.5 Dimers of ruthenium trimers with bridging ligand pyrazine and ancillary ligands: (**1**) 4-dimethylaminopyridine (dmap), (**2**) pyridine (py), and (**3**) 4-cyanopyridine (cpy). In the singly reduced mixed valence state an electron exchanges between $Ru_3O(OAc)_6$ units. In the neutral complex the formal oxidation states for both clusters are $Ru^{III}Ru^{III}Ru^{II}$.

electron is removed from each cluster at the same time as follows: $Ru_3^{III,III,II}$–BL–$Ru_3^{III,II,II}$ goes to $Ru_3^{III,III,III}$–BL–$Ru_3^{III,III,III}$ (0/+2 couple),and $Ru_3^{III,III,III}$–BL–$Ru_3^{III,III,III}$ goes to $Ru_3^{III,III,IV}$–BL–$Ru_3^{III,III,IV}$(+2/+4 couple). In contrast, the cathodic processes occurs in single electron steps that formally generate $Ru_3^{III,III,II}$–BL–$Ru_3^{III,II,II}$ (0/−1 couple) and subsequently $Ru_3^{III,II,II}$–BL–$Ru_3^{III,II,II}$ (−1/−2 couple).[39] This tells us that the two electrons are added sequentially to the dimer system. Comparing the different electrochemical splittings of cathodic peaks ($\Delta E_{1/2}$) is a qualitative measure of the strength of inter-cluster electronic communication.[39,40] That is, larger $\Delta E_{1/2}$ values indicate greater energetic stabilization of the singly reduced state, which is facilitated by better electronic coupling between the clusters. From the $\Delta E_{1/2}$ for the (-1/-2) couple for **1** (440 mV), **2** (380 mV), and **3** (250 mV)[39] in methylene chloride we learn that the effective electronic stabilization in the dimers is influenced by ancillary ligands. This is a type of remote ligand control of electronic coupling, and the fact that such a broad range in electrochemical behavior can achieved by simple substitution of ancillary ligands is quite remarkable. Variation of cluster ligands gives rise to the following conditions: (i) control of the favorable overlap between the Ru_3 cluster dπ-electron system and the bridging pz π^*

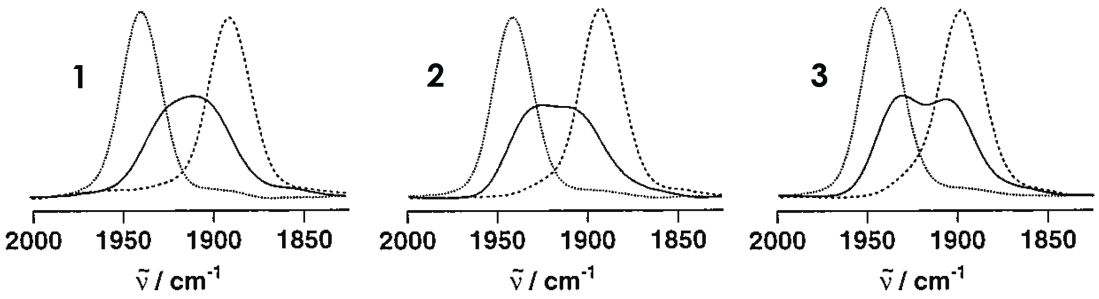

Figure 1.6 IR spectra of the ν(CO) region for complexes **1** – **3** obtained by spectroelectrochemistry in methylene chloride with 0.1 M TBAH (tetrabutylammonium hexafluorophosphate) as the electrolyte. The isovalent neutral and –2 states (dotted and dashed line, respectively) a single narrow bandshape is observed. The mixed valence state (solid line) of **1** displays a single broad band at an average of the neutral and doubly reduced band maxima. The extreme coalescence points to exchange of the unpaired electron on the vibrational timescale. The diminishing coalescence in **2**$^-$ and **3**$^-$ indicates relatively slower rates of electron exchange.

system, and (ii) the ability to raise or lower the energy of the Ru_3 cluster d-electron levels engaging the pz system by changing the electron donor/acceptor ability of the ancillary pyridyl ligand.[25] For complexes in Figure 1.5, the trend in increasing electron-donating ability of ancillary ligands is: cpy < py < dmap. The relevant Ru-dπ level is then closer to the pz π^* level in **1** than in **3**, which facilitates greater electronic communication.[25]

The carbonyl ligand on each trinuclear cluster presents an appealing vibrational spectroscopic probe for the behavior of these complexes in 0, -1, and -2 oxidation states. Each triruthenium cluster contains a carbon monoxide ligand that has a distinct stretching absorption, ν(CO) band, in the infrared (IR).[39] Because the Ru_3O core can shift electron density into the carbonyl via π-backbonding, the ν(CO) frequencies of these ligands are sensitive to the electronic environment on each cluster. Specifically, ν(CO) bands will shift to lower frequencies in the presence of greater electron density and higher frequencies in regions of depleted electron density. Figure 1.6 shows IR spectra of **1** – **3** in the neutral, –1, and –2 oxidation states.[41]

In the isovalent 0 and -2 states the carbonyls are expected to experience identical environments and a single narrow bandshape is observed at ~1950 cm^{-1} for a neutral dimer, and ~1880 cm^{-1} for the dianionic dimer. In the mixed valence (-1) state an electron can reside on either cluster. Were the electronic charge to be localized on one cluster, two bands of approximately one half intensity would be observed. Upon inspection of ν(CO) bands of mixed valence dimers, it can be seen that there is a broad and coalesced bandshape at the average of the neutral and doubly reduced band maxima.

These bandshapes are reminiscent of what is often observed by NMR spectroscopy in fluxional systems.[42] The difference in IR (vibrational frequencies) and NMR (radio frequencies) coalescence is a matter of timescale. The frequencies associated with vibrational spectroscopy are approximately 10^9 times faster than those of NMR spectroscopy. For bandshape coalescence to be observed in vibrational spectra of **1**$^-$ – **3**$^-$, the exchanging electron must be shared between the two clusters at or near the vibrational timescale, i.e. ~10^{12} s^{-1}.[39] IR spectra of singly reduced mixed valence dimers provides compelling evidence that electron transfer is on the vibrational timescale in the picosecond regime. Coalescence in vibrational spectra has also been observed in iron-tricarbonyl systems, where "turnstile" exchange of carbonyls leads to dynamically coalesced IR lineshapes.[43,44] Simulation of dynamically coalesced vibrational lineshapes can be achieved by using Bloch equations that have been suitably modified to account for the dipole moments of exchanging vibrators.[45] Bloch simulations yield exchange rate constants,[46] and analysis of **1**$^-$, **2**$^-$, and **3**$^-$ gives electron transfer rates of 2 × 10^{12} s^{-1}, 1.7 × 10^{12} s^{-1}, 1.1 × 10^{12} s^{-1}, respectively.[27] In the case of **1**$^-$, the fully coalesced bandshape would indicate that the exchanging electron is delocalized on the vibrational timescale. The ν(CO) band for **3**$^-$ is not fully averaged implying that it still exhibits some charge localization on the vibrational

timescale. These ultrafast rate constants point to the strong pre-exponential influence on electron transfer[47] and a very large degree of electronic coupling relative to the reorganization energy.[48]

Solvent and temperature dependent studies of **1**$^{-}$ – **3**$^{-}$ have revealed a marked sensitivity of electron transfer reaction rates to dynamic outer sphere promoter modes.[26,27,47] The rate of electron transfer can be affected simply changing the solvent in which we study a mixed valence dimer. For example, in acetonitrile **1**$^{-}$ has a k_{et} of 2.8 × 10^{12} s^{-1} while in hexamethylphosphoramide **1**$^{-}$ has a k_{et} of 0.66 × 10^{12} s^{-1}, about four times slower.[27] The study of many dimers in many different solvents revealed that solvent dynamics control rates of electron transfer when the activation barrier approaches zero.[26,27] Given what is known about dynamic contributions to v_N, this result is consistent with **1**$^{-}$ – **3**$^{-}$ and related systems undergoing pre-exponentially fast electron transfer.

Perhaps the most exciting discovery pertaining to nearly the character of the dimers was the effect on electron transfer when solvent dynamics are arrested.[26,27] Freezing the solvent reduced outer sphere dynamical contributions, by arresting their motion, and facilitated rate acceleration by promotion of electron transfer solely by inner sphere modes. A complementary study of the mixed valence behavior via optical excitation deepened our understanding of Class II/III borderline systems in that we were able to separate out the effect of solvent dynamics in early, middle and late borderline systems. Additionally, it became clear from optical studies that the bridging ligand contributes a viable electronic state and must be an important consideration in the overall description of systems like **1**$^{-}$ – **3**$^{-}$. The solvent and temperature dependence of ground and excited state electron transfer in these mixed valence systems will be discussed in greater detail in Chapters 2 and 3.

1.5 Necessity of a three state model of mixed valency

Until now, the discussion of **1**$^{-}$–**3**$^{-}$ has been from the perspective of a two-state donor-acceptor arrangement.[49] From Figure 1.5, it is apparent that a pyrazine bridge must be surmounted for an exchanging electron to traverse between the Ru_3O sites. The idea that bridging modes are of consequence in donor-bridge-acceptor systems has been explored in great detail with the C-T ion, where it was found that vibronic participation of symmetric pz modes promoted electron transfer.[12,14,50-52] The participation of bridging pyrazine normal modes has been investigated in mixed valence dimer systems to quantify the involvement of the bridging ligand.[53-55] The systematic variability in complexes **1**$^{-}$–**3**$^{-}$, allowed for studies of the role of vibronic contributions of specific bridging normal modes as electronic communication was tuned to nearly achieve delocalization. To this end, **1**$^{-}$–**3**$^{-}$ were interrogated by resonance Raman spectroscopy. Resonance Raman probes the symmetric vibrational profile of an optically excited molecule,[56] so mixed valence character can be followed by optically exciting the IVCT and following the enhancement of vibrational modes of pyrazine.[54] From these studies the following key insights were realized[25]: (i)there is an significant amount of electron density present on the bridging ligand in the mixed valence state and this density increases with electronic coupling, (ii)the symmetric ν_{8a} mode is an active player in the mediation of electron exchange because it can bring Ru clusters into closer proximity to bring about more favorable overlap conditions, (iii)the greater the electronic coupling in the system, the greater enhancement of vibronic coupling of bridge modes. The ν_{8a} mode appears at 1587 cm^{-1} which translates to a frequency of 4.8×10^{13} s^{-1}, and places an upper limit on how fast electron transfer can occur. This study verified that dynamic bridge modes are key players in nearly delocalized systems (as are the dynamic solvent modes) and that

a three-state description should be explicit in the mixed valence description of **1**$^{-}$–**3**$^{-}$ and related dimers.

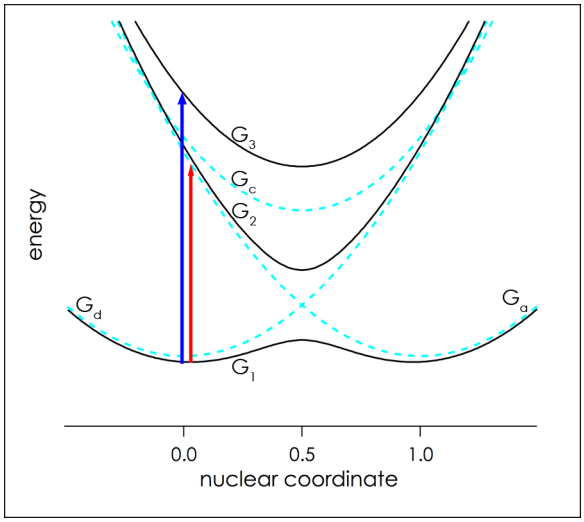

Figure 1.7 Potential energy surfaces for a three state donor-bridge-acceptor mixed valence system. Two electronic transitions to adiabatic surfaces are possible in the three state model: $G_1 \rightarrow G_2$ and $G_2 \rightarrow G_3$.

Electronic spectra of dimer systems also provide firm evidence in favor of a three-state over a two-state picture.[39] The two-state model predicts a single intervalence charge transfer band (Figure 1.4). However, inspection of the NIR region of electronic spectra of mixed valence dimer systems clearly shows the presence of two new intensities (~10 000 cm^{-1} and ~7000 cm^{-1}) that are not present in neutral dimer spectra. The appearance of two bands implies the existence of two states to which a ground state electron may transfer. Figure 1.7 shows diabatic and adiabatic potential energy surfaces for a three state system where a state, G_c, has been included for the bridge.[16] Vertical transitions from the ground state to the acceptor based state or the bridge state account for the observation of two IVCT bands. By solvent and temperature dependence studies of the IVCT behavior, we found that a vibronic three-state model cannot reconcile the solvent dynamic dependence that so heavily influences these borderline systems. Potential energy analysis, however, allows us to

include dynamical considerations in the energetic landscape. These concepts are given due consideration in Chapter 3.

1.6 Conclusions

To date there are a limited number of mixed valence systems suitable for the study of Class II/III behavior. Ruthenium dimer-of-trimer systems are fortuitously situated in the mixed valency continuum to address the issues of localized to delocalized mixed valency. The purpose of this body of work is to provide a framework by which Class II/III mixed valence complexes can be understood. The results presented in the following chapters underscore the important role dynamics play at the borderline of delocalization. That is, solvent dynamics are everything to an almost delocalized transferring electron because rates are in a regime of pre-exponential control. If you are able to select for faster or slower promoter modes, you can affect a localized-to-delocalized transition.

1.7 References

(1) Grätzel, M. *Acc. Chem. Res.* **1981**, *14*, 376.

(2) Wasielewski, M. R. *Chem. Rev.* **1992**, *92*, 435.

(3) Sun, L. C.; Hammarstrom, L.; Akermark, B.; Styring, S. *Chem. Soc. Rev.* **2001**, *30*, 36.

(4) Imahori, H.; Mori, Y.; Matano, Y. *J. Photochem. and Photobio. C* **2003**, *4*, 51.

(5) Meyer, T. J. *Acc. Chem. Res.* **1989**, *22*, 163.

(6) Bard, A. J.; Fox, M. A. *Acc. Chem. Res.* **1995**, *28*, 141.

(7) Gust, D.; Moore, T. A.; Moore, A. L. *Acc. Chem. Res.* **2000**, *34*, 40.

(8) Marcus, R. A. *J. Chem. Phys.* **1956**, *24*, 966.

(9) Marcus, R. A. *J. Chem. Phys.* **1956**, *24*, 979.

(10) Marcus, R. A. *Can. J. Chem.* **1959**, *37*, 155.

(11) Marcus, R. A. *Angew. Chem.-Int. Edit.* **1993**, *32*, 1111.

(12) Lu, H.; Petrov, V.; Hupp, J. T. *Chem. Phys. Lett.* **1995**, *235*, 521.

(13) Creutz, C.; Taube, H. *J. Am. Chem. Soc.* **1969**, *91*, 3988.

(14) Reimers, J. R.; Wallace, B. B.; Hush, N. S. *Philos. Trans. Roy. Soc. A* **2008**, *366*, 15.

(15) D'Alessandro, D. M.; Keene, F. R. *Chem. Soc. Rev.* **2006**, *35*, 424. (16) Brunschwig, B. S.; Creutz, C.; Sutin, N. *Chem. Soc. Rev.* **2002**, *31*, 168.

(17) Hush, N. S. *Prog. Inorg.Chem.* **1967**, *8*, 391.

(18) Hush, N. S. *Prog. Inorg. Chem.* **2007**, *8*, 391.

(19) Brunschwig, B. S.; Sutin, N. *Coord. Chem. Rev.* **1999**, *187*, 233.

(20) Nelsen, S. F.; Tran, H. Q.; Nagy, M. A. *J. Am. Chem. Soc.* **1998**, *120*, 298.

(21) Sutin, N. J. *Prog. Inorg. Chem.* **1983**, *30*, 441.

(22) Libby, W. F. *J. Phys. Chem.* **1952**, *56*, 863.

(23) Demadis, K. D.; Hartshorn, C. M.; Meyer, T. J. *Chem. Rev.* **2001**, *101*, 2655.

(24) Weaver, M. J. *Chem. Rev.* **1992**, *92*, 463.

(25) Glover, S. D.; Goeltz, J. C.; Lear, B. J.; Kubiak, C. P. *Coord. Chem. Rev.* **2010**, *254*, 331.

(26) Glover, S. D.; Lear, B. J.; Salsman, C.; Londergan, C. H.; Kubiak, C. P. *Phil.Trans. Roy. Soc. A* **2008**, *366*, 177.

(27) Lear, B. J.; Glover, S. D.; Salsman, J. C.; Londergan, C. H.; Kubiak, C. P. *J. Am. Chem. Soc.* **2007**, *129*, 12772.

(28) Glover, S. D.; Goeltz, J. C.; Lear, B. J.; Kubiak, C. P. *Eu. J. Inorg. Chem.* **2009**, 585.

(29) Barbara, P. F.; Meyer, T. J.; Ratner, M. A. *J. Phys. Chem.* **1996**, *100*, 13148.

(30) Nielson, R. M.; Golovin, M. N.; McManis, G. E.; Weaver, M. J. *J. Am. Chem. Soc.* **1988**, *110*, 1745.

(31) Robin, M. B.; Day, P. *Adv. Inorg. Chem. Radiochem.* **1967**, *10*, 247.

(32) Turro, N. J. *Modern molecular photochemistry*; Benjamin/Cummings Pub. Co.: Menlo Park, Calif., 1978.

(33) Hush, N. S. *Electrochim. Acta* **1968**, *13*, 1005.

(34) Brunschwig, B. S.; Creutz, C.; Sutin, N. *Coord. Chem. Rev.* **1998**, *177*, 61.

(35) Hupp, J. T.; Dong, Y. H. *Inorg. Chem.* **1994**, *33*, 4421.

(36) Bencini, A.; Ciofini, I.; Daul, C. A.; Ferretti, A. *J. Am. Chem. Soc.* **1999**, *121*, 11418.

(37) Yokogawa, D.; Sato, H.; Nakao, Y.; Sakaki, S. *Inorg. Chem.* **2007**, *46*, 1966.

(38) Yamaguchi, T.; Imai, N.; Ito, T.; Kubiak, C. P. *Bull. Chem. Soc. Japan* **2000**, *73*, 1205.

(39) Ito, T.; Hamaguchi, T.; Nagino, H.; Yamaguchi, T.; Washington, J.; Kubiak, C. P. *Science* **1997**, *277*, 660.

(40) Lear, B. J.; Kubiak, C. P. *J. Phys. Chem. B* **2007**, *111*, 6766.

(41) Ito, T.; Hamaguchi, T.; Nagino, H.; Yamaguchi, T.; Kido, H.; Zavarine, I. S.; Richmond, T.; Washington, J.; Kubiak, C. P. *J. Am. Chem. Soc.* **1999**, *121*, 4625.

(42) Hore, P. J. *Nuclear magnetic resonance*; Oxford University Press: Oxford ; New York, 1995.

(43) Grevels, F. W.; Kerpen, K.; Klotzbucher, W. E.; McClung, R. E. D.; Russell, G.; Viotte, M.; Schaffner, K. *J. Am. Chem. Soc.* **1998**, *120*, 10423.

(44) Turner, J. J.; Gordon, C. M.; Howdle, S. M. *J. Phys. Chem.* **1995**, *99*, 17532.

(45) Turner, J. J. In *Handbook of vibrational spectroscopy*; John Wiley and Sons Ltd. : 2002; Vol. 1, p 101.

(46) McClung, R. E. D. In *Program for the simulation of IR spectra of exchanging systems*.

(47) Londergan, C. H.; Salsman, J. C.; Ronco, S.; Dolkas, L. M.; Kubiak, C. P. *J. Am. Chem. Soc.* **2002**, *124*, 6236.

(48) Londergan, C. H.; Salsman, J. C.; Lear, B. J.; Kubiak, C. P. *Chem. Phys.* **2006**, *324*, 57.

(49) Londergan, C. H.; Kubiak, C. P. *Chem. Eur. J.* **2003**, *9*, 5962.

(50) Ondrechen, M. J.; Ko, J.; Zhang, L. T. *J. Am. Chem. Soc.* **1987**, *109*, 1672.

(51) Ferretti, A.; Lami, A.; Ondrechen, M. J.; Villani, G. *J. Phys. Chem.* **1995**, *99*, 10484.

(52) Zhang, L. T.; Ko, J.; Ondrechen, M. J. *J. Phys. Chem.* **1989**, *93*, 3030.

(53) Londergan, C. H.; Kubiak, C. P. *J. Phys. Chem. A.* **2003**, *107*, 9301.

(54) Londergan, C. H.; Rocha, R. C.; Brown, M. G.; Shreve, A. P.; Kubiak, C. P. *J. Am. Chem. Soc.* **2003**, *125*, 13912.

(55) Rocha, R. C.; Brown, M. G.; Londergan, C. H.; Salsman, J. C.; Kubiak, C. P.; Shreve, A. P. *J. Phys. Chem. A.* **2005**, *109*, 9006.

(56) Hupp, J. T.; Williams, R. D. *Acc. Chem. Res.* **2001**, *34*, 808.

Chapter 2

Implications of solvent and temperature on electron transfer rates in Class II/III mixed valence systems

2.1 Introduction

Condensed phase chemical reactions depend on temperature, pressure, and of course, the condensed phase in which they are dissolved, the solvent. The same applies to intermolecular and intramolecular electron transfer reactions, as they too, are sensitive to these conditions. Much effort has been put forth to try to understand exactly how the outer sphere interacts with mixed valence complexes. The specific focus of this chapter is to discover the role of solvent and temperature in mixed valence systems on the cusp of delocalization.

As mentioned in Chapter 1, in order to understand in a broad sense the properties of electron transfer, Robin and Day devised a set of guidelines, based on

solvent, vibrational and electronic motion, by which all mixed valence complexes can be classified.[1] Briefly, a Class I system is uncoupled and no electron exchange takes place. A Class II possesses some degree of electronic communication and the solvent and exchanging electron are localized. Class III systems possess a very high degree of electronic coupling ($H_{AB} \geq \lambda/2$), and the solvent and exchanging electron are taken to be averaged. With the discovery of the Creutz-Taube ion, where a mixed valence complex possessed some properties of Class II and Class III mixed valence species, an additional category, Class II/III was necessary. In a 2001 review of mixed valency Meyer, et al. discussed the localized-to-delocalized transition in mixed valence complexes and proposed a definition for Class II/III systems as follows; the solvent is averaged and the exchanging electron is localized.[2] Based on the results reported here, this definition is restricting in the sense that our observations point to solvent dynamic control rates of electron transfer in Class II/III systems.[3-5] The solvent dynamic aspect is absent from the definition proposed in 2001. Investigating the solvent and temperature behavior of a series of highly electronically coupled complexes led to a deeper understanding of the borderline of delocalization, and prompted a redefinition of Class II/III mixed valency.

2.2 Solvent dependence of ultrafast electron transfer rates

It has previously been demonstrated that for mixed valence dimers of the type $[Ru_3O(OAc)_6(py)(CO)\text{-}(pz)\text{-}(CO)(py)(OAc)_6Ru_3O]^-$ that the degree of coalescence in ν(CO) bandshape provides information about the rate of electron transfer.[6] By varying ancillary ligands or bridging ligand, the electronics in these systems can be "tuned" to give faster or slower rates of intramolecular electron transfer.[7] We know from Marcus Hush theory that outer-sphere contributions can influence intramolecular electron transfer.[8,9] In the mixed valence systems considered here (Figure 2.1) the outer-sphere

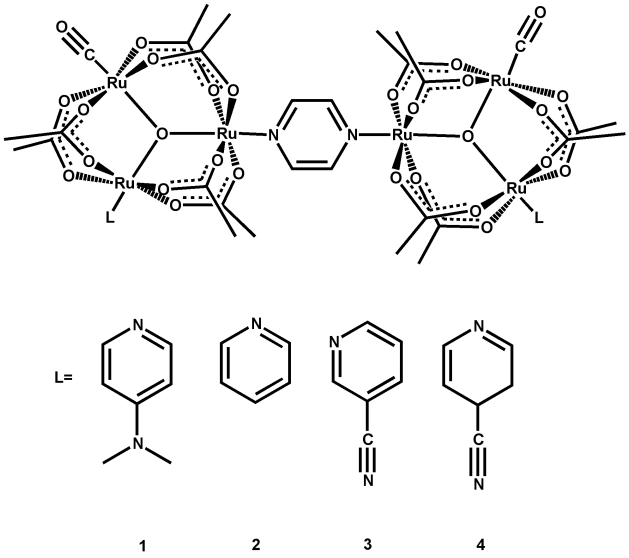

Figure 2.1 Structures of $[Ru_3O(OAc)_6(CO)(L)]_2$-pz, where pz = pyrazine and ancillary ligands **1** = dimethylaminopyridine (dmap), **2** = pyridine (py), **3** = 3-cyanopyridine (3-cpy), and **4** = 4-cyanopyridine (4-cpy).

is composed of solvent molecules, so to monitor outer-sphere effects, all one needs to do is change the solvent in which we study our mixed valence dimer. Figure 2.2 shows varying degrees of ν(CO) coalescence the dimer $[Ru_3O(OAc)_6(py)(CO)$-(pz)-$(CO)(py)(OAc)_6Ru_3O]^-$ in three solvents; tetrahydrofuran, methylene chloride, and acetonitrile.[5] From spectral simulation[10] three different intramolecular electron transfer rate constants in the three different solvents are obtained. From this simple picture, it is clear that the solvent affects electron transfer in these systems. It will be the focus of this chapter to understand how the solvent interactions with the mixed valence dimer affect rates of electron transfer.

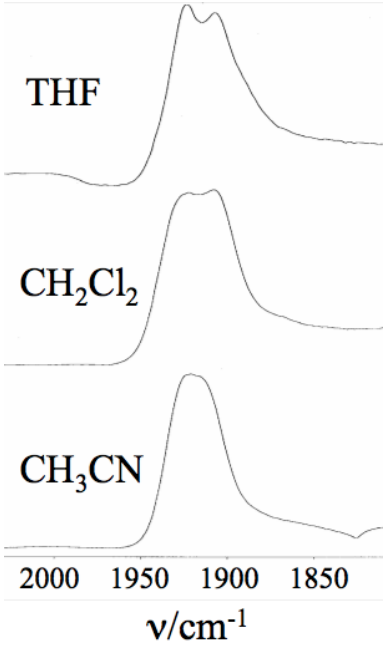

Figure 2.2 Shown are the ν(CO) stretches of the dimer $[Ru_3O(OAc)_6(py)(CO)\text{-}(pz)\text{-}(CO)(py)(OAc)_6Ru_3O]^-$ in tetrahydrofuran (top), methylene chloride (middle), and acetonitrile (bottom) with electron transfer rate constants of 1.05 E 12 s^{-1}, 1.74 E 12 s^{-1}, 2.6 E 12 s^{-1}, respectively.

Table 2.1 Electron transfer lifetimes, k_{et}^{-1}, in picoseconds at -30 °C for mixed valence complexes **1**$^-$ – **4**$^-$.

Solvent	Complex			
	1$^-$	**2**$^-$	**3**$^-$	**4**$^-$
CH_3CN	0.35(5)	0.38(5)	0.72(10)	0.91(12)
CH_2Cl_2	0.50(5)	0.57(5)	0.72(12)	0.91(11)
DMF	0.67(12)	0.77(15)	0.91(10)	1.0(2)
THF	0.83(15)	0.95(15)	1.0(1)	1.0(1)
DMSO	0.77(1)	0.87(14)	1.1(1)	0.9(1)
$CHCl_3$	1.5(2)	1.8(2)	1.9(1)	2.0(1)
HMPA	1.5(2)	2.2(2)	2.5(5)	3.3(3)

Table 2.1 lists the electron transfer lifetimes for four different mixed valence dimers (Figure 2.2) in seven different solvents; acetonitrile (CH_3CN), methylene chloride (CH_2Cl_2), dimethylformamide (DMF), tetrahydrofuran (THF), dimethylsulfoxide (DMSO), chloroform ($CHCl_3$) and hexamethylphosphoramide (HMPA).[4,5] Identifying solvent parameters that correlate well with observed electron transfer lifetimes will bring to light a meaningful relationship between outersphere solvent effects and electron transfer.

2.3 Electron transfer rate dependence on time-independent solvent parameters

There are many solvent parameters by which chemical phenomena can be understood,[11] however, considered here are solvent parameters that are relevant to the theme of electron transfer. Explored here is the relationship of prevalent solvent parameters λ_o, ε_{op}, ε_s, and E_T to picosecond electron transfer lifetimes in **1**$^-$ – **4**$^-$. The degree of correlation is quantified by the average coefficient of determination (R^2) value for linear regression plots of k_{et}^{-1} in **1**$^-$ – **4**$^-$ versus the solvent parameter of interest. Values for λ_o, ε_{op}, ε_s, and E_T are given in Table 2.2.[11,12]

Table 2.2 Selected solvent thermodynamic parameters for the seven solvents used in this study. [a] Values for the static dielectric constants were obtained from reference number 12. [b] Values for optical dielectric constants were taken by squaring the refractive indices taken from reference number 12. [c] The microscopic polarity of the solvents was obtained from reference number 11.

solvent	ε_s [a]	ε_{op} [b]	$(1/\varepsilon_{op} - 1/\varepsilon_s)$	E_T [c]
CH_3CN	35.94	1.81	0.526	45.6
CH_2Cl_2	8.93	2.03	0.381	40.7
DMF	36.71	2.04	0.462	43.2
THF	7.58	1.98	0.373	37.4

Table 2.2 Selected solvent thermodynamic parameters for the seven solvents used in this study. [a] Values for the static dielectric constants were obtained from reference number 12. [b] Values for optical dielectric constants were taken by squaring the refractive indices taken from reference number 12. [c] The microscopic polarity of the solvents was obtained from reference number 11, continued.

DMSO	46.45	2.19	0.435	45.1
$CHCl_3$	4.81	2.09	0.270	39.1
HMPA	29.30	2.13	4.36	40.9

The first parameter to be investigated is the solvent reorganization energy, λ_o, which measures the energetic contributions of the solvent to the barrier for optically induced electron transfer,[13] and is the standard solvent parameter used in the mixed valence community. From Marcus' electron transfer theory, λ_o can be described by the following equation:

$$\lambda_o = \frac{(\Delta e)^2}{8\pi}\left(\frac{1}{\varepsilon_{op}} - \frac{1}{\varepsilon_s}\right)\int (D_A - D_B)^2 \, d\tau$$

Here, Δe is the amount of charge transferred, ε_{op} is the optical dielectric constant, ε_s is the static dielectric constant, and D_A and D_B are the dielectric displacement vectors of the precursor and successor complexes, respectively. For electron transfer in a particular mixed valence complex in different solvents, Δe, D_A and D_B, is expected to be unchanged, and the only variation in the outer-sphere reorganization energy will be accounted for in the term $(1/\varepsilon_{op} - 1/\varepsilon_s)$. The reorganization energy is included in the expression for the barrier to thermal electron transfer,$\Delta G_\lambda^* = (\lambda - 2H_{AB})^2/4\lambda$.[13] I can be expected that the term $(1/\varepsilon_{op} - 1/\varepsilon_s)$ show good correlation with electron transfer rates in mixed valence systems.[8] For the mixed valence systems **1**$^-$ – **4**$^-$, good correlation with λ_o was expected, however, this was far from what was observed. In fact, upon examination of the plot of $(1/\varepsilon_{op} - 1/\varepsilon_s)$ versus electron transfer lifetimes of **1**$^-$ – **4**$^-$, reveals no correlation at all. This is alarming, as this quantification of λ_o has been widely

applied by the mixed valence community to understand the solvent contribution to the reaction coordinate. As the data in Figure 2.3 clearly show, λ_o does not describe the solvent dependence of the mixed valence systems **1**$^-$ – **4**$^-$.

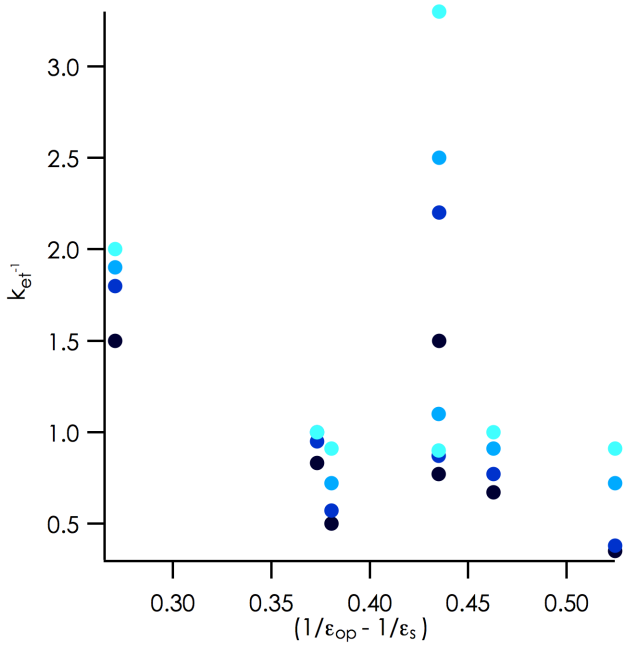

Figure 2.3 A plot of $(1/\varepsilon_{op} - 1/\varepsilon_s)$, the variable portion of the outer sphere reorganization energy, versus the lifetime for electron transfer, k_{et}^{-1}, for complexes **1**$^-$ (●), **2**$^-$(●), **3**$^-$(●), **4**$^-$(●). The average of R^2 values for each dimer in the plot is 0.191, indicating poor correlation between this solvent parameter and k_{et}^{-1}.

Although there is clearly no correlation between λ_o and k_{et}^{-1}, it is possible that contributions from a single dielectric constant could bear more relevance in the solvent dependent electron transfer rates of **1**$^-$ – **4**$^-$. The static dielectric constant, ε_s, is a measure of the solvent response to an applied electric field and gauges the extent to which the solvent is affected by an external field. It should be noted that from the perspective of the solvent in a mixed valence system, the external field is induced by the mixed valence ion. The equation for ε_s is given by equation below.[14]

$$\varepsilon_s = \left(\frac{4\pi}{3}\right) N_o \left(\alpha_o + \frac{\mu^2}{3kT}\right)$$

Here, α_o is the polarizability of the solvent molecules, which accounts for how their electron clouds are perturbed by local electric fields, and μ accounts for the orientation of the permanent dipole moment of the solvent response to the applied field. The static dielectric constant parameterizes how the solvent will respond when there is an external change in dipole moment, such as the change in dipole moment that occurs due to an electron transfer. Figure 2.4 shows a plot of ε_s versus the electron transfer lifetime. This lack of agreement likely stems from the fact that ε_s only describes a solvent's response when the applied field is either static or oscillates at frequencies less than those associated with the timescale of the far IR, which is ~10^{11} s^{-1} for **1**$^-$ – **4**$^-$. At frequencies greater than those in the far IR the orientational term, μ, drops out,

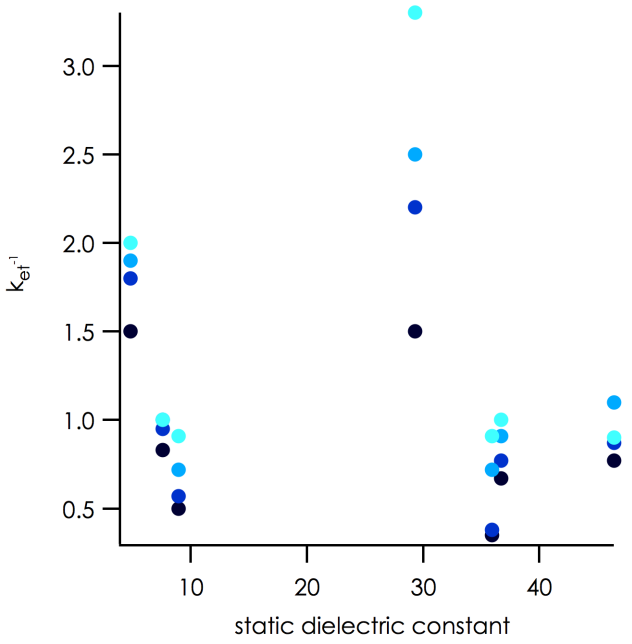

Figure 2.4 A plot of ε_s, the static dielectric constant, versus the lifetime for electron transfer, k_{et}^{-1}, for complexes **1**$^-$(●), **2**$^-$(●), **3**$^-$(●), **4**$^-$(●). The average of R^2 values for each dimer in the plot is 0.040, indicating extremely poor correlation between this solvent parameter and k_{et}^{-1}.

because the solvent can no longer keep pace with the oscillatory changes in electric field. The dielectric that results by exclusion of this term is the optical dielectric constant (ε_{op}) and is equal to the square of the refractive index of the solvent, n^2.[14] We know from IR ν(CO) coalescence that electron transfer rates measured for **1**$^-$ – **4**$^-$ are on the order of 10^{11} s^{-1} or faster, and thus it is not surprising that the correlation between k_{et}^{-1} and ε_s is unsatisfactory. Because rates of electron transfer are fast in **1**$^-$ – **4**$^-$, ε_{op}, which corresponds to faster timescales, may provide a better parameter for comparison with k_{et}^{-1}. However, looking at the plot in Figure 2.5, it can be seen that the correlation is slightly better, but far from satisfactory. Although dielectric parameters have a frequency dependence, their application can only be realized in a static sense

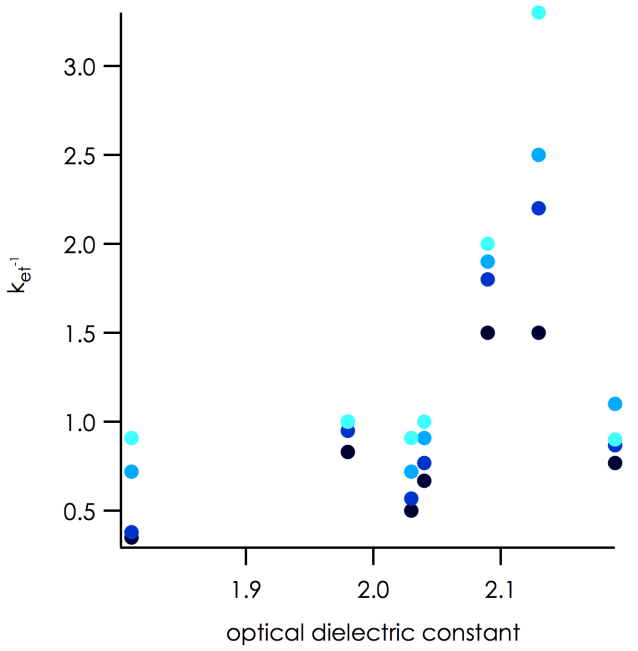

Figure 2.5 A plot of ε_{op}, the optical dielectric constant, versus the lifetime for electron transfer, k_{et}^{-1}, for complexes **1**$^-$(●), **2**$^-$(●), **3**$^-$(●), **4**$^-$(●). The average of R^2 values for each dimer in the plot is 0.280, indicating poor correlation between this solvent parameter and k_{et}^{-1}.

because they really account for the *magnitude* of the solvent response to an applied field. These static qualities make these parameters ideal for a continuum solvent

model, but they cannot account for a dynamic solvent response to fluctuations on the order of picoseconds.

It is disconcerting that such frequently employed solvent parameters used to explain electron transfer phenomena fall very short describing the solvent dependence in a set of very well characterized mixed valence complexes, **1**$^{-}$ – **4**$^{-}$. Chemical intuition leads one to conclude that a major contribution to the electron transfer rate should come from the reorganization of solvent nuclear coordinates following the charge redistribution (change in dipole) associated with an electron transfer.[9,15] Solvent polarity is another solvent parameter that could solidify the relationship between electron transfer and solvent response. Solvent microscopic polarity, E_T, measures the solvatochromic response of a dye molecule. Specifically, the most widely accepted microscopic polarity scale is based on the pyridinium-*N*-

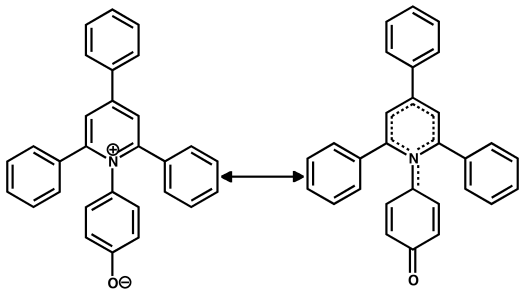

Figure 2.6 The ground state (left) and excited state (right) of the pyridinium-*N*-phenoxide betaine dye used to define the microscopic polarity scale.

phenoxide betaine dye depicted in Figure 2.6. This dye is an appropriate choice as it exhibits a very strongly solvent dependent $\pi \rightarrow \pi^*$ absorption band with intermolecular charge transfer character, as well as a very different dipole moment in ground and excited state.[11] The solvatochromic shift of dye molecules of this type provides a scale for comparison of a solvent's ability to stabilize the charge redistributed excited state of the dye molecule.

It is possible that E_T will also be a good measure of solvent response to electron transfer in **1**$^-$ – **4**$^-$. The plot in Figure 2.7 is a plot of electron transfer lifetime versus E_T, and shows that rates of electron transfer in our complexes, however, do not depend on solvent polarity.

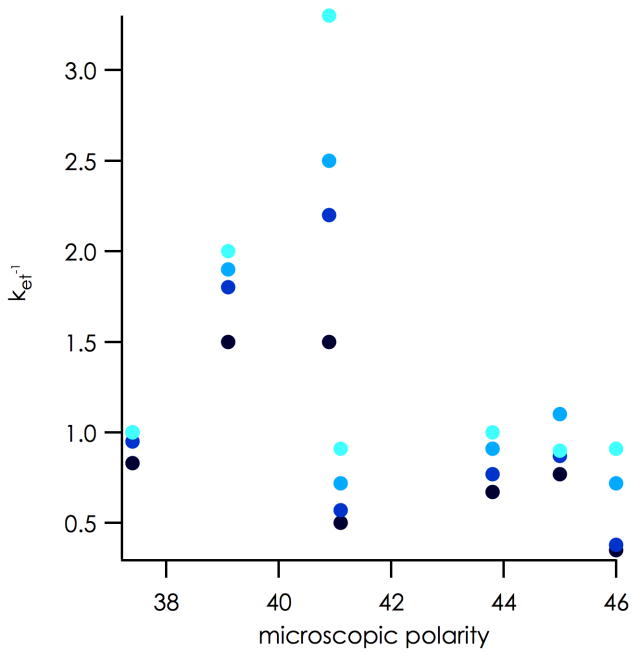

Figure 2.7 A plot of E_T, the microscopic polarity in units of kcal/mol, versus the lifetime for electron transfer, k_{et}^{-1}, for complexes **1**$^-$(●), **2**$^-$(●), **3**$^-$(●), **4**$^-$(●). The average of R^2 values for each dimer in the plot is 0.169, indicating poor correlation between this solvent parameter and k_{et}^{-1}.

The correlation plots in Figures 2.3, 2.4, 2.5, and 2.7 show that there is no definable relationship between electron transfer lifetime and λ_o, ε_{op}, ε_s, or E_T. This would imply that there is little or no connection between the strength of solvent continuum response and changes in the local fluctuating field present in **1**$^-$ – **4**$^-$. More precisely, the energetics of the solvent's response to changes in electric dipole of the mixed valence complex seem to have no bearing on k_{et}^{-1}. Considering equation 8 from

Chapter 1 suggests we are observing a boundary condition for rates of electron transfer.

For mixed valence systems approaching delocalization, $H_{da} \rightarrow \lambda/2$, the term within exponential portion of equation will approach zero and the value of the exponential approaches unity. This implies that $k_{et} \approx \kappa_{el}\nu_N$ and the electron transfer is nearly activationless and the pre-exponential term, ν_N, will dominate the rate expression.[16] From equation 7 in Chapter 1 we learn that the pre-exponential term is composed of the weighted average of all internal vibrational modes that contribute to electron transfer *as well as* solvent modes that allow for solvent reorganization following the electron transfer event.[15,17] With this in mind, it is clear why the normally applied solvent reorganization parameters fail to capture the solvent dependence of **1**$^-$ – **4**$^-$. All of the afore mentioned solvent parameters quantify different thermodynamic time-independent qualities of solvent contribution to the nuclear coordinate. The exponential portion of the equation will dominate the rate expression when the value of the term within the rate expression is not close to zero, which occurs when H_{da} is far from approaching $\lambda/2$. In this regime the thermodynamic terms, λ_o, ε_{op}, ε_s, and E_T will have an impact on the electron transfer rate. However, in highly electronically coupled mixed valence systems (e.g. **1**$^-$ – **4**$^-$) the exponential term approaches unity and the pre-exponential frequencies control the rate of electron transfer. The next section will focus on appropriate dynamic properties of the solvent that can effectively describe the relationship between solvent reorganization and electron transfer rates.

2.4 Electron transfer rate dependence on time-dependent solvent parameters

It is clearly relevant to find acceptable correlation between rates of electron transfer and dynamic (time-dependent) solvent parameters. Table 2.3 below includes the solvent parameters discussed in this section for the seven different solvents used in this study.

Table 2.3 Listed are selected solvent dynamic parameters investigated in this study are solvent viscosity, η, principal moments of inertia, I_x, I_y, I_z, instantaneous solvent response time, τ_0, average lifetime of solvent response, $\langle\tau\rangle$, and time for solvent response function to reach $1/e$, t_{1e}.

solvent	η/ 10^{-3} Pa s	I_x / g Å^2 mol^{-1}	I_y / g Å^2 mol^{-1}	I_z / g Å^2 mol^{-1}	τ_0/ ps	$\langle\tau\rangle$/ ps	t_{1e}/ ps
CH_3CN	0.345	3.31	55.53	55.54	0.12	0.26	0.15
CH_2Cl_2	0.441	16.2	156.9	169.7	0.25	0.56	0.38
DMF	0.924	56.8	122.8	172.9	0.38	2	0.67
THF	0.575	70.5	72.2	125.3	0.43	0.94	0.7
DMSO	1.991	72.3	73.4	120.5	0.4	2	0.9
$CHCl_3$	0.058	152.83	152.96	295.2	0.71	2.8	2.3
HMPA	3.47	474	580	712	0.3	9.9	5.9

The first solvent parameter, viscosity, provides a metric for solvent for solvent fluidity. Viscosity, η, is a function of the rate at which a fluid's velocity changes over a given distance (dv/dx) and is a measure of the restriction of solvent translational motion. In polar solvents with increasingly restricted motion (more viscous) it is expected that ν_N will be smaller and as a result, k_{et} will decrease. This general trend is observed, where mixed valence dimers in a more viscous solvent exhibit slower rates of electron transfer (Figure 2.8).

The correlation between k_{et}^{-1} and η has improved with respect to solvent time-independent parameters, but it is far from satisfactory. This comparison does, however, lend credibility to the intuitive thinking above. The poor correlation between electron transfer and viscosity likely arises from the fact that solvent translational motion is not expected to be as effective at immediate response to a fluxional moment dipole moment of a mixed valence complex undergoing electron transfer. To contrast, solvent rotational motion, which is likely a major component of solvent response. This notion has been investigated by simulation and analysis of solvation

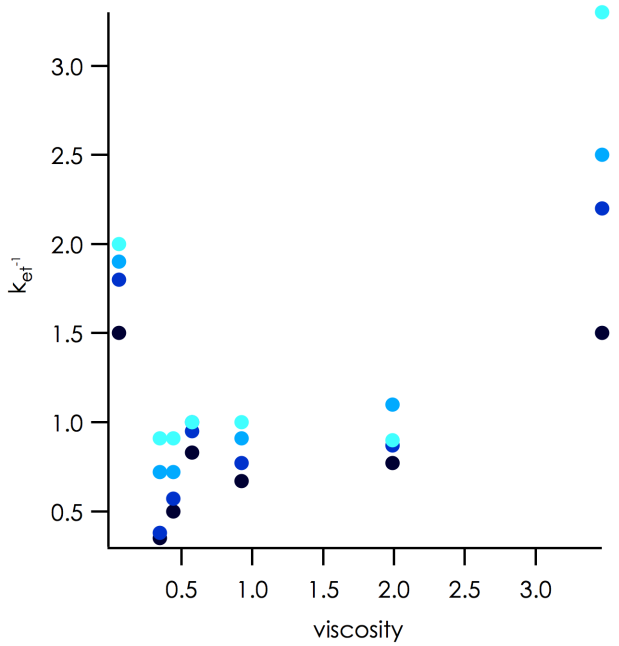

Figure 2.8 A plot of η, the solvent viscosity in units of 10^{-3} Pa s, versus the lifetime for electron transfer, k_{et}^{-1}, for complexes **1**-(●), **2**-(●), **3**-(●), **4**-(●). The average of R^2 values for each dimer in the plot is 0.334, indicating improved correlation between this solvent parameter and k_{et}^{-1}.

spectra Stratt and coworkers.[18,19] They showed that the major contribution to solvation in polar solvents comes from rotational rearrangement of the solvent and also that rotational rearrangement was on the same timescale as solvation. To contrast, they found that translational motion associated with solvation was similar between different

solvents and could not account for differences in the timescale of solvation. Considering the directionality of electron transfer in the dimer systems, it makes sense that rotational motion of the solvent is a key component of solvent dipolar reorganization. The observation that rotational motion of the solvent is likely to be a primary contribution to solvent reorganization orients our thinking toward solvent parameters that can effectively describe the solvent dependence of k_{et}. Weaver has derived an expression for the pre-exponential, ν_N, which depends only on the rotational motion of the solvent; $\nu_N = (2\pi\tau_{rot})^{-1}$.[15] Here τ_{rot} describes the solvent-phase inertial rotation time, and attempts to capture the lifetime of rotation of molecules in a dielectric medium. It is likely that τ_{rot} will correlate well with electron transfer rates, however, the values for solvents used in this study were not readily obtainable. Instead, simpler parameters can be utilized which quantitatively describe the rotational motion of molecules are the principal moments of rotational inertia.

The rotational moment of inertia, $\boldsymbol{I}$, is a measure of how "easily" a molecule can rotate in the x, y, and z direction. The easier a molecule rotates the faster rotation occurs; i.e., the moment of inertia is inversely proportional to the rate of rotation. Since the rate of electron transfer is likely tied to the timescale of solvent dipolar reorientation, there may be a reasonably good correlation between electron transfer lifetimes and $\boldsymbol{I}$ in **1**$^{-}$ – **4**$^{-}$. Table 2 lists $\boldsymbol{I}_x$, $\boldsymbol{I}_y$, and $\boldsymbol{I}_z$ and the corresponding R^2 values from plots of k_{et}^{-1}versus $\boldsymbol{I}_x$, $\boldsymbol{I}_y$, and $\boldsymbol{I}_z$. The correlation is indeed much improved over the previous solvent parameters considered. Figure 2.9 shows a plot of $\boldsymbol{I}_x$ versus k_{et}^{-1}.

Of the three rotational moments, $\boldsymbol{I}_x$ shows the best correlation to k_{et}^{-1} with an averaged R^2 value of 0.825. This is followed by $\boldsymbol{I}_z$, with an R^2 value of 0.748 and lastly, $\boldsymbol{I}_y$ with an R^2 value of 0.657. The result that $\boldsymbol{I}_x$, shows the best correlation to k_{et}^{-1} is not unexpected. Since it is defined as smallest principal moment of inertia, $\boldsymbol{I}_x$ represents the easiest direction of rotation. When a change in external dipole occurs (such as in

an electron transfer reaction in a mixed valence dimer), the most immediate and facile response of the solvent will be to rotate in the direction of least resistance; that is, about the axis with the lowest rotational moment of inertia. In this respect it is very satisfactory that $\boldsymbol{I}_x$ shows the best correlation to k_{et}^{-1}.

It is important to note that in the case of acetonitrile, $\boldsymbol{I}_x$ is not formally associated with a change in dipole because rotation is about the linear (C-C-N) axis. Although it may seem unfitting to include $\boldsymbol{I}_x$ of acetonitrile in our analysis, the following validates its use. The calculated moments of inertia for the solvents studied here only take into consideration a "static" structure that does not vibrate. In reality, bending vibrational modes of the molecule can break linearity, and under a distorted geometry, a rotation about the easy axis *does* reorient the dipole of acetonitrile. Substituting the value of $\boldsymbol{I}_y$ for acetonitrile in place of $\boldsymbol{I}_x$ and plotting as in Figure 2.10 yields an R^2 value of 0.792, which is still in excellent agreement with k_{et}^{-1}. The strong

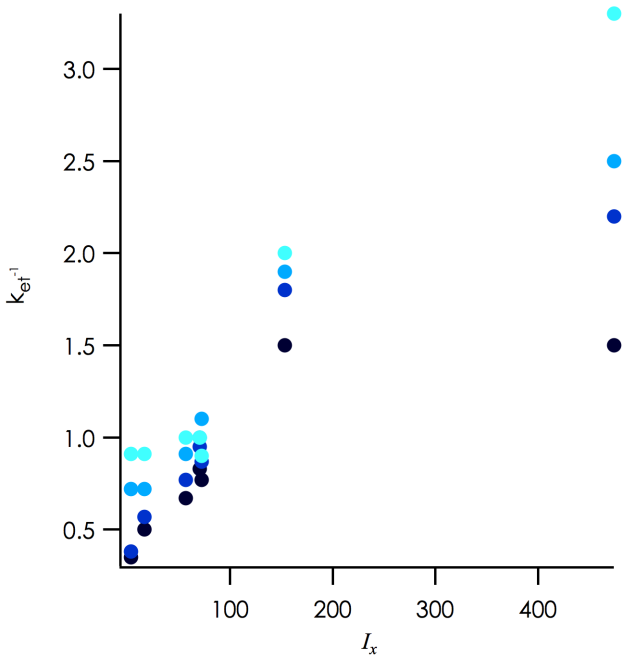

Figure 2.9 A plot of $\boldsymbol{I}_x$, the easy moment of inertia in units of g Å^2 mol^{-1}, versus the lifetime for electron transfer, k_{et}^{-1}, for complexes **1**-(●), **2**-(●), **3**-(●), **4**-(●). The average of R^2 values for each dimer in the plot is 0.825, indicating very satisfying correlation between this solvent parameter and k_{et}^{-1}.

correlation between the solvent moment of inertia and k_{et}^{-1} underscores the importance of solvent rotational motion in the electron transfer process.

It is quite satisfying that solvent rotational motion based on moments of inertia fits very well with observed rates of electron transfer in **1**$^-$ – **4**$^-$ in fluid solution, however, solvent dynamical motion is not limited to rotation. Solvent rotations may be weighted more heavily in the pre-exponential term, but to some extent solvent translational modes will also contribute to dynamic solvation of the mixed valence species. For a mixed valence system to realize coordinate geometries that minimize the potential

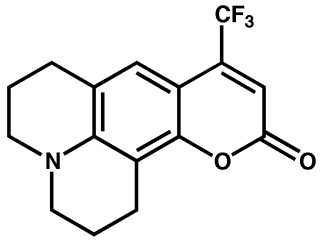

Figure 2.10 Structure of Coumarin 153 dye.

energy following an electron transfer event, solvent rotation and translation are needed to orient the solvent dipoles favorably. A fuller description of solvent dependence on electron transfer reactions in **1**$^-$ – **4**$^-$, will require a parameter that encompasses broader range of solvent reorientational motions is desirable. A comprehensive time resolved study of polar solvation dynamics has been conducted by the Maroncelli group. This yielded solvent parameters which can provide such a description.[20] With ultrafast laser excitation, they observed time dependent emission spectra of Coumarin 153 dye in twenty-four common solvents. "Instantaneous" electronic excitation creates a new charge distribution within the dye molecule, specifically; it delocalizes the lone pair on the nitrogen into the Coumarin ring. Subsequent equilibration of surrounding solvent molecules to accommodate the new

electronic state is accounted for by monitoring the time dependence of spectral response function below.[20]

$$S_v(t) \equiv \frac{v(t) - v(\infty)}{v(0) - v(\infty)}$$

Here, $v(0)$, $v(\infty)$, and $v(t)$ correspond to the initial emission frequency, the steady state frequency, and the emission frequency at some time during dynamic solvent relaxation, respectively. Thus, the spectral response function measures the frequency shift of emission in time as solvation evolves. From this study three characteristic solvation times that describe dynamic solvent behavior were defined: τ_0, t_{1e}, and $\langle\tau\rangle$.[20] The parameter τ_0 corresponds to the instantaneous behavior of solvent before solvent motions evolve, while $\langle\tau\rangle$ emphasizes long-term behavior of the solvent response. $\langle\tau\rangle$ is an average of the lifetimes corresponding to different solvent response components. The values of t_{1e} correspond to the time when $S_v(t)$ reaches $1/e$, and represents a timescale for the total evolution of solvent dynamic response.

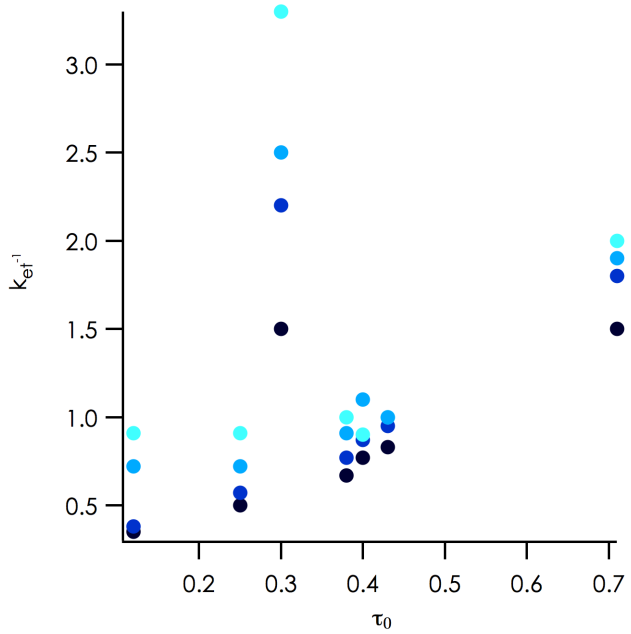

Figure 2.11 A plot of instantaneous solvation response lifetime versus lifetime for electron transfer in complexes **1**-(●), **2**-(●), **3**-(●), **4**-(●). The average of R^2 values for each dimer in the plot is 0.234, indicating less than satisfying correlation between this solvent parameter and k_{et}^{-1}.

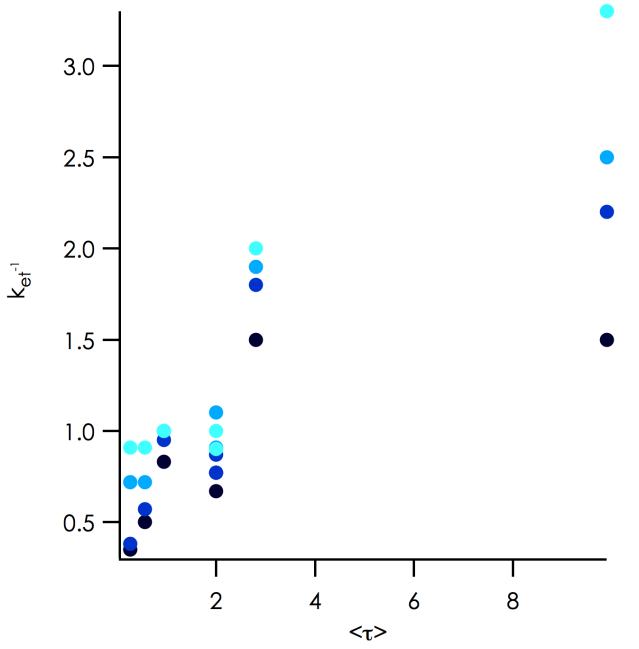

Figure 2.12 A plot of the average of the solvent relaxation times versus the electron transfer lifetimes for **1**-(●), **2**-(●), **3**-(●), **4**-(●). The average of R^2 values for each dimer in the plot is 0.764, indicating surprisingly good correlation between this solvent parameter and k_{et}^{-1}.

The plot in Figure 2.11 shows τ_0 versus the lifetime for electron transfer, where a very poor correlation is observed. The solvation parameter τ_0 deals with the fastest timescales of solvent response. The main component of this lifetime comes from the polarization of the solvent molecules immediately following an electron transfer event, and not from reorientational motion. Polarization of the surrounding solvent is not expected to fully stabilize the newly acquired electronic state of the mixed valence complex, and as such τ_0 is not likely to correlate well with observed electron transfer lifetimes in **1**$^-$ – **4**$^-$.

The plot in Figure 2.12 shows good correlation between $\langle\tau\rangle$ and k_{et}^{-1} in **1**$^-$ – **4**$^-$. This is not entirely expected considering the lifetimes of electron transfer are very fast and the average solvation lifetime includes fast and slow solvation components. However, this good correlation points to the possibility that slower solvent motions, although not dominant, may at least have some role to play in the total dynamic

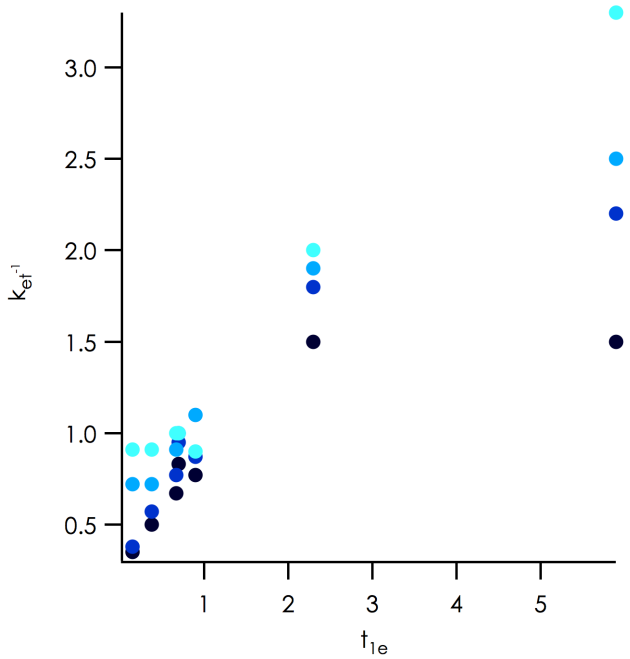

Figure 2.13 A plot of t_{1e} versus lifetime for electron transfer in complexes **1**$^-$(●), **2**$^-$(●), **3**$^-$(●), **4**$^-$(●). The average of R^2 values for each dimer in the plot is 0.860, indicating excellent correlation between this solvent parameter and k_{et}^{-1}.

solvent response.

The final solvent parameter of interest is t_{1e}, which can be thought of as a lifetime for overall solvent dynamic response. This solvent parameter shows the best correlation between electron transfer lifetimes of the mixed valence complexes in this study (Figure 2.13). This should not be a surprise, as t_{1e} is thought to encompass an overall dynamic solvent response. It is believed that a major component of t_{1e} is comprised of an ultrafast (100 – 300 fs) inertial response by the solvent, and that it is this component that is responsible for a large fraction of the solvent relaxation.[20,21] Based on the strong correlation with solvent moments of inertia and t_{1e} with rates of electron transfer in **1**$^-$ – **4**$^-$, it seems that important solvent motions in these systems are largely inertial in character. It is very satisfying to learn that a plot of t_{1e} versus $\boldsymbol{I}_x$ is very close to linear, with an R^2 value of 0.991, Figure 2.14. This points to the very prevalent inertial component in solvent dipolar relaxation, and also to the key role solvent dipolar reorientation dynamics plays in ultrafast electron transfer.

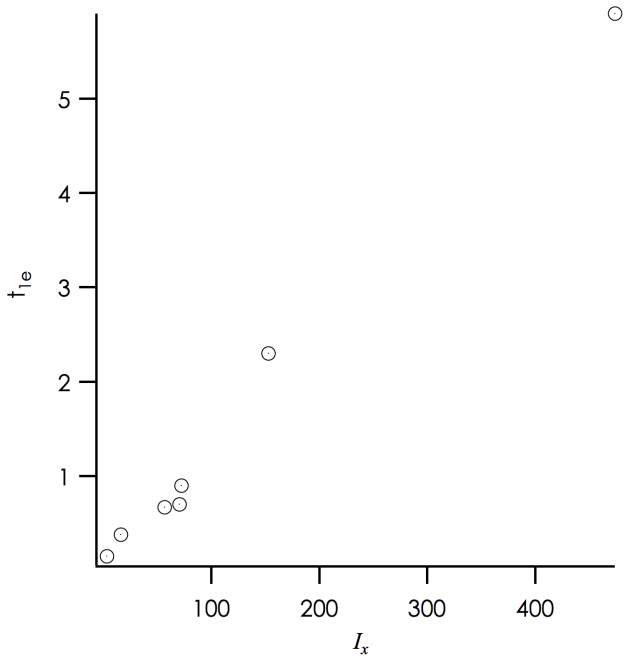

Figure 2.14 Plotted is the "easy" moments of inertia versus t_{1e} for the seven solvents used in this study. There is excellent agreement between these two parameters with an R^2 value of 0.991.

2.5 Solvent thermodynamics versus solvent dynamics in understanding picosecond electron transfer

Sections 2.2 and 2.3 have related the rates of electron transfer in **1**$^-$ – **4**$^-$ to solvent thermodynamic parameters and dynamic parameters, respectively. The difference in correlation between time-independent (thermodynamic) and time-dependent (dynamic) parameters is striking; dynamic parameters display good to excellent correlation with electron transfer rates, whereas thermodynamic parameters display extremely poor correlation. Of the dynamic parameters we consider here, the best correlation in achieved with $\boldsymbol{I}_x$ and t_{1e}, which both correspond to fast dynamic motion of a solvent molecule in the vicinity of a perturbed molecular dipole. The fact that these two parameters correlate extremely well with one another suggests they both involve similar dynamic behavior of the solvent.

By knowing that solvent dynamics provide excellent correlation with k_{et}^{-1} where thermodynamic parameters do not in **1**$^-$ – **4**$^-$, it can be concluded that rates of electron transfer are controlled via the pre-exponential term, ν_N. This pre-exponential solvent control takes effect as a result of the electronic coupling in **1**$^-$ – **4**$^-$ being so large that H_{AB} approaches $\lambda/2$. The pre-exponential frequency factor derived by Weaver in indicates that a major contribution to ν_N comes from fluid solvent dynamics. From a semi-classical description ν_N is composed of a weighted average of internal modes of the molecule and external solvent modes that contribute to the reorganization energy of electron transfer. It is from this vantage point, internal vibrational modes of the molecule in the pre-exponential and their role in electron transfer should be considered.

Solvent dynamic motions are expected to be slower (~10^{12} s^{-1}) than internal vibrational modes (~10^{13} s^{-1}).[16] For example, it is known that the ν_{8a} mode of the pyrazine bridge is strongly coupled to the ground state electron transfer event in **1**$^-$ – **4**$^-$ and will be a mode included in the pre-exponential term.[22] The frequency of this vibration is 4.8 × 10^{13} s^{-1}, while relaxation frequency (from t_{1e}) of the fastest solvent used in this study, acetonitrile, is 6.7 × 10^{12} s^{-1}. Considering the timescales for the processes contributing to electron transfer in **1**$^-$ – **4**$^-$, it would seem that relaxation of the solvent it limiting the rate of electron transfer. Were it possible to decouple solvent dynamics from the intramolecular electron transfer event, the system may be relieved of "solvent friction" effects. In this case the mixed valence system is expected experience an overall *increase* in electron transfer rate.

2.6 Decoupling of solvent modes from ultrafast electron transfer

It has been predicted that decoupling solvent modes from electron transfer reaction can be achieved by freezing the solvent in which electron transfer

occurring.[23] The primary effect of this decoupling is that solvent dipolar reorientation (rotation and translation) will no longer contribute to dynamic reorganization of the system. From the semi-classical definition, this means that ν_N will consist only of a weighted average of intramolecular vibrational modes. When solvent friction is mitigated, ν_N is expected to increase from ~10^{12} s^{-1} to ~10^{13} s^{-1}. There is an exciting, albeit counterintuitive, result that follows from this observation. Rate of electron transfer are expected to *increase* as the solvent temperature decreases. An important point to make, however, is that k_{et} is expected only to increase until the solvent is frozen, and then change no further (i.e. decoupled solvent modes remain decoupled after freezing.) Using **1**$^-$, **2**$^-$ and **4**$^-$ in methylene chloride (m.p. = 181 K) and **2**$^-$ and **4**$^-$ in acetonitrile (m.p. = 229 K), FTIR spectra were collected from 298 K to beyond freezing point for each solvent/complex system. In all cases, as the temperature of the system was decreased from 298 K to just above the freezing point, non-Arrhenius behavior of the electron transfer rate was observed. That is to say, that a slight increase in estimated rate constants occurred at lower temperatures until the system reached the freezing point of the solvent. This result is consistent with a very low activation barrier to electron transfer. As the freezing point of the solvent was approached, a dramatic increase in ν(CO) coalescence occurred for complexes **2**$^-$ and **4**$^-$; two broadened and coalesced, but discernable, bandshapes collapsed into a single highly coalesced bandshape. While **1**$^-$ did display a slight increase in rate of electron transfer, the increase spectral coalescence as the temperature was decreased was less dramatic, as the ν(CO) bandshape was already fully coalesced at 298 K. Tables 2.4 and 2.5 list temperature dependent electron transfer lifetimes up to the freezing point for electron transfer in methylene chloride and acetonitrile, respectively.

Table 2.4 Temperature dependent electron transfer lifetimes for complexes **1**-, **2**-, and, **4**- in methylene chloride are given. Lifetime values are given in picoseconds (ps) with an uncertainty of 0.02 ps.

complex	Temperature / K				
	298	233	213	193	183
1-	0.50	0.50	0.43	0.43	0.29
2-	0.74	0.56	0.56	0.48	0.40
4-	1.52	0.95	0.87	0.71	0.56

Table 2.5 Temperature dependent electron transfer lifetimes for complexes **2**- and **4**- in acetonitrile are given. Lifetime values are given in picoseconds (ps) with an uncertainty of 0.02 ps.

complex	Temperature / K				
	298	253	243	233	223
2-	0.61	0.60	0.56	0.53	0.50
4-	1.20	1.11	0.92	0.56	0.56

The mixed valence complexes **1**- – **4**- all show slower electron transfer lifetimes in "slower" solvents, or solvents with longer t_{1e}'s. How then, does freezing a solvent produce faster k_{et}^{-1}'s? Freezing the solvent causes the dynamic solvent modes (namely rotational and translational modes) to decouple from very fast electron transfer. The dependence on solvent dipole reorientation is lifted from the rate dependence, faster internal vibrational modes dominate and ν(CO) bandshapes should reflect more delocalized electronic structures. Because the timescale of freezing the solvent molecules is much slower than that of electron transfer, the mixed valence ions must exist in "averaged" solvent environments upon freezing. This is how valence trapping is avoided at low temperatures.

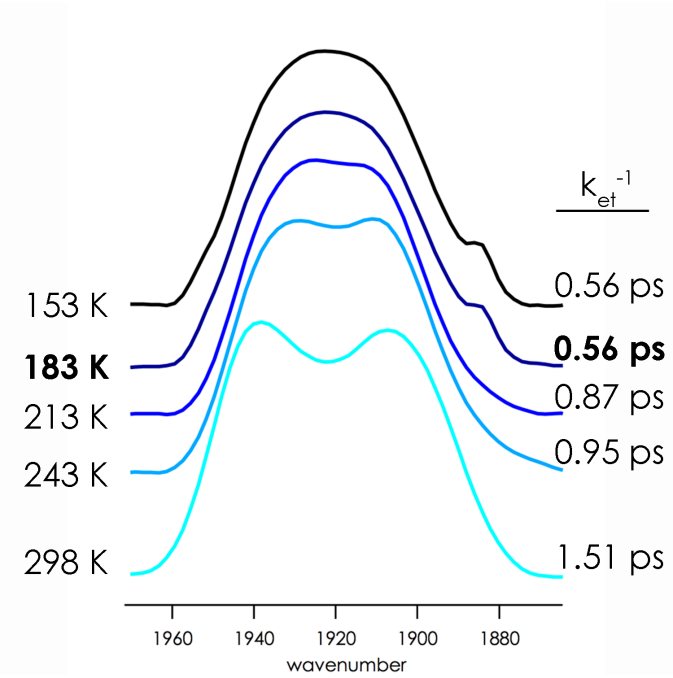

Figure 2.15 IR bandshapes for ν(CO) of the mixed valence dimer **4**$^-$ in methylene chloride as a function of temperature. The bandshape shows increasing coalescence as the freezing point of the solution is achieved (approximately 183 K). To the right of each spectrum are listed the electron transfer lifetimes obtained from simulation of that spectrum.

Complex **4**$^-$, which has the slowest exchange rate of the dimers in this study shows the most dramatic change in ν(CO) coalescence. Examination of Figures 2.15 shows that ν(CO) bandshape increases in coalescence as the solution gets colder and that beyond the freezing point, the same degree of coalescence is observed. The same behavior can be observed for **4**$^-$ in acetonitrile (Figure 2.16). Comparison of Figures 2.15 and 2.16 show that the coalesced bandshapes of complex **4**$^-$ are nearly identical once the solvent has frozen. This implies that the rates of electron transfer in **4**$^-$ in the two environments must be similar at frozen temperatures. This is a most striking detail of these two sets of spectra, highlighted by the fact that the ν(CO) bandshapes are so different when the solvent is fluid. The fact that the rates of electron transfer for **4**$^-$ are the same when both methylene chloride and acetonitrile solutions are frozen is

consistent with the removal of solvent dynamical terms from ν_N, leaving only internal vibrational modes of the molecule. In other words, freezing of methylene chloride and acetonitrile solutions has the effect of equalizing the ν_N term for these solvents. Since the exponential term is nearly unity for these systems, we then see that freezing of the solvents must generate nearly identical electron transfer rates in the different solvents. This analysis is verified by the spectra in Figures 2.15 and 2.16.

One question which arises when studying these data is the following: is there an intrinsic temperature dependence in the ν(CO) bandshape which could lead to broadening not due accelerated electron exchange? It is well known that IR bandshapes change with temperature, especially when the solvent is frozen. Locking the solute in a frozen solvent matrix can lead to increased inhomogeneous

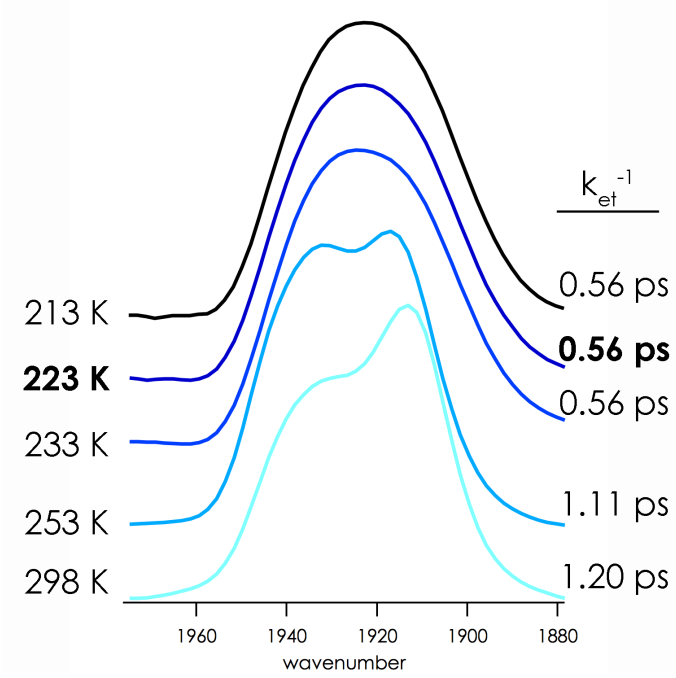

Figure 2.16 IR bandshape for ν(CO) of the mixed valence dimer **4**$^-$ in acetonitrile as a function of temperature. The bandshape exhibits increasing coalescence as the freezing point of the solution is approached (approximately 233 K). To the right of each spectrum are listed the electron transfer lifetimes obtained from simulation of the corresponding spectrum.

broadening.[24] It is imperative, then, to understand the temperature dependence of ν(CO) IR bandshapes independent of electron exchange in order to rule out inhomogeneous broadening effects in lieu of increased coalescence due to faster electron exchange.

To investigate the intrinsic temperature dependence of ν(CO) bandshape a system must be chosen which can be studied in the neutral and fully reduced (-2) state. Dimers **1** – **4** are not stable in the -2 state for the length of time necessary for this study. Ru_3 monomers *are* stable in the neutral and minus one (fully reduced) state and are an appropriate experimental control because the necessary information about temperature dependence of ν(CO) bandshapes in neutral and fully reduced clusters can be obtained. FTIR spectra were collected for the monomer $[Ru_3O(OAc)_6(cpy)_2(CO)]$ in the neutral and minus one state in methylene chloride from 298 K to 83 K and in acetonitrile from 298 K to 173 K.

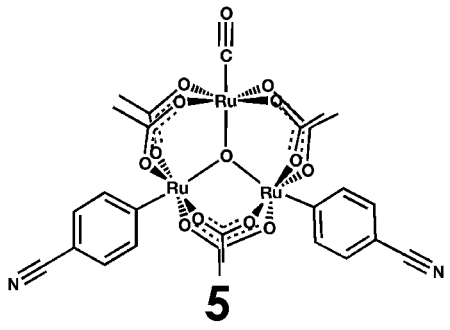

5

Figure 2.17 Complex $[Ru_3O(OAc)_6(cpy)_2(CO)]$ used to investigate the ν(CO) bandshape temperature dependence of a neutral and fully reduced cluster.

The peak position and full width at half-maximum values were measured for the ν(CO) bands of this complex in both solvents. The values are tabulated for both solvent systems and dimer oxidation states in Tables 2.6 and 2.7. As the solvent temperature decreased, slight broadening of ν (CO) bands was observed, accompanied by a shift in peak position. In all cases the shift in peak energy was less

than 6 cm^{-1} from the starting value over the temperature range investigated. Neither the observed shift in energy nor the degree of peak broadening (FWHM) in **5**$^-$ were sufficient to account for the spectral coalescence in **1**$^-$, **2**$^-$ and **4**$^-$ (Figures 2.15 and 2.16). This result verifies that the coalescence we are observing in the mixed valence dimer systems is due to an increase in the rate of dynamic electron exchange, *not* the intrinsic temperature dependence of IR bandshapes.

Table 2.6 Change in position and FWHM of the ν(CO) band fo neutral and minus 1 state of complex **5** in methylene chloride as a function of temperature.

Temperature/ K	Neutral complex		Minus one Complex	
	Peak position/cm^{-1}	FWHM/ cm^{-1}	Peak position/cm^{-1}	FWHM/ cm^{-1}
298	1946.1	20.8	1903.7	20.9
273	1942.2	19.5	1902.6	19.7
253	1943.9	19.7	1901.7	19.2
233	1942.4	18.2	1901.5	19.0
213	1945.8	25.4	1901.7	18.8
193	1949.9	29.1	1901.9	18.7
173	1949.9	29.1	1901.7	21.8
153	1949.9	29.1	1899.6	23.1
133	1949.9	29.2	1899.6	23.5
113	1951.3	29.2	1899.6	23.9
93	1951.9	29.2	1899.6	24.0
83	1959.9	29.0	1899.6	24.0

Table 2.7 Change in position and FWHM of the ν(CO) band fo neutral and minus 1 state of complex **5** in acetonitrile as a function of temperature.

Temperature/ K	Neutral complex		Minus one Complex	
	Peak position/cm^{-1}	FWHM/ cm^{-1}	Peak position/cm^{-1}	FWHM/ cm^{-1}
298	1946.0	14.6	1882.3	16.3
273	1945.8	15.3	1882.2	21.1
253	1942.6	20.3	1880.4	21.7
233	1943.0	20.2	1882.3	17.2
213	1943.7	19.9	1882.3	18.0
193	1944.0	19.9	1882.4	18.2
173	1944.0	19.5	1883.3	18.1

2.7 Conclusions

IR spectral analysis has been used to probe the effects of solvent upon the rates of electron transfer in mixed valence systems which lie on the Class II/III borderline. It has been demonstrated here that exchange rates for intramolecular electron transfer reactions in **1**$^-$ – **4**$^-$ show a strong solvent dependence. The influence of the solvent upon the mixed valence systems lying on the precipice of delocalization does not depend on static thermodynamic parameters, but from parameters of the solvent that figure prominently into system *dynamics*. In particular, we learned from this study that solvent inertial parameters and solvent dipolar reorientation times provide the strongest correlations with the observed electron transfer rates in the solvents studied.

To further understand the important role of solvent dynamics, the behavior of a borderline system when solvent modes are decoupled from the electron transfer event was demonstrated. By freezing the solvent, solvent dynamical terms are removed from the pre-exponential frequency factor. Removal of the solvent dynamical contributions leaves only faster internal modes of the molecule to promote electron transfer. As a result, ν(CO) bandshapes display increased coalescence as the rate of intramolecular electron transfer increases. This behavior is further support that solvent dynamics are controlling the electron transfer rate of the dimers in this study.

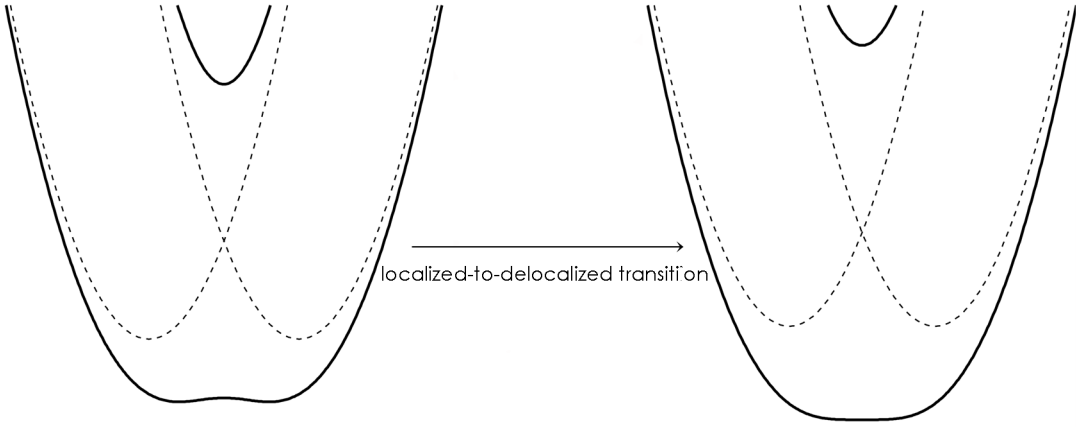

Figure 2.18 Schematic showing the effect of removing "solvent friction" by restricting solvent dipolar reorientation (freezing) from the nuclear coordinate in a Class II/III system, which brings about a localized to delocalized transition.

This study demonstrates a localized to delocalized transition in a series of highly electronically coupled mixed valence complexes, and provides a more complete picture of mixed valency in the Class II/III regime. Based on our observations in this study, a refinement of the definition Class II/III mixed valence complexes is in order. The new definition should be based upon the influence solvent *dynamics* exert on the mixed valence system. Thus, Class II mixed valence complexes are defined as those for which solvent time-independent parameters are able to fully capture the systems

solvent dependence. Class II/III mixed valence complexes are those for which the time-independent solvent parameters fail to account for the solvent dependence of the system, but time-dependent parameters *do* capture the solvent dependence of the system. Furthermore, from the temperature dependent studies, a precise definition of the Class II/III system is that solvent dynamical parameters control rates of electron transfer in borderline systems and tend to localize otherwise delocalized electronic states. Class III systems are those that are solvent independent from a dynamic or thermodynamic perspective as these systems are already electronically delocalized. These definitions provide more descriptive criteria for experimentalist to use when attempting to classify mixed valence systems in the highly coupled Class II, Class II/III and Class III regime. These guidelines are especially helpful with respect to large metal mixed valence complexes where the dynamics of the solvent are more homogeneous than the dynamics of vibrational modes, which can span several orders of magnitude ($\sim 10^{12}\ s^{-1}$ to $\sim 10^{15}\ s^{-1}$).

2.8 Experimental

Complexes used in this study were of the type $[Ru_3O(OAc)_6(CO)(L)]_2$-μ-pz where pz = pyrazine with ancillary ligands **1** = 4-dimethylaminopyridine, **2** = pyridine, **3** = 3-cyanopyridine, and **4** = 4-cyanopyridine, Figure 1. Complexes **1**–**4** were prepared as described previously. Complex **5**, $Ru_3O(OAc)_6(CO)(4\text{-cpy})_2$, was obtained as a side product during the synthesis of complex **4**. The solvents for this study were chosen such that the mixed valence state of the complex is soluble and is stable over a wide range of temperatures. For the optical cryostat studies, acetonitrile and methylene chloride were dried over basic alumina with a custom dry solvent system. Solutions (10 mM) of each dimer were chemically reduced to the mixed valence state with 1.1 molar

equivalents of cobaltocene ($E°'$= −1.33 V vs Fc/Fc^+) in an inert atmosphere. Spectra of mixed valence dimers were recorded on a Bruker Equinox 55 FTIR in a flow through an optical cryostat (Specac, model number 21525). The sample cell, consisting of CaF_2 windows with a path length of 0.1 mm, is contained in a vacuum jacketed housing. Addition of liquid nitrogen to the cooling compartment followed by heating to the desired temperature with a computer-controlled thermocouple/heating coil regulates temperature in the sample cell. Solvents for use in IR spectroelectrochemistry were dried and distilled by the usual methods. The IR spectroelectrochemical responses were measured in a sixth-generation home-built cell mounted onto a specular reflectance unit. The cell has been described in detail elsewhere. Simulation of IR spectra to estimate ET rate constants was performed with VibexGL,[10] a program for the simulation of IR spectra of exchanging systems.

2.9 References

(1) Robin, M. B.; Day, P. *Adv. Inorg. Chem. Radiochem.* **1967**, *10*, 247.

(2) Demadis, K. D.; Hartshorn, C. M.; Meyer, T. J. *Chem. Rev.* **2001**, *101*, 2655.

(3) Glover, S. D.; Lear, B. J.; Salsman, C.; Londergan, C. H.; Kubiak, C. P. *Phil.Trans. Roy. Soc. a* **2008**, *366*, 177.

(4) Lear, B. J.; Glover, S. D.; Salsman, J. C.; Londergan, C. H.; Kubiak, C. P. *J. Am. Chem. Soc.* **2007**, *129*, 12772.

(5) Londergan, C. H.; Salsman, J. C.; Ronco, S.; Dolkas, L. M.; Kubiak, C. P. *J. Am. Chem. Soc.* **2002**, *124*, 6236.

(6) Ito, T.; Hamaguchi, T.; Nagino, H.; Yamaguchi, T.; Washington, J.; Kubiak, C. P. *Science* **1997**, *277*, 660.

(7) Salsman, J. C.; Ronco, S.; Londergan, C. H.; Kubiak, C. P. *Inorg. Chem.* **2006**, *45*, 547.

(8) Hush, N. S. *Prog. Inorg.Chem.* **1967**, *8*, 391.

(9) Marcus, R. A. *J. Chem. Phys.* **1956**, *24*, 966.

(10) McClung, R. E. D. In *Program for the simulation of IR spectra of exchanging systems*.

(11) Reichardt, C. *Solvent Effects in Organic Chemistry*; Verlag Chimie GmbH: Weinheim, **1978**; Vol. 3.

(12) Murov, S. L.; Carmichael, I.; Hug, G. L. *Handbook of photochemistry*; 2nd ed.; Marcel Dekker, Inc.: New York, 1993.

(13) Sutin, N. J. *Prog. Inorg. Chem.* **1983**, *30*, 441.

(14) Shoemaker, D. P.; Garland, C. W. *Experiments in Physical Chemistry*; McGraw-Hill: New York, **1962**.

(15) Weaver, M. J. *Chem. Rev.* **1992**, 92, 463.

(16) Brunschwig, B. S.; Creutz, C.; Sutin, N. *Chem. Soc. Rev.* **2002**, *31*, 168.

(17) Sutin, N. In *Electron Transfer-from Isolated Molecules to Biomolecules, Pt 1* **1999**; Vol. 106, p 7.

(18) Stratt, R. M. *Acc. Chem. Res.* **1995**, *28*, 201.

(19) Stratt, R. M.; Maroncelli, M. *J. Phys. Chem.* **1996**, *100*, 12981.

(20) Horng, M. L.; Gardecki, J. A.; Papazyan, A.; Maroncelli, M. *J. Phys. Chem.* **1995**, *99*, 17311.

(21) Maroncelli, M. *J. Mol. Liq.* **1993**, *57*, 1.

(22) Londergan, C. H.; Rocha, R. C.; Brown, M. G.; Shreve, A. P.; Kubiak, C. P. *J. Am. Chem. Soc.* **2003**, *125*, 13912.

(23) Chen, P.; Meyer, T. J. *Inorg. Chem.* **1996**, *35*, 5520.

(24) Turner, J. J. In *Handbook of vibrational spectroscopy*; John Wiley and Sons Ltd. : **2002**; Vol. 1, p 101.

Note: This chapter has been derived from two publications, of which the dissertation author was the primary and second author, respectively: S.D. Glover, B.J. Lear, J.C. Salsman, C.H. Londergan, C.P. Kubiak "Electron transfer and the Class II/III borderline of mixed valency: dependence of rates on solvent dynamics and observations of a localized to delocalized transition in freezing solvents" *Philosophical Transactions of the Royal Society A*, **2008**, *366*, 177-185, and B.J. Lear, S.D. Glover, J.C. Salsman, C.H. Londergan, C.P. Kubiak " Solvent dynamical control of ultrafast ground state electron transfer: implications for class II/III mixed valency" *Journal of the American Chemical Society*, **2007**, *129*, 12772-12779.

Chapter 3

Persistence of a three-state description of mixed valency at the localized-to-delocalized transition.

3.1 Introduction

The study of mixed valence complexes has been of interest to the chemistry, biology, and physics scientific communities for nearly 50 years.[1-3] The classifications of mixed valence complexes, originally defined by Robin and Day[3], as Class I (uncoupled), Class II (moderately coupled) and Class III (delocalized) have been applied to many systems, and these descriptions have been tested and refined by a variety of experimental methods.[4-11,12] One area that is still under discussion is the physical description and classification of complexes that lie somewhere along the border between Class II and Class III, at the threshold of delocalization.[13-15] Here, we describe the spectroscopic behavior of such borderline Class II/III systems[19] in the case of the dimers of trinuclear ruthenium complexes, $[Ru_3(\mu_3\text{-}O)(OAc)_6(CO)(py)\text{-}(\mu_2\text{-}BL)\text{-}$

$Ru_3(\mu_3\text{-}O)(OAc)_6(CO)(py)]^{-1}$, where BL = 1, 4-pyrazine or 4, 4'-bipyridine and py = 4-dimethylaminopyridine (dmap), pyridine (py), or 4-cyanopyridine (cpy) (**1** – **4**), Figure 3.1a. The range of electronic structures available in the series of mixed valence complexes **1**$^-$ – **4**$^-$ affords an opportunity to examine several discrete points along the localized-to-delocalized transition. Previous work in our laboratories has established that the degree of electronic communication in mixed valence ions **1**$^-$ – **4**$^-$ is controlled by the overlap between the d-orbitals of the Ru_3 clusters and the bridging

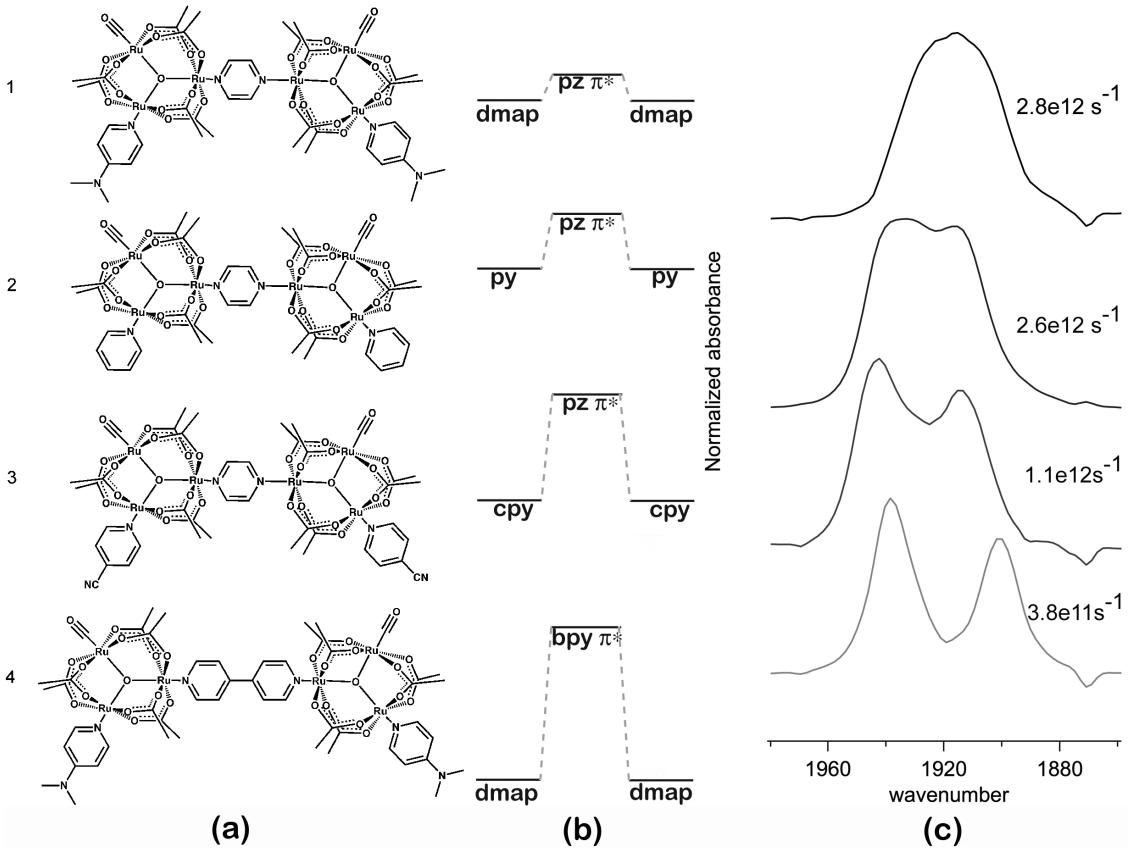

Figure 3.1 (a) The complexes of the type $[Ru_3(\mu_3\text{-}O)(OAc)_6(CO)(py)\text{-}(\mu_2\text{-}BL)\text{-}Ru_3(\mu_3\text{-}O)(OAc)_6(CO)(py)]^{-1}$, where BL = 1, 4-pyrazine and py = 4-dimethylaminopyridine (**1**), pyridine (**2**), or 4-cyanopyridine (**3**), and BP = 4, 4'-bipyridine and py = 4-dimethylaminopyridine (**4**); (b) qualitative molecular orbital representations of relative energies of Ru_3 d-orbitals (LUMO for neutral species) and bridging ligand π^* orbitals; (c) ν(CO) region of the IR spectra of the mixed valence ions **1**$^-$ – **4**$^-$ in acetonitrile at 298 K, and rate constants, k_{ET}, estimated by simulation of the IR lineshape.

pyrazine or bipyrdine π^* orbitals.[20] In pyrazine bridged systems, more electron-donating ancillary pyridine ligands (*i.e.* dmap > py > cpy) raise cluster d-orbital energies relative to the pyrazine π^* orbital. This improved energetic alignment enhances electronic communication between Ru_3O units, Figure 3.1b. A particularly valuable characteristic of the mixed valence ions **1**$^-$ – **4**$^-$ is that the rates of intramolecular electron transfer (ET) can be estimated from the degree of coalescence of the IR spectra of the carbonyl ligands in the ν(CO) region[21,22]. Figure 3.1c shows the ν(CO) spectra of **1**$^-$ – **4**$^-$, and rate constants for ET, k_{ET}, estimated by simulation of the IR lineshape.[22] Rate constants, k_{ET}, increase from *ca.* 4 x $10^{11}s^{-1}$ (**4**$^-$) to *ca.* 3 x $10^{12}s^{-1}$ (**1**$^-$) as the degree of electronic communication increases.

The assignment of mixed valence ions **1**$^-$ – **4**$^-$ as "borderline Class II/III"[6] is based on several lines of experimental evidence. First, the rate constants for intramolecular ET, k_{ET}, estimated by simulation of the 1D IR lineshapes in the ν(CO) region, extend up to *ca.* 3 x $10^{12}s^{-1}$ in solvents such as acetonitrile. This is approaching the average pre-exponential frequency factors in normal Arrhenius type rate expressions, suggesting that the activation barriers for these reactions are approaching zero[13,23], the Class III limit. Second, k_{ET}, estimated by simulation of the 1D IR lineshapes in seven polar solvents showed a strong correlation with solvent dynamics[24], especially Maroncelli's t_{1e},[16] which is considered the fast component of the total solvent dynamic response to changes in the electronic environment. This suggested that the 1D IR lineshapes were being controlled by dynamics on the picosecond time scale, as expected for nearly barrierless ET. Third, freezing the solvents led to complete coalescence of the ν(CO) lineshapes and the rate constants k_{ET} that clearly were different in fluid solution became the same at the solvent freezing points, and did not change upon further cooling. The observed *acceleration* of k_{ET} at the solvent freezing points[19] was explained by a localized-to-delocalized transition where the external solvent

dynamical motions become weighted less than (faster) internal modes of vibration.[25] On the basis of these studies, we have proposed a revised definition of borderline Class II/III mixed valence complexes as those in which the solvent dynamical parameters control rates of ET, and tend to localize otherwise delocalized electronic states.[26]

Here, we describe the intervalence charge transfer (IVCT) spectra of these borderline Class II/III mixed valence complexes. We show that the spectra are best described by a three-state semiclassical model[13] that includes both Ru_3 redox center states, *and* a state for the bridging ligand. Only such a three-state model captures the fact that the mixed valence ions **1**$^-$ – **4**$^-$ display *two* IVCT transitions in the near infrared (NIR) electronic spectra. Further, we show how such three-state mixed valence complexes present temperature and solvent dependences that provide significant information about the degree of electronic delocalization. We are not aware of other systems that offer the opportunity to study optically induced ET in electronic ground states that are delocalized up to the limit that solvent dynamics will allow. The detailed study of three-state mixed valency in these systems offers the opportunity to refine our understanding of the general question of electronic delocalization.

3.2 The Near Infrared (NIR) Electronic Absorption Bands

Figure 3.2 shows the NIR region of the electronic spectra of **1**$^-$- **4**$^-$ in acetonitrile at 298 K. The highest energy band that appears at 16,000 cm^{-1} (**4**$^-$) to 18,000 cm^{-1} (**1**$^-$) is an intra-cluster metal-to-ligand-charge-transfer (MLCT) transition. A similar band is observed in the isolated $[Ru_3(\mu_3\text{-}O)(OAc)_6(CO)(py)_2]$ trimers, and neutral dimers-of-trimers.[20] The observed trend in the increasing energy of this band in the series **3**$^-$ **< 2**$^-$ **< 1**$^-$ tracks the increasing π^* energies of the ancillary pyridine ligands dmap > py > cpy. The MLCT bands at 16,000 cm^{-1} to 18,000 cm^{-1} will not be considered further here. It is the two other bands that appear in the NIR spectra that are of interest. These two

bands appear well separated at 11,000 cm^{-1} and 7,000 cm^{-1} in the spectrum of **1**$^-$, and extensively overlapped in the spectrum of **4**$^-$. Each spectrum was simulated by fitting Gaussian bandshapes in order to extract energies for electronic transitions. In the case of **4**$^-$ the two overlapping bands were fit to two Gaussians, however, due to increasingly pronounced low energy cutoff in more highly coupled species **1**$^-$- **3**$^-$ fitting to a single Gaussian was not possible. The best fitting method was to place a small Gaussian centered at the absorbance maximum of the asymmetric peak. This has the net effect of introducing asymmetry to the bandshape. These curve fits are shown in Figure 3.3. Energies of high energy and low energy bands in acetonitrile at 298 K for **1**$^-$-**4**$^-$ are given in Table 2.

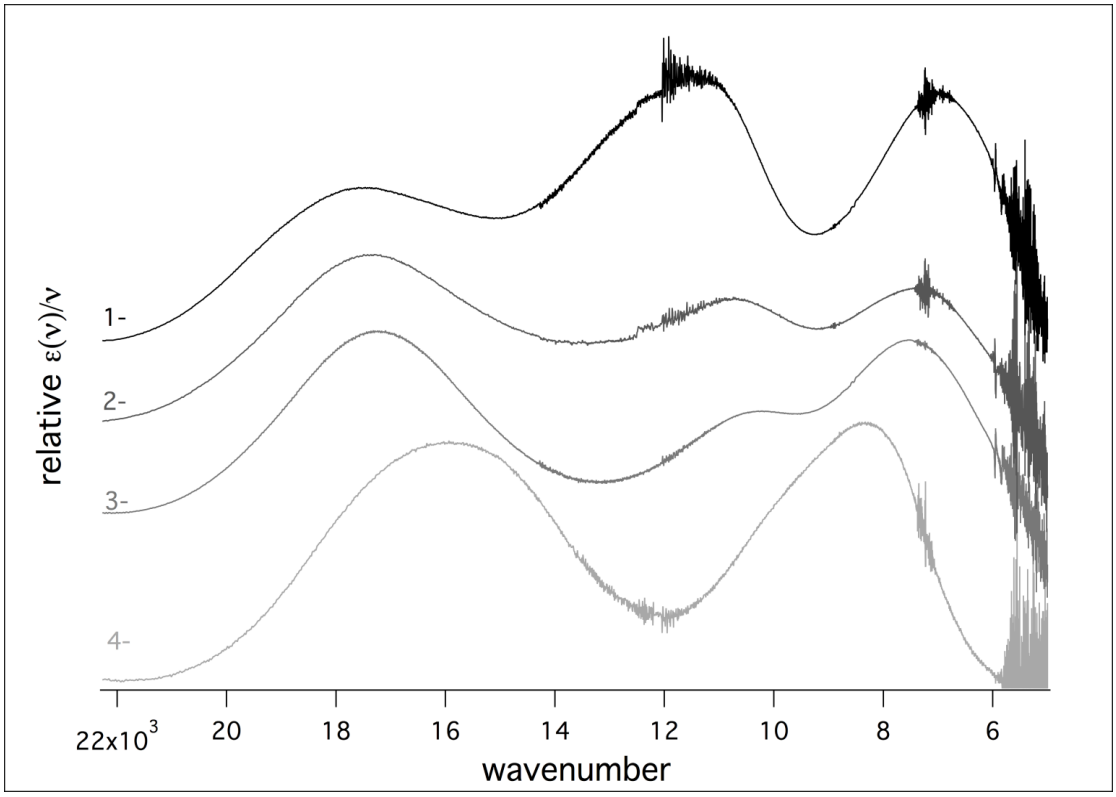

Figure 3.2 Near Infrared (NIR) spectra of **1**$^-$ – **4**$^-$ in acetonitrile at 298K. IVCT band energies are given in Table 1.

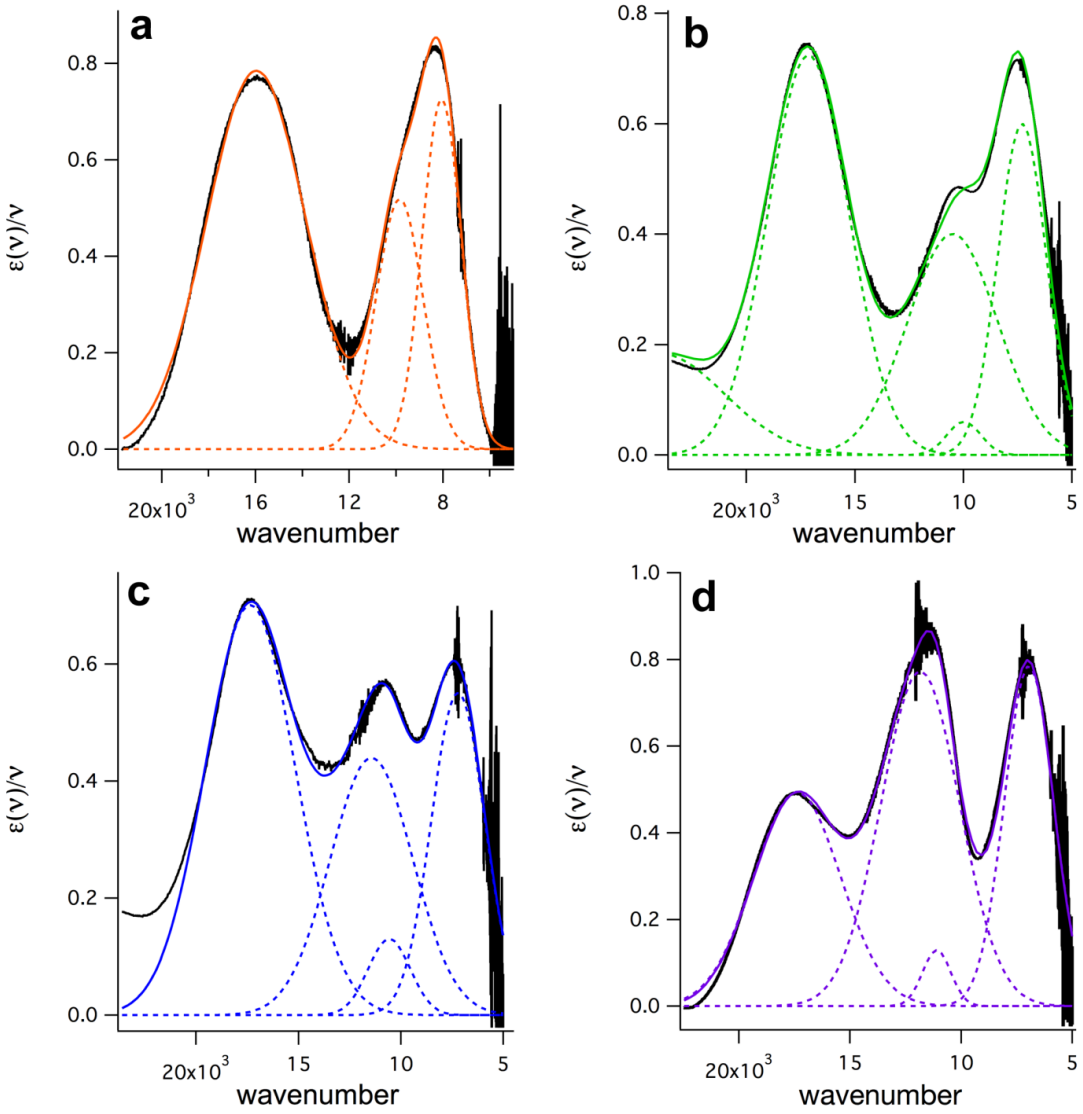

Figure 3.3. Curve fitting was preformed for complexes **1**$^{-}$ – **4**$^{-}$ to determine energies and integrated intensities of MMCT and MBCT bands. Here are the corresponding curve fits for **4**$^{-}$ (a), **3**$^{-}$ (b), **2**$^{-}$ (c), and **1**$^{-}$ (d). MMCT and MBCT bands increase in intensity and asymmetry (on the low energy side of the band) as electronic communication increases through the series **4**$^{-}$ < **3**$^{-}$ < **2**$^{-}$ < **1**$^{-}$. To obtain good curve fits of spectra a smaller "spare" Gaussian is placed beneath the band maximum to simulate asymmetry. The more intense "spare" Gaussian increases in intensity to accommodate greater asymmetry in MBCT bandshapes.

The IVCT spectra of **1**$^{-}$ – **3**$^{-}$ have been assigned with varying degrees of success since their original report in 1997.[21] In the first discussion of the appearance of two IVCT bands, the higher energy band was assigned as the inter-cluster IVCT band, but within the context of a two state Marcus-Hush model, and the lower energy band was assigned as intra-cluster IVCT.[22] In 2006, we proposed three-state (2 Ru_3 sites + bridge), and five-state (2 Ru_3 sites + bridge + 2 ancillary pyridine) models based on the vibronic coupling model originally developed by Ondrechen[9,27,28] to describe the IVCT spectra of **1**$^{-}$ – **3**$^{-}$,[29] and ten related complexes.[20] The three- and five-state vibronic coupling models captured the appearance and trends of the two IVCT bands of complexes **1**$^{-}$ – **4**$^{-}$ and many more, but they did not provide a theoretical framework to describe the localized-to-delocalized transition, or to begin to understand the effects of solvent and temperature. Here, we apply a semiclassical three-state model developed by Brunschwig, Creutz, and Sutin,[13] that is parameterized in terms of donor – acceptor coupling, $H_{AB,}$ donor – bridge – coupling, H_{AC}, and the vertical energy separation between the donor and the bridge state, ΔG_{AC}. We will show how this model behaves through a nearly complete localized-to-delocalized transition, and how it can be combined with solvent models to describe temperature and solvent effects on IVCT spectra at the Class II/III borderline.

3.3 Three state model of mixed valency

Semi-classical Marcus-Hush theory has been used with much success in the description of mixed valence systems.[6,23,30,31] The three-state model, developed by Brunschwig, Creutz, and Sutin closely follows the two-state Marcus-Hush model, but employs a third state to represent the bridging ligand.[13] Though we will focus on the electron transfer aspects of this model, hole transfers are also ubiquitous in mixed valency, for example in donor-bridge-acceptor systems,[32] DNA,[33,34] polymers[35] and

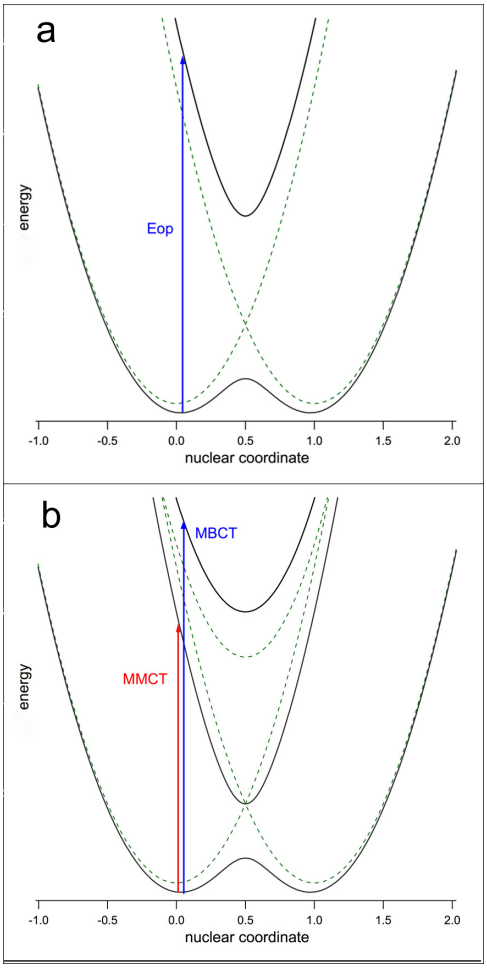

Figure 3.4 a) Diabatic (green dash) and adiabatic (black line) potential energy surfaces of a two state mixed valence system. E_{op} is the optical excitation energy from donor to acceptor surfaces. **b)** Diabatic and adiabatic potential energy surfaces for a three state system, where a surface is included for the bridging ligand state. MMCT corresponds to the energy of the optical transition between donor and acceptor, while MBCT corresponds to the energy of the optical transition from donor to bridge.

quantum dots.[36,37] There are, to our knowledge, a very limited number of studies that follow a multi-state hole transfer analysis and there can be many exciting opportunities in that direction.

Figures 3.4a and 3.4b show potential energy surfaces for a two and three-state model, respectively, along the asymmetric reaction coordinate. Potential energy surfaces (PESs) map the energies along the nuclear coordinate, composed of internal

nuclear coordinates and as well as outer sphere solvent coordinates that contribute to the mixed valence character. When the bridge state lies higher in energy than the donor and acceptor states, the three state model predicts PESs such as those in Figure 3.4b. In the three state system, there are three electronic coupling constants, H_{AB}, H_{AC} and H_{BC}, however in a symmetric system $H_{AC} = H_{BC}$, and only two electronic coupling parameters need to be considered; donor-acceptor coupling is defined as H_{AB}, and donor-bridge coupling as H_{AC}. Electronic coupling between the donor-bridge-acceptor assembly brings about three adiabatic states of consequence: ground and excited state states involving the two metal (Ru_3) units (having mainly metal cluster character), and an excited state in which bridge character predominates. It is

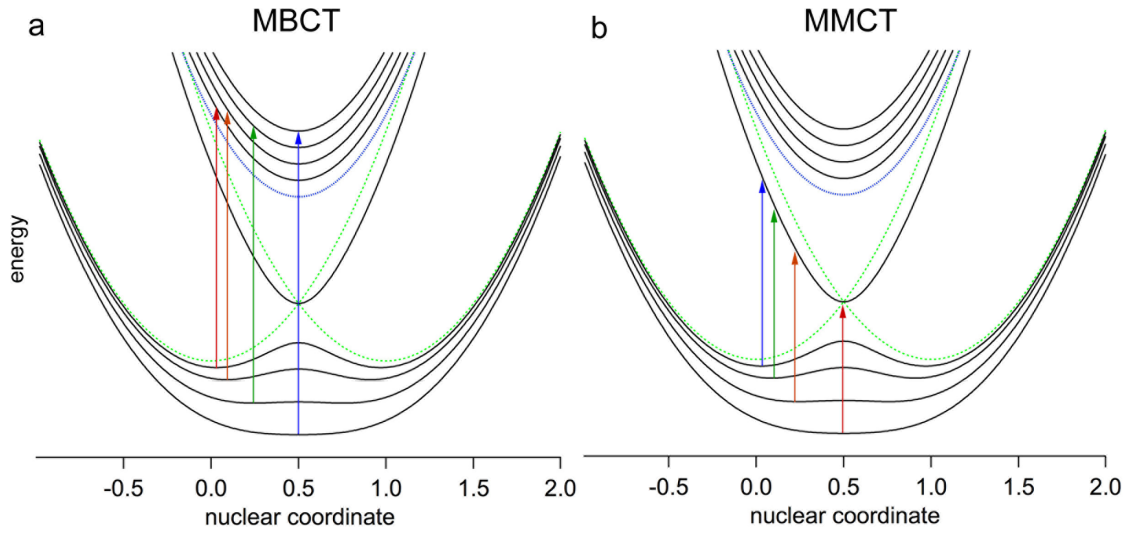

Figure 3.5 a) A series of potential energy surfaces showing the effect of increased coupling on the vertical energy difference, or metal to bridge charge transfer (MBCT) energy of adiabatic ground state and bridge state. Increased coupling leads to more energetic MBCT bands. **b)** A series of potential energy surfaces showing the effect of increased coupling on the vertical energy difference, or metal to metal charge transfer (MMCT) energy of adiabatic ground state and excited metal state. Increased coupling leads to less energetic MMCT bands.

noteworthy that increasing either donor-acceptor coupling, H_{AB}, or donor-bridge coupling, H_{AC} increases the adiabaticity of the three PESs: as the energy of the ground

state PES is stabilized, the activation energy at the classical turning point is decreased, and the minima on each side move closer together. Additionally, as H_{AC} increases the excited state bridge PES is shifted to higher energy. Despite the similarities between the two models, the trends predicted for IVCT bands are quite different. [4,13,23] Most notably, the three-state model predicts two IVCT transitions. When the bridging ligand state is higher in energy than the two metal based states, the low energy transition is metal-to-metal-charge-transfer(MMCT) in character, and the high energy transition is metal-bridging ligand-charge-transfer (MBCT), Figure 3.4b. It is how these two IVCT transitions respond to increasing electronic coupling that contrasts most strongly with conventional two-state behavior.

Figure 3.5 shows a series of three-state PESs with increasing electronic communication. It is expected that as electronic coupling between cluster and bridge states increases, the MBCT band will *increase* in energy, and the MMCT band will *decrease* in energy until delocalization is achieved.[13] In the case of the MBCT band, the trend is the same as an IVCT band of a two state system, but the trend of the MMCT band is the opposite. This trend in energies of MMCT and MBCT bands will continue until the system is fully delocalized (Class III), at which point the MBCT band is predicted to vanish and the MMCT band is predicted to become increasingly narrow and intense.[13] Further predictions for three-state mixed valency include intensification, narrowing and increased band asymmetry on the low energy side of IVCT bandshapes as complexes become increasingly delocalized.[13] The notion that the MBCT band vanishes once delocalization has been achieved was challenged by a recent study of highly electronically coupled Class III systems.[38] In this study, Lear and Chisholm investigated the intervalence properties of a series of delocalized mixed valence complexes and found that not only were MBCT bands present, but they exhibited quite large intensities. Their findings contradict the three-state model where the MBCT

intensity is predicted to vanish at the point of delocalization. The prediction of a vanishing MBCT band is a valid outcome of the three-state model when only electronic coupling between donor and bridge (redox metal state to bridging ligand state) is considered, which implies that MBCT bands have no MMCT character and *vice versa*. However, in real systems, especially those which posses large degrees of electronic coupling, there is likely mixing of donor, bridge and acceptor states and the MBCT band will thus posses at least some MMCT character. In this case, the MBCT band is *not* expected to vanish at the point of delocalization.

To date, it has proven very difficult to classify borderline mixed valence complexes by IVCT bandshape character alone, and further spectroscopic investigation is usually required. The mixed valence complexes **1**$^-$– **3**$^-$ do exhibit borderline behavior in the IR spectra[19,39], but coalescence of IR spectra only indicates that electronic delocalization has been achieved on a picosecond vibrational time scale, which is not necessarily an indication of collapse of the ground state PES to a single minimum. We consider next how the three-state model for mixed valency describes the transition toward delocalization, and the solvent and temperature dependence along the way.

3.4 Interpretation of NIR spectra within the three-state model

The energies of the IVCT bands of complexes **1**$^-$– **4**$^-$ are tabulated in Table 1. Previous studies of these complexes have led to the conclusion that the bridging ligand π^* levels lie higher in energy than the d-orbitals involved in the mixed valence states, as shown in Figure 3.1b.[20,22] Thus, the three-state PESs of Figures 3.4b and 3.5 are appropriate in the description of **1**$^-$– **4**$^-$. Previous studies also indicate the order of increasing electronic communication in the mixed valence ions as: **4**$^-$ < **3**$^-$ < **2**$^-$ **< 1**$^-$. This is based on the larger splittings $\Delta E_{1/2}$ of the reversible reduction processes between the

(0/–1) and (-1/ –2) states that correspond formally to $Ru_3^{III,III,II}$-BL-$Ru_3^{III,III,II}$/$Ru_3^{III,II,II}$-BL-$Ru^{III,III,II}$ (0/-1) and $Ru_3^{III,II,II}$-BL-$Ru_3^{III,III,II}$/ $Ru_3^{III,II,II}$-BL-$Ru_3^{III,II,II}$ (-1/-2), where the -1 state is the inter-cluster mixed valence state of interest. The increasing order of electronic communication is also apparent in the IR spectra in the ν(CO) region, which shows increasing spectral coalescence in the order **4**$^-$ < **3**$^-$ < **2**$^-$ **< 1**$^-$, corresponding to increasing degrees of electronic delocalization on the vibrational time scale. If the two bands between 6,000 cm^{-1} and 12,000 cm^{-1} (Figure 3.2) are considered to be three-state IVCT bands, their behavior with increased degrees of electronic communication can be explained well. From **1**$^-$ to **3**$^-$, there is a gradual decrease in electronic communication, and the high energy IVCT band moves to lower energy as the low energy IVCT band moves to higher energy. That is to say: the high energy IVCT band behaves like a three-state MBCT band, and the low energy IVCT band behaves like a MMCT band. The mixed valence ion **4**$^-$ has a 4, 4' – bipyridine in place of pyrazine as the bridging ligand, and this leads to a sharp decrease in electronic communication, as gauged by electrochemical and IR spectroscopic data.[22] Extensive overlap of the MBCT and MMCT bands is observed for this dimer. The energetic separation between MMCT and MBCT bands is expected to be the smallest with less strongly electronically coupled systems. The assignment of the NIR spectra of **1**$^-$– **4**$^-$ in the 6,000 cm^{-1} to 12,000 cm^{-1} region as MBCT (high energy IVCT band) and MMCT (low energy IVCT band) are also consistent with previous resonance Raman studies.[40,41] Resonance Raman spectra of **1**$^-$– **3**$^-$ showed only enhancement of symmetric modes of the bridging pyrazine ligand upon excitation of the high energy IVCT band.[40,41] It was not experimentally possible to obtain resonance Raman spectra within the low energy IVCT band. The strong apparent vibronic involvement of the bridging pyrazine ligand modes in the high energy IVCT band is consistent with a MBCT electronic transition, and we can be quite confident in this assignment. The lower

energy IVCT bands appearing at *ca.* 7,000 cm^{-1} are then assigned as the MMCT bands.

The three-state description of mixed valency effectively describes the trend in diverging energies of MMCT and MBCT bands in mixed valence complexes **1**$^{-}$– **4**$^{-}$. Recall that at the Class II/III to Class III (localized-to-delocalized) transition the MBCT band is expected to vanish, but we see that even in the most electronically coupled dimer, **1**$^{-}$, strong MBCT intensity persists. Because of the extensive electronic communication in dimers of this study we believe that coupling between all states can exist and MBCT band intensity will remain through a localized-to-delocalized transition. Analysis of the ν(CO) region of the IR spectra of **1**$^{-}$– **3**$^{-}$ led to a similar conclusion.[22] In Figure 3.1c, it can be seen that the ν(CO) spectra of **3**$^{-}$ and **2**$^{-}$ are not coalesced, and that for **1**$^{-}$ is nearly, but not fully coalesced. This has been interpreted in terms of extensive, but incomplete delocalization.[22]

Next, we consider how the MBCT and MMCT bands of the three state model respond to solvent properties and temperature.

Table 3.1 Energies in units of wavenumbers are given for MBCT and MMCT for complexes **1**$^-$ – **4**$^-$ in acetonitrile and methylene chloride. Extinction coefficients and integrated band intensities can be found in Table 3.2.

	Acetonitrile		Methylene chloride	
Complex	MBCT	MMCT	MBCT	MMCT
1$^-$	11100	6950	11130	6645
2$^-$	10560	7050	10350	6820
3$^-$	10090	7300	10050	7310
4$^-$	9530	7920	–	–

Table 3.2 Integrated band intensities, $\int \epsilon(\nu)/\nu$, are given for MBCT and MMCT transtions for mixed valence complexes . Their ratios (MBCT/MMCT) are given in the third column. The relative intesity of the MBCT band increases as electronic communication increases through the series of dimers. Extinction coefficients, $\epsilon(\nu)$, are given for the MBCT and MMCT in the last two columns. All data is for the complexes in acetonitrile at 298 K.

Complex	MBCT	MMCT	MBCT/MMCT	$\epsilon(\nu)$/MBCT	$\epsilon(\nu)$/MMCT
1$^-$	3630	2170	1.67	9300	5600
2$^-$	2560	1800	1.42	5900	4200
3$^-$	2190	1670	1.31	4900	5100
4$^-$	1305	1510	0.865	5000	5100

Table 3.3 Energies (in wavenumbers) of MBCT and MMCT bands of mixed valence complex **3**$^-$ in four different solvents. The difference in energies between acetonitrile and n-butyronitrile is small; 4% for the MBCT and 5% for the MMCT.

Solvent	MBCT	MMCT
Acetonitrile	10090	7300
Methylene chloride	10050	7310
dimethylsulfoxide	10100	7310
n-butyronitrile	10450	6960

3.5 Solvent dependence of three-state MBCT and MMCT bands

Most commonly, a distinction is made between Class II and Class III by a mixed valence complex's solvatochromic behavior of the IVCT bands.[6,15] This stems from the fact that the energy required for solvent reorientation will contribute to the total reorganization energy. Reorganization energy in mixed valence systems is composed of a sum of inner sphere and outer sphere components and is commonly represented by $\lambda_{tot} = \lambda_i + \lambda_o$. The inner sphere component, λ_i, accounts for the energy required for collective nuclear displacements and bond vibrations that are coupled to charge transfer. The outer sphere component, λ_o, accounts for energy required to reorient the solvent following redistribution of charge on the mixed valence species. Descriptions of how the solvent environments interact with the exchanging electron in Class II, Class II/III "borderline", and Class III mixed valence systems follow.[6] For a Class II species, the exchanging electron and solvent are localized. In a Class III mixed valence complex, the electron is delocalized and solvent is averaged. At the Class II/III localized-to-delocalized transition, the electron is localized and solvent is averaged. But, solvent motions that are averaged with respect to a localized electron imply either that solvent motion is faster than electron exchange, or uncoupled to it. For complexes **1**$^-$– **3**$^-$, we have shown that this cannot be the case. Solvent and temperature dependence studies of **1**$^-$– **3**$^-$ have shown that the rates of ET are strongly correlated to solvent dipolar reorientation times.[19,24,39] A particularly relevant question then is: how do three-state mixed valence MBCT and MMCT bands respond to solvent through the Class II/III transition? Table 1 summarizes the MBCT and MMCT band energies of **1**$^-$– **4**$^-$ in acetonitrile and methylene chloride at 25° C.

The data show that there is only a small variance in band energies of the four mixed valence ions in methylene chloride and acetonitrile. In the case of complexes **1**$^{-}$– **3**$^{-}$ it can be seen that band energies of MBCT and MMCT are in general slightly greater in acetonitrile than in methylene chloride. This is consistent with acetonitrile having a larger solvent reorganization energy than methylene chloride, however, the differences are so small that they would not be expected to significantly change the shape of a potential energy surface. Complex **3**$^{-}$ was further studied in dimethyl sulfoxide and n-butyronitrile, and again only a small variance in energies was observed (Table 3.3). The weak solvent dependence of the IVCT bands of **1**$^{-}$ – **3**$^{-}$ are consistent with very low barriers for ET, and extensive delocalization. A note of caution should accompany this analysis. When these complexes are assessed by traditional Marcus-Hush analysis of their bandshapes energies, the degree of delocalization and rates of electron transfer are greatly underestimated.[42] The weak solvent dependence of the IVCT bands of **1**$^{-}$ – **3**$^{-}$ is consistent with complexes that are highly electronically coupled. A source of considerable confusion is that the use of a traditional two-state Marcus Hush treatment leads to a class II assignment, based on the energy of the IVCT bands of **1**$^{-}$ – **3**$^{-}$, but assignment as class III based on their nearly solvent-independent response. It is preferable to establish a more quantitative classification of Class II/III, rather than simply noting that these complexes show some delocalized and some localized behavior. We know from IR vibrational spectroscopy that rates of electron transfer are on the picosecond timescale, which points to nearly barrierless electron transfer and rate constants that are controlled by the pre-exponential frequency factor in the rate expression.[19,39] This underscores the importance of understanding the dynamic contributions to mixed valence character in highly coupled complexes at the borderline of delocalization.

3.6 Temperature dependence of three-state MBCT and MMCT bands

We turn now to the temperature dependence of the MBCT and MMCT bands. A previous study from our laboratory showed non-Arrhenius temperature dependence of rates of electron transfer for **1**$^{-}$–**3**$^{-}$ in acetonitrile and methylene chloride, *i.e.* the rates of ground state intramolecular electron transfer were observed to increase as the temperature of solutions was decreased.[19,39] We described this as a localized-to-delocalized transition as solvent modes were decoupled from the electron transfer reaction. The question of how the MBCT and MMCT bands respond to temperature is now addressed. It will be important in the following analysis to consider parameters used to describe the energetic landscape for the mixed valence system and how they can be affected, if at all, by temperature. Parameters which are fundamental to the energetic description are the electronic coupling parameters, H_{AB} and H_{AC}, ΔG_{AC}, and the reorganization energy, λ. Of these, H_{AB}, H_{AC}, and ΔG_{AC} are not expected to change with temperature, as they are intrinsic electronic parameters of the mixed valence complex.[43] The reorganization energy, specifically the solvent reorganization energy, is expected to change with temperature. The high frequency vibrational modes of the complex which contribute to the inner sphere reorganization energy, λ_i, are not expected to change significantly in the temperature range of this study, which leaves the outer sphere reorganization energy, λ_o, as the sole temperature dependent parameter of interest.

The solvent reorganization energy describes the energy required for solvent dipoles to reorient in order to accommodate change in dipole moment of the mixed valence complex following an electron transfer event. The ubiquitous continuum treatment of solvent from semi-classical Marcus-Hush theory has been used with success for the description of many mixed valence systems.[44] Recent work by Matyushov and others has described some shortcomings of the continuum theory in

describing solvent reorganization energy.[45] A study by Zimmt, Waldeck and coworkers, addresses the differences between Marcus continuum and Matyushov molecular solvation theories and their effectiveness in describing solvent reorganization energy.[43] Their findings are pertinent to the discussion at hand as they describe the different outcomes of temperature dependence of λ_o when considering solvation from a continuum or molecular perspective.

The conventional Marcus-Hush continuum model assumes a dipolar continuum surrounding a "hard sphere" donor-acceptor assembly. The expression for reorganization energy takes into account that optical (ε_{op}) and static (ε_s) dielectric constants, are temperature dependent. The solvent dependent portion, or the Pekar factor[46], describes the solvent dipolar reorientation near the donor-acceptor interface. This model predicts that for strongly polar solvents, like acetonitrile, as temperature decreases the solvent reorganization energy decreases. Matyushov's molecular solvation theory extends the continuum model to include the longitudinal response of the solvent in addition to the reorientational component. Both rotational and longitudinal aspects are temperature dependent, but calculations reveal that their contributions are not equal in magnitude.[43,45] The rotational component has a temperature dependence determined, (as in continuum theory) by the Pekar factor, and the longitudinal component depends on the thermal expansivity of the solvent. The net result is that Matyushov's solvation theory predicts an increase in solvent reorganization energy with decreasing temperature in strongly polar solvents, which is in disagreement with predictions of continuum theory. When longitudinal and rotational components are considered separately, however, the molecular solvation model predicts that the rotational component decreases with temperature. The longitudinal component is expected to increase with decreasing temperature and with greater magnitude than the rotational component. When the two contributions

are considered together, an overall *increase* in solvent reorganization energy as temperature decreases is predicted.

Changes in IVCT bands of **1**$^{-}$–**4**$^{-}$ in acetonitrile and methylene chloride were followed as a function of temperature. Figure 3.6 shows the spectra of **3**$^{-}$ in acetonitrile and methylene chloride at increasingly colder temperatures. What can be seen is that as the temperature of the solution is decreased, the bands intensify and change in energy. Specifically, the MMCT transition decreases in energy and the MBCT transition increases in energy. The divergence in energies of the two transitions is reminiscent of

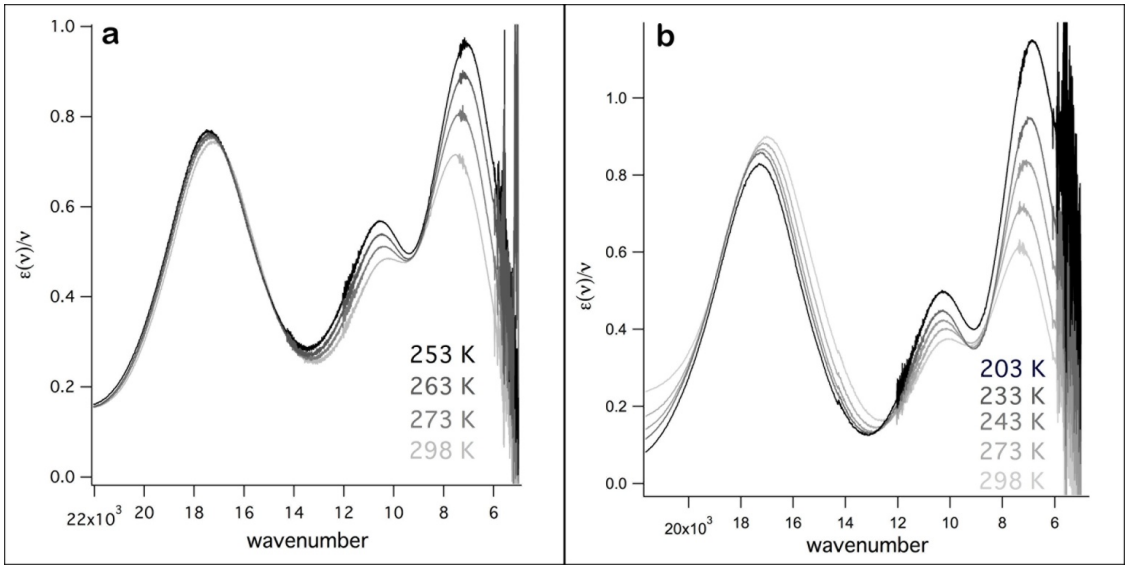

Figure 3.6 Spectra of **3**$^{-}$ collected in acetonitrile (a) and methylene chloride (b). An increase in MBCT and decrease in MMCT band energies is observed in both solvents.

the behavior exhibited by **1**$^{-}$– **4**$^{-}$ as electronic communication increases (*vide supra*). This trend is consistent with increasingly delocalized behavior as the temperature is decreased. Additionally, the MMCT bands increase in intensity by 50% in acetonitrile and 130% in methylene chloride, Figure 3.6. An increase in intensity of the MMCT band is predicted by the three state model for a system which is approaching delocalization. [13] This observation of increasingly delocalized behavior as the

temperature decreases is in accord with our observations of temperature dependence on ground state electron transfer in IR studies of the ν(CO) spectra.[19,39]

Changing the reorganization energy in a mixed valence system, inner or outer sphere, will alter the landscape of potential energy surfaces describing a mixed valence species. Increasing the reorganization energy and treating H_{AB}, H_{AC}, ΔG_{AC} as constants will cause the activation barrier along the symmetric coordinate to increase in a PES, and a mixed valence species will take on more localized character. Conversely, decreasing the reorganization energy will allow a mixed valence species

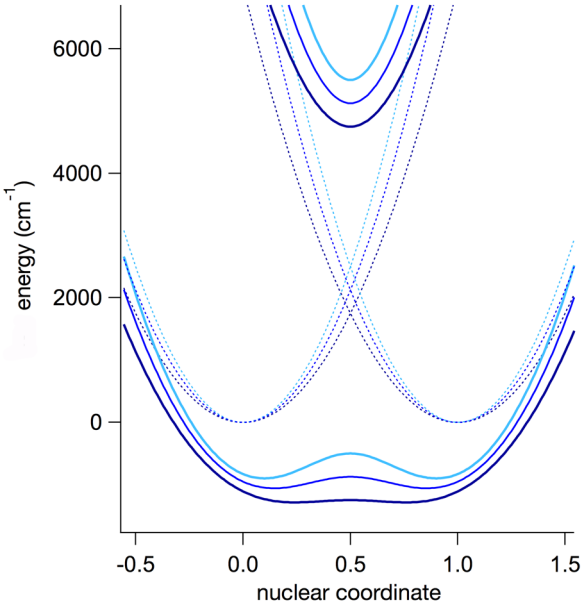

Figure 3.7 Three sets of potential energy surfaces where the electronic coupling constant is held at 3000 cm^{-1} and the reorganization energy is varied. λ is ---, 7000 cm^{-1}, --- 8500 cm^{-1}, and ---10000 cm^{-1}.

to take on more delocalized character. Figure 3.8 shows three sets of potential energy surfaces generated for a two-state system where only the reorganization parameter has been changed. All other factors being equal, when the reorganization energy is smaller, the potential energy surface is more adiabatic. The resultant spectra of **3**$^-$ are consistent with a small decrease in reorganization energy as the temperature is decreased.

From the standpoint of the classic Marcus continuum theory this result is in agreement, however from the more descriptive Matyushov solvation theory, there is clearly a discrepancy. Molecular solvation theory predicts a net increase in solvent reorganization energy as the temperature is decreased. A key point, however, is that molecular solvation theory predicts that the rotational component to the net solvent reorganization energy will *decrease* as temperature decreases. Comparison of ET lifetimes versus solvent dynamic parameters elucidated that the rotational solvent response is a large contribution to the mixed valence character of complexes on the borderline of delocalization. Specifically, we have shown that rates of electron transfer in complexes **1**$^-$ – **3**$^-$ depend strongly on solvent dipolar reorientation, and therefore it stands to reason that the energy associated with these motions will greatly contribute to the outer sphere reorganization energy of these complexes. Likewise, rates of electron transfer in **1**$^-$ – **3**$^-$ do not correlate strongly to slow (longitudinal) solvent response and as such the longitudinal component to the net solvent reorganization energy, so it is expected that this aspect of the outer sphere reorganization energy will not be as important in **1**$^-$– **3**$^-$. Figure 3.9 compares the solvent longitudinal response and the solvent dipolar reorientation time versus electron transfer lifetimes for four symmetric dimers.

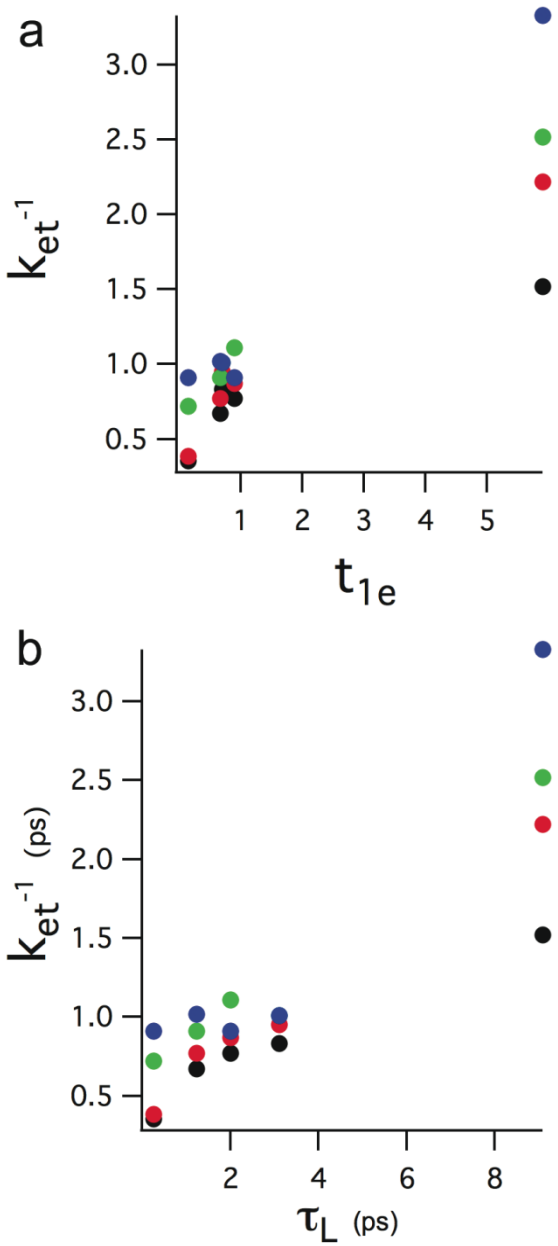

Figure 3.8 a) Solvent dipolar reorientation time versus complex electron transfer lifetime for **1**$^{-}$(●), **2**$^{-}$(●), **3**$^{-}$(●) and [$Ru_3(\mu_3\text{-}O)(OAc)_6(CO)(py)$-($\mu_2$-pyrazine)-$Ru_3(\mu_3\text{-}O)(OAc)_6(CO)(py)]^{-1}$(●) where py=2-cyanopyridine (average R^2= 0.860). The values for solvent (t_{1e}) are as follows: acetonitrile (0.15 ps), dimethylformamide (0.67 ps), tetrahydrofuran (0.7 ps), dimethylsulfoxide (0.9 ps) and hexamethylphosphoramide (5.9 ps).[16] **b)** Plotted are solvent longitudinal response times[17,18], τ_L, versus electron transfer lifetime for the same four dimers (average R^2= 0.605). The values for solvent(τ_L) are as follows: acetonitrile (0.25 ps), dimethylformamide (1.23 ps), tetrahydrofuran (3.1 ps), dimethylsulfoxide (2 ps) and hexamethylphosphoramide (9.09 ps).

The correlation is poorer for the longitudinal solvent response *vs.* electron transfer lifetime than it is for the solvent dipolar response (t_{1e}) *vs.* the electron transfer lifetime. This is evidence that electron transfer in these deeply adiabatic systems is strongly influenced by solvent dipolar reorientation, but less so by solvent translation. This makes sense when considering the timescales of the different solvent motions and rates of ET. Longitudinal motions have a longer timescale than the ET event in **1**$^-$ – **3**$^-$. From a dynamic perspective, ET has already proceeded before solvent longitudinal motion can respond. In contrast, solvent dipolar reorientation times are on the same timescale as ET in these systems, and ET does not proceed until all the nuclear coordinates and solvent dipoles are aligned favorably. By this rationale, it appears that the dipolar reorientation portion of the molecular solvation theory is the component of greater importance when the system is nearly delocalized. With this effect included, current theories of solvation will properly account for more

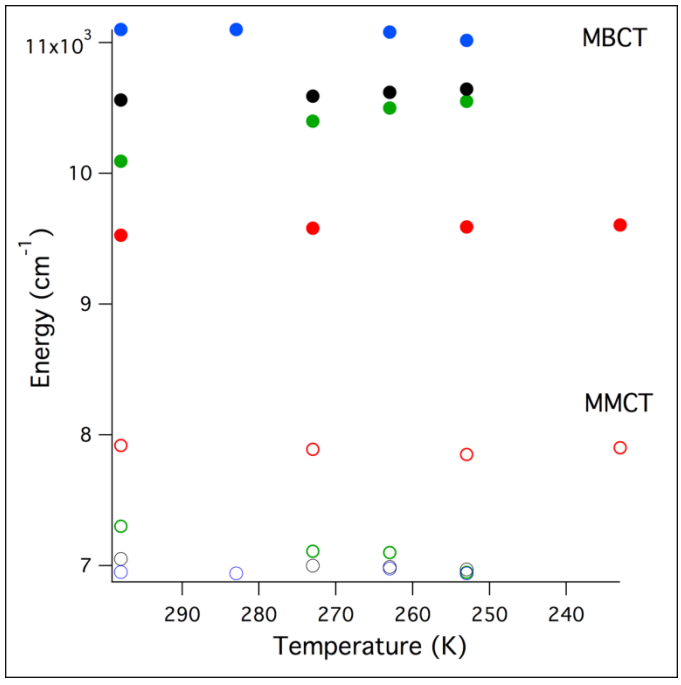

Figure 3.9 Energies of ●MMCT and ○MBCT bands as temperatures are decreased for the four dimers in this study; **1**$^-$ (○), **2**$^-$(○), **3**$^-$ (○) and **4**$^-$ (○).

delocalized behavior on lowering the temperature.

The plot in Figure 3.10 summarizes band energies versus temperature for **1**$^-$ – **4**$^-$ in acetonitrile. Complexes **2**$^-$ and **1**$^-$ show analogous temperature dependent behavior in their MMCT and MBCT band energies, however, **2**$^-$ to a much lesser degree and with almost no change for **1**$^-$. From Figure 3.10 it can be seen that MMCT and MBCT bands of **4**$^-$ are independent of temperature. **4**$^-$ is the least electronically coupled dimer in this study and is a Class II, electron localized, system. By convention, it is expected that the IVCT band of a Class II ion like **4**$^-$ will be solvent dependent, so it may seem unusual that there is no observed temperature dependence. Temperature dependent IR spectra of **4**$^-$ show no change in ν(CO) bandshape and no change in rate constant for electron transfer. This is in contrast to **1**$^-$, **2**$^-$ and **3**$^-$ which all exhibit rate acceleration upon freezing of the solvent. This difference in behavior of **4**$^-$ stems from the fact that the electronic ground state is localized with or without solvent dynamics in play. The more highly coupled systems are localized when solvent dynamics are in play, and delocalized when solvent modes are uncoupled.

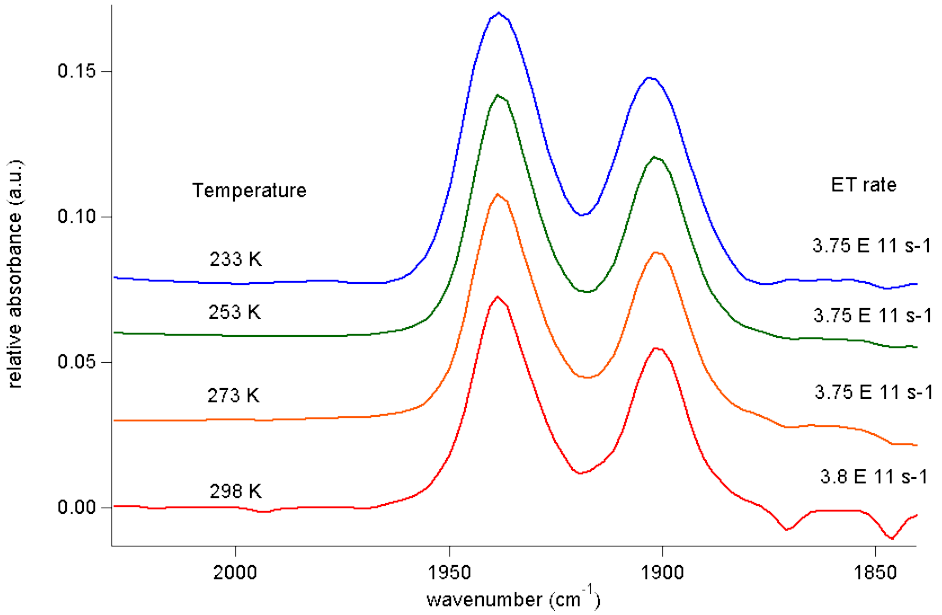

Figure 3.10 The ν(CO) region infrared spectra of mixed valence dimer **4**$^-$ in acetonitrile at 298, 273, 253 and 233K. Changing the temperature of the solution brings about no change in ν(CO) bandshape and no change in rate constant for electron transfer. This is in contrast to **1**$^-$, **2**$^-$ and **3**$^-$ which all exhibit rate acceleration upon freezing of the solvent.

For systems clearly in the Class II regime, solvent dynamic motions can be faster than electron transfer and because of the difference in relative timescales, the two are expected to be uncoupled. This is supported by the temperature independence of ν(CO) stretches for **4**$^-$ in acetonitrile, by the fact that there is no change in bandshape, nor observed rate acceleration, Figure 3.11. Decreasing the solution temperature will change the overall outer sphere reorganization energy to a small degree, however, increased delocalization is not expected because the electron transfer is uncoupled to solvent dynamics. Since localized behavior of **4**$^-$ persists as the solvent is frozen, temperature dependence of the IVCT spectra is not expected.

From Figure 3.10 it can be seen that the trend to more delocalized behavior tapers as electronic communication increases from **3**$^-$ to **1**$^-$. This is consistent with the

series of dimers approaching the late limit of the Class II/III borderline, with **1**$^-$ being the closest to delocalized. Figure 3.12 shows the temperature dependent spectra of **1**$^-$ in acetonitrile. As the solution is cooled the MMCT band begins to intensify and the MBCT loses intensity. This type of behavior is a predicted outcome of a system crossing through a localized-to-delocalized transition. We note, however, that the MBCT band is still present and bears much of its original intensity. This is *not* the predicted behavior when donor, bridge and acceptor are treated as pure states. Due to the nature of strong electronic coupling in these systems, mixing between all states that contribute to the mixed valence character is likely and MBCT intensity should persist through the localized to delocalized transition.

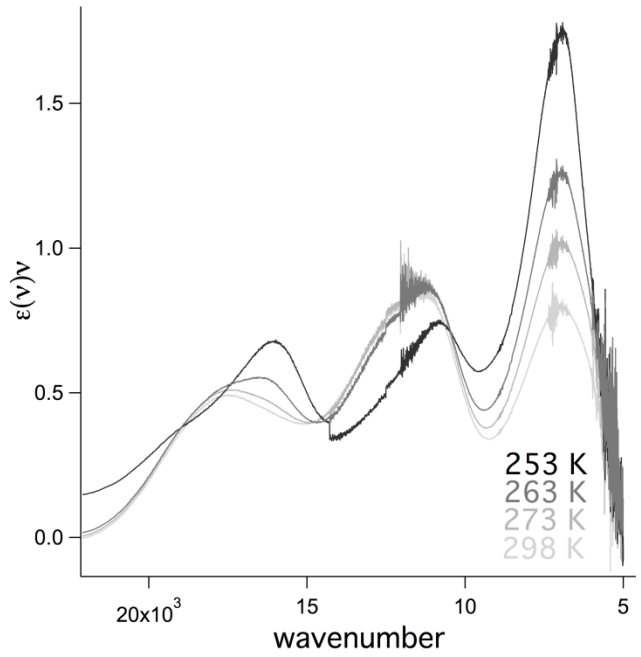

Figure 3.11 **1**$^-$ in acetonitrile at increasingly colder temperatures shows intensification of MMCT band and weakening of the MBCT band, consistent with a Class II/III to Class III transition. This dimer undergoes dramatic changes in intensity; 90% increase in MMCT and 20% decrease in MBCT intensity.

3.7 Three-state Potential Energy Surfaces

A three state model including a state for the bridge has been successfully employed to describe a number of bridged mixed valence complexes in the literature previously.[13,47,48] Potential energy surface analysis gives a snapshot of the energetic landscape of a mixed valence system as well as the ability to simulate IVCT bandshapes. The equations which generate a three state diabatic PES along symmetric and asymmetric coordinates are given below.

$$G_a = \lambda x^2 + \lambda y^2$$

$$G_c = \lambda(x - 0.5)^2 + \lambda(y - 0.5)^2 + \Delta G_{ac}$$

$$G_b = \lambda(x - 1)^2 + \lambda(y - 1)^2$$

Here, G_a, G_c and G_b are the energies of the donor, bridge and acceptor states, respectively. λ is the reorganization energy, x is the symmetric nuclear coordinate and y is the asymmetric nuclear coordinate and ΔG_{ac} is the difference in energy between the minimum of the donor (or acceptor) state and the minimum of the bridge state. In the case that electron donor, bridge, and acceptor are electronically coupled, solving the 3 × 3 secular determinant for the eigenvalues, E will give the energies for the adiabatic PES.

$$\begin{vmatrix} G_a - E & H_{ac} & H_{ab} \\ H_{ac} & G_c - E & H_{bc} \\ H_{ab} & H_{bc} & G_b - E \end{vmatrix} = 0$$

In order to apply a three state treatment to our systems, values for electronic coupling constants, reorganization energy, and ΔG_{ac} will have to be determined. Electronic coupling constants have been estimated for a number mixed valence complexes similar to **1**$^-$ – **3**$^-$.[42] If we make the assumption that a majority of the electronic communication is between donor and bridge, and that the electronic communication between donor and acceptor is negligible, the afore determined values for H_{ab} will provide a reasonable estimate for the complexes in the present study.

DFT calculations were used to estimate ΔG_{ac} for **1**$^{-}$ and **3**$^{-}$. Estimated LUMO energies of the electron donor and bridge state were obtained from program output files. The electron donor is taken to be one half of the dimer unit, $Ru_3(\mu_3\text{-}O)(OAc)_6(CO)(py)(pz)$, and the bridge state is taken to be a free pyrazine ligand. Table summarizes the HOMO and LUMO energies for monomeric clusters and pyrazine. ΔG_{ac} is taken as the energy difference between LUMO of a cluster and the LUMO of pyrazine. For the $Ru_3(\mu_3\text{-}O)(OAc)_6(CO)(py)(pz)$ unit input geometries were obtained from crystallographic data of a closely related compound, $Ru_3(\mu_3\text{-}O)(OAc)_6(CO)(ABCO)$, where ABCO = 1-azabicyclo[2,2,2]octane. To best simulate the donor unit of the complexes in this study, the ABCO ligands on the cluster were replaced with pyrazine and the appropriate pyridyl ligand. From LUMO energies of monomeric cluster versus the LUMO of pz, ΔG_{ac} is estimated to be 14 200 cm^{-1} and 17 600 cm^{-1} for **1**$^{-}$ and **3**$^{-}$, respectively.

Table 3.4 DFT obtained relative HOMO and LUMO energies in wavenumbers. The value of ΔG_{ac} was determined by the difference between LUMO of the cluster versus the pyrazine (pz) ligand.

Complex	HOMO (cm^{-1})	LUMO (cm^{-1})
$Ru_3(\mu_3\text{-}O)(OAc)_6(CO)(dmap)(pz)$	-38872	-25662
$Ru_3(\mu_3\text{-}O)(OAc)_6(CO)(py)(pz)$	-40390	-27095
$Ru_3(\mu_3\text{-}O)(OAc)_6(CO)(cpy)(pz)$	-42159	-29134
pz	-55073	-11464

PES of the ground state along the symmetric and antisymmetric coordinate are shown for **1**$^{-}$ and **3**$^{-}$ in Figure 3.13. The ground state surface for **1**$^{-}$ is much smoother and much closer to parabolic in shape than in **3**$^{-}$, which is expected given that **1**$^{-}$ has a greater degree of electronic coupling.

As can be seen, there is not a distinct minimum present for the bridging state, and the coordinate is smooth. A remarkable result of the three state model is that even with negligible coupling between donor and acceptor, sufficient electronic coupling between donor and bridge will enable nearly barrierless ground state electron transfer. This is shown by the potential energy surfaces in Figure 3.13, where the activation barrier along the symmetric coordinate can be circumvented by travelling along the asymmetric coordinate.[48] This result is in accord with the ultrafast rates of electron transfer measured for these systems. Further work in this area will involve spectral simulation of NIR spectra from PES analysis.

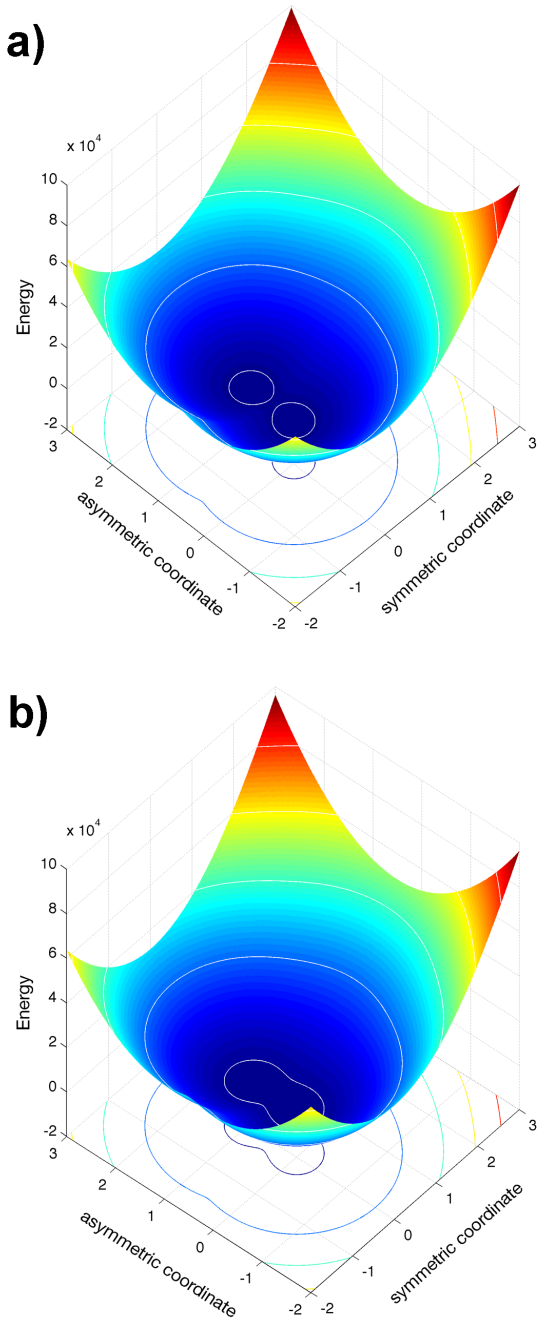

Figure 3.12. PES plots for **3 (a)** and **1 (b)**. The following parameters were used to generate the ground state surface for **3**-: λ= 8000 cm-1, ΔG_{ac} = 16700 cm-1, H_{ab}=0 cm-1 , H_{ac} = 4500 cm-1. The following parameters were used to generate the ground state surface for **1**-: λ= 8000 cm-1, ΔG_{ac} = 14200 cm-1, H_{ab}= 0, H_{ac}=5400 cm-1. A discussion of obtaining ΔG_{ac} can be found in the Supporting Information. Estimations for electronic coupling parameters can be found in reference 33.

3.8 Conclusions

The question of whether a particular system is localized or delocalized is usually best referred to a time scale, up to Class III which represents the absolute limit of electronic delocalization. The classification of mixed valence complexes as "borderline Class II/III" arose from the difficulty in locating precisely how far a particular weakly localized, adiabatic mixed valence system had to go to achieve complete Class III character.[6] More recent studies of the role of solvent dynamics on delocalization have helped clarify the onset of a localized to delocalized transition.[19,26] Thus, a borderline Class II/III system is one in which solvent dynamics such as solvent dipolar reorientation times tend to localize otherwise delocalized electronic states. This will generally occur when electronic coupling is large, barriers to ET are negligibly small, and the rate expression becomes dominated by internal and solvent modes that are heavily weighted in the pre-exponential frequency factor.[19] For systems that are described well by a three-state semi-classical model such as the mixed valence complexes **1**$^-$ – **4**$^-$ in the present study, it is clear that delocalization on the time scale of the fastest (inertial) solvent motions is not sufficient to achieve complete electronic delocalization. The appearance of both the MMCT and MBCT bands in the near IR electronic spectra is a clear indication of a transition dipole that can only be present when there is residual localization in the ground state, although whether the three-state MBCT band disappears completely at the Class III limit was recently questioned.[38] In every other respect, complexes **1**$^-$ – **4**$^-$ exhibit such a well behaved and predictable (by the three-state model) progression through the Class II/III borderline that it is tempting to use criteria from the three-state model to assign a particular system's behavior to either an "early" or "late" Class II/III borderline situation. One trend that becomes immediately clear is that within the three-state description energies of MMCT and MBCT bands diverge with increased electronic communication. This relationship

can be used to compare series of mixed valence complexes with varying degrees of electronic coupling, especially if the value of the electronic coupling constant is not explicitly known, as is often the case in highly electronically coupled complexes. We have also found that a study of solvent and temperature effects can reveal the depth of highly coupled complexes within the Class II/III region. From this study, complex **4**$^-$ displays temperature independence in intervalence band energies in optical electron transfer as well as temperature independence in IR ν(CO) bandshape which points to the lack of solvent dynamic contribution to the nuclear coordinate. The lack of dependence on solvent dynamics of a Class II mixed valence system sets it apart from a borderline Class II/III mixed valence system. As a mixed valence system enters the "early" borderline Class II/III regime, the influence of dynamic contributions from the solvent becomes evident. Vibrational *and* optical investigations of **3**$^-$ and **2**$^-$ reveal solvent dependence of the mixed valence character. In both intervalence and vibrationally induced electron transfer we found that restricting solvent motion (by lowering the temperature) favors delocalized behavior. As mixed valence systems transition through the later end of borderline Class II/III to Class III, solvent and temperature dependence of electron transfer begin to wane, as in **1**$^-$. This is a result of solvent dynamics becoming nearly decoupled from electron transfer as the rate of ET becomes faster than solvent response. This study of mixed valence ions **1**$^-$ – **4**$^-$ has provided a clearer understanding of the borderline of delocalization. It has provided guidelines for establishing where a particular system lies within the border, and criteria that apply to "late" Class II, Class II/III borderline, "late" borderline, and Class III that we believe can be applied more widely.

3.9 Experimental

Synthesis of all compounds has been reported previously in the literature.[21] Acetonitrile and methylene chloride solvents used in this study were obtained from a custom dry solvent system. All other solvents were distilled over sodium benzophenone and degassed before use. Cobaltocene and decamethylcobaltocene were used as received from Strem and Sigma Aldrich, respectively. Chemical reductions were performed under an inert atmosphere. For complexes **1**$^-$ and **4**$^-$ decamethylcobaltocene was added stoichiometrically. For complexes **2**$^-$ and **3**$^-$, cobaltocene was added stoichiometrically to produce the monoanion.

All UVVIS-NIR spectra were collected with a Shimadzu UV 3600. Samples were contained in Specac sealed liquid IR cells with CaF_2 windows and path length of 1.00 mm. Temperature dependent studies were carried out in a Specac cryostat cell. Spectral deconvolution of NIR spectra was carried out in IGORpro.

All DFT calculations of were performed in Jaguar version 3.5 (1998 Schrodinger, Inc.)[49] running on a single Pentium III processor. Calculations of monomeric ruthenium clusters were preformed with B3LYP/ LACVP** [50] level of theory, and the bridging ligand pyrazine with B3LYP/6-31G*.

3.10 References

(1) Creutz, C.; Taube, H. *J. Am. Chem. Soc.* **1969**, *91*, 3988.

(2) Hush, N. S. *Prog. Inorg.Chem.* **1967**, *8*, 391.

(3) Robin, M. B.; Day, P. *Adv. Inorg. Chem. Radiochem.* **1967**, *10*, 247.

(4) Brunschwig, B. S.; Sutin, N. *Coord. Chem. Rev.* **1999**, *187*, 233.

(5) Chisholm, M. H. *Proc. Natl. Acad. Sci.* **2007**, *104*, 2563.

(6) Demadis, K. D.; Hartshorn, C. M.; Meyer, T. J. *Chem. Rev.* **2001**, *101*, 2655.

(7) Oh, D. H.; Sano, M.; Boxer, S. G. *J. Am. Chem. Soc.* **1991**, *113*, 6880.

(8) Reimers, J. R.; Hush, N. S. *Chem. Phys.* **1996**, *208*, 177.

(9) Ondrechen, M. J.; Ko, J.; Zhang, L. T. *J. Am. Chem. Soc.* **1987**, *109*, 1672.

(10) D'alessandro, D. M.; Topley, A. C.; Davies, M. S.; Keene, F. R. *Chem. Eur. J.* **2006**, *12*, 4873.

(11) Petrov, V.; Hupp, J. T.; Mottley, C.; Mann, L. C. *J. Am. Chem. Soc.* **1994**, *116*, 2171.

(12) Hupp, J. T.; Dong, Y. H. *Inorg. Chem.* **1994**, *33*, 4421.

(13) Brunschwig, B. S.; Creutz, C.; Sutin, N. *Chem. Soc. Rev.* **2002**, *31*, 168.

(14) Glover, S. D.; Goeltz, J. C.; Lear, B. J.; Kubiak, C. P. *Eur. J. Inorg. Chem.* **2009**, 585.

(15) D'Alessandro, D. M.; Keene, F. R. *Chem. Soc. Rev.* **2006**, *35*, 424.

(16) Horng, M. L.; Gardecki, J. A.; Papazyan, A.; Maroncelli, M. *J. Phys. Chem.* **1995**, *99*, 17311.

(17) Simon, J. D. *Acc. Chem. Res.* **1988**, *21*, 128.

(18) Weaver, M. J. *Chem. Rev.* **1992**, *92*, 463.

(19) Lear, B. J.; Glover, S. D.; Salsman, J. C.; Londergan, C. H.; Kubiak, C. P. *J. Am. Chem. Soc.* **2007**, *129*, 12772.

(20) Salsman, J. C.; Ronco, S.; Londergan, C. H.; Kubiak, C. P. *Inorg. Chem.* **2006**, *45*, 547.

(21) Ito, T.; Hamaguchi, T.; Nagino, H.; Yamaguchi, T.; Washington, J.; Kubiak, C. P. *Science* **1997**, *277*, 660.

(22) Ito, T.; Hamaguchi, T.; Nagino, H.; Yamaguchi, T.; Kido, H.; Zavarine, I. S.; Richmond, T.; Washington, J.; Kubiak, C. P. *J. Am. Chem. Soc.* **1999**, *121*, 4625.

(23) Sutin, N. In *Electron Transfer-from Isolated Molecules to Biomolecules, Pt 1* **1999**; Vol. 106, p 7.

(24) Londergan, C. H.; Salsman, J. C.; Ronco, S.; Dolkas, L. M.; Kubiak, C. P. *J. Am. Chem. Soc.* **2002**, *124*, 6236.

(25) Chen, P.; Meyer, T. J. *Inorg. Chem.* **1996**, *35*, 5520.

(26) Glover, S. D.; Goeltz, J. C.; Lear, B. J.; Kubiak, C. P. *Coord. Chem. Rev.* **2010**, *254*, 331.

(27) Zhang, L. T.; Ko, J. J.; Ondrechen, M. J. *J. Phys. Chem.* **1989**, *93*, 3030.

(28) Ferretti, A.; Lami, A.; Ondrechen, M. J.; Villani, G. *J. Phys. Chem.* **1995**, *99*, 10484.

(29) Londergan, C. H.; Kubiak, C. P. *J. Phys. Chem. A* **2003**, *107*, 9301.

(30) Sutin, N. J. *Prog. Inorg. Chem.* **1983**, *30*, 441.

(31) Crutchley, R. J. *Adv. Inorg. Chem.* **1994**, *41*, 273.

(32) Grozema, F. C.; Berlin, Y. A.; Siebbeles, L. D. A.; Ratner, M. A. *J. Phys. Chem. B* **2010**, *114*, 14564.

(33) Kurnikov, I. V.; Tong, G. S. M.; Madrid, M.; Beratan, D. N. *J. Phys. Chem. B* **2002**, *106*, 7.

(34) Lewis, F. D.; Wu, Y. S.; Zhang, L. G.; Zuo, X. B.; Hayes, R. T.; Wasielewski, M. R. *J. Am. Chem. Soc.* **2004**, *126*, 8206.

(35) Reimers, J. R.; Hush, N. S. *Chem. Phys.* **1993**, *176*, 407.

(36) Blackburn, J. L.; Selmarten, D. C.; Ellingson, R. J.; Jones, M.; Micic, O.; Nozik, A. J. *J. Phys. Chem. B* **2005**, *109*, 2625.

(37) Cai, X. C.; De, P. K.; Anyaogu, K. C.; Adhikari, R. M.; Palayangoda, S. S.; Neckers, D. C. *Chem. Comm.* **2009**, 1694.

(38) Lear, B. J.; Chisholm, M. H. *Inorg. Chem.* **2009**, *48*, 10954.

(39) Glover, S. D.; Lear, B. J.; Salsman, C.; Londergan, C. H.; Kubiak, C. P. *Phil.Trans. Roy. Soc. A* **2008**, *366*, 177.

(40) Londergan, C. H.; Rocha, R. C.; Brown, M. G.; Shreve, A. P.; Kubiak, C. P. *J. Am. Chem. Soc.* **2003**, *125*, 13912.

(41) Rocha, R. C.; Brown, M. G.; Londergan, C. H.; Salsman, J. C.; Kubiak, C. P.; Shreve, A. P. *J. Phys. Chem. A.* **2005**, *109*, 9006.

(42) Londergan, C. H.; Salsman, J. C.; Lear, B. J.; Kubiak, C. P. *Chem. Phys.* **2006**, *324*, 57.

(43) Kumar, K.; Kurnikov, I. V.; Beratan, D. N.; Waldeck, D. H.; Zimmt, M. B. *J. Phys. Chem. A* **1998**, *102*, 5529.

(44) Hush, N. S. *Electrochim. Acta* **1968**, *13*, 1005.

(45) Vath, P.; Zimmt, M. B.; Matyushov, D. V.; Voth, G. A. *J. Phys. Chem. B.* **1999**, *103*, 9130.

(46) Pekar, S. *Zh Eksp Teor Fiz+* **1946**, *16*, 341.

(47) Lambert, C.; Noll, G.; Schelter, J. *Nature Mat.* **2002**, *1*, 69.

(48) Launay, J.-P.; Coudret, C.; Hortholary, C. *J. Phys. Chem. B.* **2007**, *111*, 6788.

(49) JAGUAR v 3.5; Schrodinger; Portland, OR, 1998.

(50) Hay, P. J.; Wadt, W. R. *J. Chem. Phys.* **1985**, *82*, 299.

Note: This chapter is a full reproduction of the publication S.D. Glover, C.P Kubiak "Persistence of the three-state description of mixed valency at the localized-to-delocalized transition." *Journal of the American Chemical Society*, **2011**, *accepted,* of which the dissertation author is the primary author.

Chapter 4

2D IR spectroscopy for temporal resolution of ultrafast electron transfer

4.1 Introduction

The focus of the previous two chapters was to understand the dynamics of ultrafast electron transfer reactions in mixed valence ruthenium dimer-of-trimers. In each technique used, FTIR and UV-VIS NIR spectroscopy, a spectrum is collected and averaged over a timescale of many seconds. This means that during the collection of a spectrum, trillions of intramolecular electron transfer reactions have taken place. Dynamic behavior occurring on the timescale of light frequencies implemented during the experiment will thus appear averaged. An example of this was shown in Figure 3.1, where dimer-of-trimers show ν(CO) bandshapes that are broad and coalesced, implying a rate of intramolecular electron transfer on the the vibrational timescale, or picoseconds.[1] Another classic example of spectral coalescence comes from the study of (η^4-diene)irontricarbonyls that exhibit picosecond isomerization.[2,3] In the same manner that rate constants are extracted from coalesced NMR spectra, Bloch lineshape analysis has been applied to determine rate constants for infrared spectra.[3,4]

To date, Bloch lineshape analysis is the only method used for rate constant determination in hexaruthenium dimer-of-trimer complexes.[1] It is known that there are many contributions to IR bandshapes[4] and there has been much heated discussion on whether it is possible to discriminate between genuine chemical exchange and "pseudocollapse" from a coalesced 1D bandshape.[4-7] Because all rate constants in mixed valence dimers have been estimated by the degree of coalescence, it is of great interest to determine by a direct method of the rate of intramolecular electron transfer. Time resolved two-dimensional infrared (2D IR) spectroscopy is a technique which could provide a direct measure of the rate constant for electron transfer and further our understanding of the dynamics of ultrafast electron transfer.

4.2 Two dimensional infrared spectroscopy theory

The concept of 2D IR spectroscopy was first realized by Isao Noda working for Proctor & Gamble Company in 1989 as a novel time-resolved IR technique.[8] In this initial study 2D IR was used to improve spectral resolution of overlapped 1D IR features, and detect intramolecular vibrational interactions of polymeric solutions. Since its inception less than three decades ago, 2D IR has become a widely used technique for elucidation of time-resolved ultrafast molecular dynamics.[9]

In principle, 2D IR spectroscopy is analogous to two-dimensional correlation NMR spectroscopy, which measures scalar coupling in spin-spin coupled nuclei by a coherence transfer mechanism. Molecular vibrational couplings are the main concern of 2D IR spectroscopy. The timescale of nuclear spin relaxation is 10^3 –10^6 s^{-1} as compared with vibrational relaxation, which is six to ten orders of magnitude faster. The relevant timescale for the study of dynamics by 2D IR is thus, picoseconds to femtoseconds. With this in mind, 2D IR has been dedicated to the study of ultrafast dynamic behavior such as intramolecular vibrational energy exchange, structural

isomerization, and solution dynamics.[9] The picosecond electron transfer reaction in Ru_3O dimers of trimers begs for study by 2D IR, where time resolved measurements may quantify the dynamics of electron transfer.

Two prevailing 2D IR techniques are widely employed in the spectroscopic community; (1) dynamic hole burning, or double resonance 2D IR, and (2) pulsed Fourier Transform (FT), or heterodyne detected vibrational echo 2D IR. Either technique leads to analogous spectral time resolution and intensities, though the temporal pulse sequences are quite different.[10] Pulsed FT 2D IR utilizes a series of three (broad ~200 cm^{-1}) femtosecond laser pulses followed by a "photon echo" pulse that is emitted from the sample.[9] The three pulsed are tuned to the vibrational region of interest and affect the sample oscillators as follows: the first pulse places oscillators in a coherent $\nu = 0 \rightarrow \nu = 1$ superposition, the second labels oscillators in time and the third pulse brings oscillators back into coherence. Reaction dynamics take place during the time between the second and third pulse, which is varied throughout the experiment in order to allow for shorter or longer interaction times. It is through the variation of time between the second and third pulse (T_w) that time resolution in realized. The fourth pulse is emitted by the sample and is subject to interference with a separate local oscillator pulse (heterodyne) to obtain phase information.[11] Axes of 2D FTIR spectra are Fourier transformed with respect to the time in between the first and second pulse (dependent or y-axis) and to the time spanning the second and third pulse (independent or x-axis) yielding frequency domain axes. Two separate attempts to study ultrafast electron transfer of compound **2**$^-$ by FT 2D IR under the supervision of M. D. Fayer (Stanford) and Nien-He Ge (University of California Irvine) have been inconclusive due to lack of sufficient data and sample degradation by atmospheric contamination.

The second 2D IR method, dynamic hole burning, is in essence a vibrational pump-probe experiment.[10] Samples are pumped with an ultrashort laser pulse, from which a narrow slice of frequencies (5-15 cm^{-1}) are selected with a Fabry-Perot filter. The sample is subsequently probed with a broad (200 cm^{-1}) laser pulse after a chosen waiting time. The pump and probe frequencies compose the vertical and horizontal axis, respectively. Figure 4.1 shows representative pump and probe bandshapes that make up the axes of the 2D IR spectrum a schematic 2D IR spectrum. Peaks along the diagonal of the 2D spectrum represent a 1D FTIR. These peaks appear as negative intensities as the pump pulse depopulates the ground state via the $\nu = 0 \rightarrow 1$ transition. This in turn populates the $\nu = 1$ state and appearing as positive intensities (offset from the diagonal) are peaks corresponding to the $\nu = 1 \rightarrow 2$ transition. The positive intensities appear offset from the diagonal due to anharmonicity.[9,10] Figure 4.2 is a vibrational level energy diagram for two coupled anharmonic oscillators a and b whose quantum states can be represented by $|ab\rangle$ and $|ba\rangle$, respectively. The energy levels that need to be considered are the ground vibrational state, $|00\rangle$, two single quantum states $|01\rangle$ and $|10\rangle$, and three double quantum states $|02\rangle$, $|20\rangle$, and $|11\rangle$, a combination band. It is assumed that prior to the pump, the vibrators are primarily in the ground state (i.e., the Boltzmann population mostly in the ground state), $|00\rangle$. The pump probe will supply sufficient energy to the system such that all the transitions shown in Figure 4.2 are possible. Allowed transitions are shown with arrows in with red indicating positive intensity (population of vibrational level) and blue indicating negative intensity (de-population or bleach). Cross peaks, shown in the off-diagonal region of the spectrum, occur by exchange of vibrational energy between $|01\rangle$ and $|10\rangle$ states. This point will be of particular importance to the discussion in section three of this chapter. The x-axes of 2D IR spectra are horizontal slices in the probe frequency direction obtained at various pump frequencies. A simple analogy to the double

resonance experiment is the following: the pump pulse provides an initial "jolt" of vibrational excitation energy, and the probe pulse takes an infrared "picture" of the system as vibrational relaxation ensues. Examination of time resolved 2D spectra can provide details of vibrational relaxation pathways, and reveal whether any of those pathways are intramolecular exchange processes.

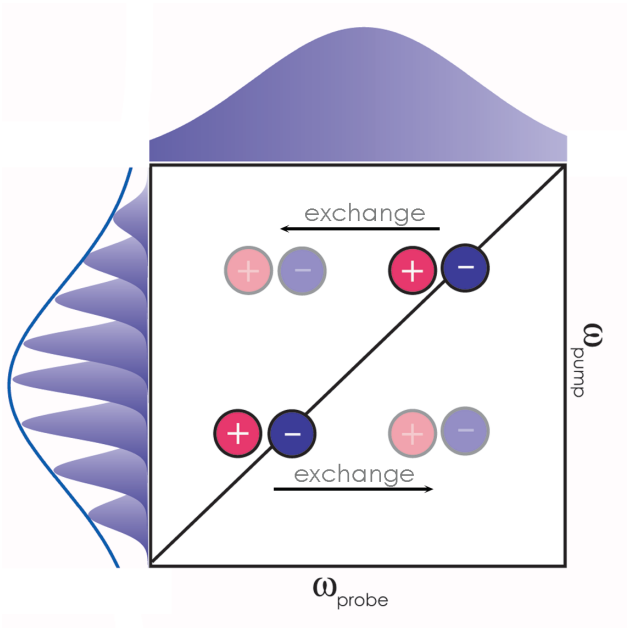

Figure 4.1. A representative 2D IR spectrum with pump and probe pulses included along y and x-axes, respectively. Each horizontal slice is a transient absorption spectrum at the pump frequency along the probe axis. Should exchange or energy transfer occur, off diagonal peaks will appear on the timescale of that dynamic process.

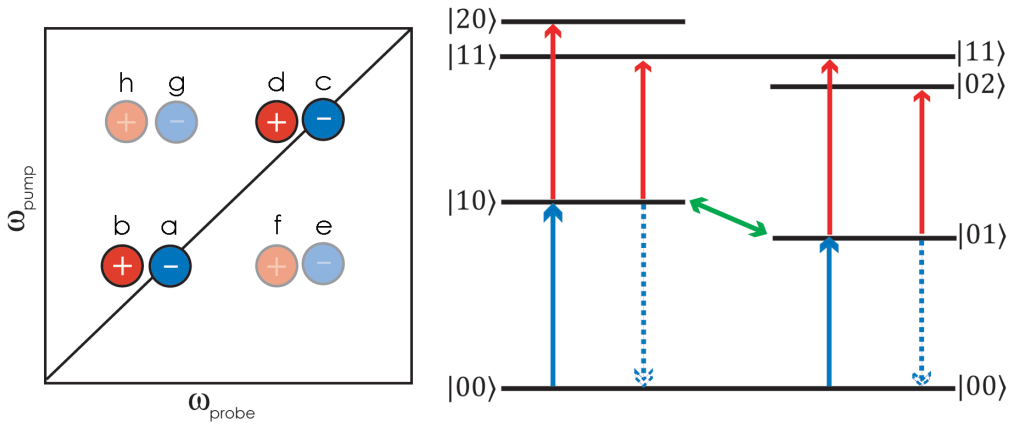

Figure 4.2. Shown is a representative 2D IR spectrum (left) and corresponding energy level diagram (right) showing vibrational transitions. The peaks appearing in the 2D spectrum correspond to the following transitions: **a** ($|00\rangle \rightarrow |10\rangle$ and $|10\rangle \rightarrow |00\rangle$), **b** ($|10\rangle \rightarrow |20\rangle$), **c** ($|00\rangle \rightarrow |01\rangle$ and $|01\rangle \rightarrow |00\rangle$), **d** ($|01\rangle \rightarrow |02\rangle$), **e** ($|00\rangle \rightarrow |01\rangle$), **f** ($|10\rangle \rightarrow |11\rangle$), **g** ($|00\rangle \rightarrow |10\rangle$), and **h** ($|01\rangle \rightarrow |11\rangle$). The off diagonal pair, **fe**, corresponds to exchange of **ba** to **dc**. The off diagonal pair **hg** corresponds to exchange of **dc** to **ba**.

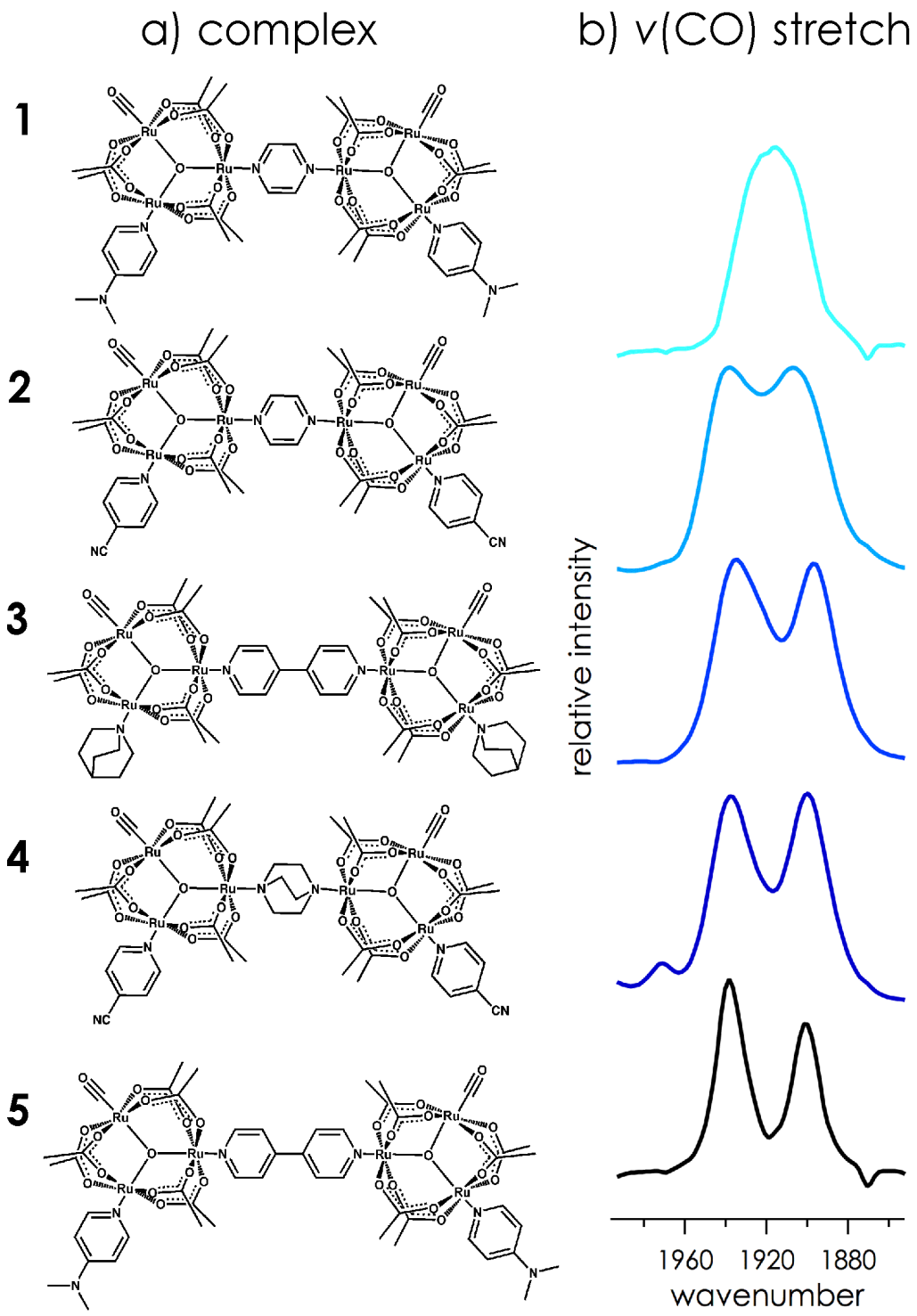

Figure 4.3. **(a)** Dimers prepared for 2D IR studies. These dimers were chosen because of the wide range of coalescence in ν(CO) spectra. **(b)** IR bandshapes to corresponding mixed valence dimers in acetonitrile at 298 K are shown where **5**- displays the least coalescence and **1**- the most. Simulated rate constants range from 3.75 × 11 s^{-1} (**5**) to 2.8 × 12 s^{-1} (**1**).

4.3 Dynamic hole burning 2D IR spectroscopy of ruthenium dimers of trimers

2D IR spectroscopy was carried out in order to ascertain the timescale for electron transfer in mixed valence systems [$Ru_3O(OAc)_6(CO)(py)$-BL-$Ru_3O(OAc)_6(CO)(py)$], where BL is the bridging ligand. A series of mixed valence dimers was chosen such that vibrational dynamics could be probed in dimers possessing varying degrees of ν(CO) coalescence (Figure 4.3). Additionally, 2D IR experiments were preformed on neutral dimers. By comparing 2D spectra and kinetics of mixed valence and neutral dimers we may differentiate between intrinsic vibrational dynamics and vibrational dynamics due to exchange. A second point, of keen importance concerns the nature of coalescence in vibrational spectra. Does coalescence in infrared spectra imply that a system possesses picosecond fluxional behavior? There is currently no consensus on this point, and it can be very experimentally challenging to make the distinction between "pseudo collapse" and coalescence.[2,3,5] Pseudo collapse, which can lead to coalescence, arises when oscillators sample different harmonics within their own potential well, but don't experience exchange between potential wells.[4] This is discussed further in section 3 of Chapter 5. For the most complete picture of mixed valency at the Class II/III limit, it is in our interest to understand, to the best of our abilities, the dynamics that are the cause of ν (CO) bandshapes of our mixed valence dimers.

Figure 4.4 shows 2D IR spectra of the neutral dimer **2** with 2, 7, and 10 ps waiting time. The orange (positive) and blue (negative) intensities correspond to the $\nu = 1 \rightarrow 2$ and $\nu = 0 \rightarrow 1$, respectively. The slight diagonal slant in the bandshapes of 2D spectrum after 2 ps pump-probe delay is likely from inhomogeneous broadening which can occur when oscillators interact with surrounding solvent molecules. In the 1D IR neutral complexes **1** - **5** all show a single carbonyl stretching frequency due to symmetry. In a 2D IR spectrum neutral complexes will have the two intensities; the "hole"

corresponding to the $\nu = 0 \rightarrow 1$ transition and the positive peak for the $\nu = 1 \rightarrow 2$ transition. The $\nu = 1 \rightarrow 2$ transition is offset from the diagonal by ~25 cm^{-1} along the probe axis due to anharmonicity. Differentiation between carbonyl sites on a neutral dimer system can be achieved by isotopic labeling in one of the carbonyls in the dimer. Isotopic labeling will provide the experimental control for investigation of exchange pathways in neutral complexes.

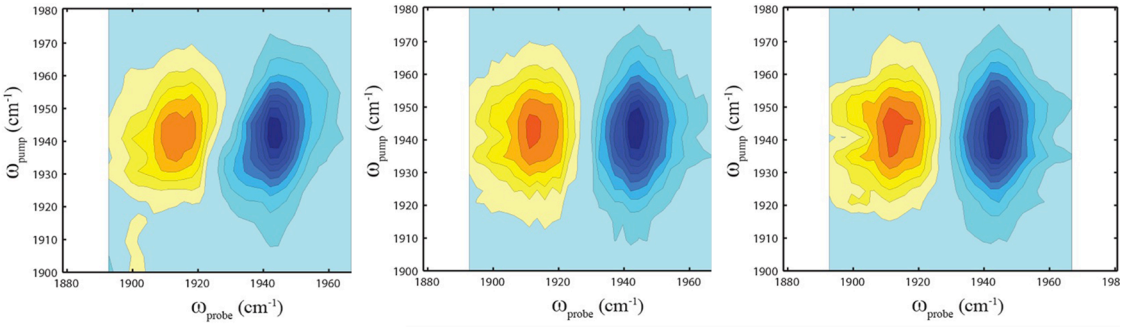

Figure 4.4. 2D spectra of neutral dimer 2 in methylene chloride after 2 ps (left), 7 ps (middle), and 10 ps (right) waiting times in between pump and probe pulse. Each spectrum is normalized to either the tallest peak or deepest hole.

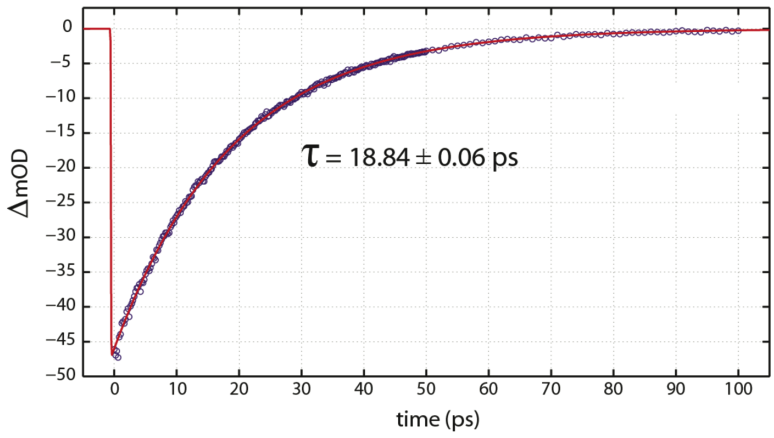

Figure 4.5. Vibrational decay of the bleach excited state for **2** in methylene chloride. The lifetime of relaxation is 18.84 picoseconds. The unit along the y-axis, ΔmOD, is the change in optical density on the milli-scale.

Vibrational lifetime kinetics can also be obtained for individual peaks in a 2D spectrum by broadband IR pump-probe experiments.[12] For example, a broadband pump tuned to the center frequency of the ν =0 → 1 of **2** at 1940 cm^{-1} depletes the ground state population and manifests as a negative intensity (or hole) in the spectrum. Vibrational relaxation will repopulate the ground state leading to the returned intensity in the pumped spectral region. Plotting the change in intensity versus waiting time between pulses will show vibrational decay of excited states. Fitting the time dependent changes in intensity to an exponential decay will give time constants for relaxation. The plot in Figure 4.5 shows vibrational decay of the bleach in the 2D spectrum. The decay curve fits to a mono-exponential decay giving a lifetime of 18.84 $\pm$ 0.6 ps. This tells us that after an initial excitation of vibrational population from the ground state, $1/e$ of that population has returned to the ground state after 18.8 picoseconds.

A 2D dynamic hole burning IR on a neutral dimer is not terribly interesting for a study of mixed valence dynamics, as there is no electron transfer reaction. Much more interesting is the study of mixed valence complexes where dynamic exchange of an electron is expected. Figure 4.6 shows 2D spectra of **2**$^-$ in methylene chloride with 1, 2, 3, and 5 ps waiting times. The blue peak pair along the diagonal corresponds to the 1D FTIR spectrum of **2**$^-$ and the orange peak pair offset from the diagonal is the ν =1 → 2 anharmonic transition. The 1D FTIR of **2**$^-$ in Figure 4.3 shows that the mixed valence ν(CO) peak is quite deeply coalesced. In the 2D spectrum this becomes apparent in that the peaks along the diagonal are not cleanly separated. Inspection of the four spectra shows that in all cases there is no distinct cross peak formation. This is at first a troubling result, and one that was observed for all dimers in this study. A number of plausible explanations for the lack of distinguished cross peaks in the spectra that follow will be outlined.

Figure 4.7 shows 2D IR spectra for a neutral valence dimer in methylene chloride which is related to complex **2**, $[Ru_3O(OAc)_6(cpy)(^{13}CO)\text{-}pz\text{-}(CO)(cpy)(OAc)_6Ru_3O]$, where one carbonyl has been isotopically substituted to ^{13}CO. Spectra with waiting times of 2, 4, 7, 10 and 15 ps between pump and probe pulses are shown. The kinetics trace shown in Figure 4.7 is correspond the $\nu(^{13}CO)$ vibrational lifetime. There are some notable differences between the spectra shown for the mixed valence complex **2**$^-$ and the corresponding neutral complex shown in Figures 4.6 and 4.7, respectively. Spectra for the **2**$^-$ mixed valence species are significantly broadened along the diagonal, which is consistent with the coalescence observed in 1D spectra. There is also a diagonal slant in the contours of the spectra for **2**$^-$ with 2 and 4 picosecond waiting times, which is likely due to inhomogeneous broadening. By comparison, the spectra for the neutral istopically labeled analogue show distinctly separated peaks with no evidence of diagonal broadening. The kinetic lifetimes for the low frequency mode are also quite different for the neutral and mixed valence variants. The mixed valence species **2**$^-$ displays bimodal vibrational relaxation, as evidenced with the bi-exponential decay curve fit, with time constants of 2.6 and 9.8 picoseconds. This implies that there are likely two pathways of relaxation in the $\nu = 1 \rightarrow 0$ transition. The kinetic lifetimes for the low frequency $\nu(^{13}CO)$ (Figure 4.7) mode and the $\nu(CO)$ (Figure 4.4) mode of the neutral analogue, however, show mono-exponential decay with a time constant of 14.1 and 18.8 picoseconds, respectively. There is a clear difference in the relaxation kinetics between neutral and mixed valence complex of **2**.

Inspection of the spectra for **1**$^-$, in Figure 4.8, and the neutral isotopic analogue, $[Ru_3O(OAc)_6(dmap)(^{13}CO)\text{-}pz\text{-}(CO)(dmap)(OAc)_6Ru_3O]$, in Figure 4.9, show similar qualitative and quantitative features when compared to the spectra of **2** and **2**$^-$. Again, in the mixed valence species there is significant coalescence along the

diagonal of the spectrum and broadening in spectra corresponding to earlier waiting times. In neutral complex spectra there is no diagonal broadening and low and high frequency peaks are cleanly separated. Quantitatively, the kinetics traces show similar behavior; faster bi-exponential kinetics (time constants of 2.3 and 9.2 picoseconds) in the mixed valence species, and slower mono-exponential kinetics (13.0 picoseconds) in the neutral species.

The spectra depicted in Figure 4.10 are for **3**$^-$ with waiting times of 2, 4, 7, 10 and 15 picoseconds. The 1D spectrum for **3**$^-$ given in figure 3 shows less coalescence in the ν(CO) bandshape than for **2**$^-$ and **1**$^-$. This quality of the ν(CO) bandshape is also present in the 2D spectra of figure 10, where there is clean peak separation between high and low frequency modes along the diagonal. The kinetics trace of the vibrational relaxation in the low frequency mode displays mono-exponential kinetics with a time constant of 10 picoseconds. This is in contrast to the mixed valence species **1**$^-$ and **2**$^-$, which have significant bandshape coalescence and display bi-exponential kinetics, *vide infra*. The complex displaying the least spectral coalescence in 1D IR spectra, ***5***$^-$, also share similar 2D spectra qualities with **3**$^-$, in that there is clean separation of ν (CO) stretches along the diagonal owing to the lack of coalescence in ν (CO) bandshape. Additionally, the kinetics traces for ***5***$^-$ corresponding to peak lifetimes also fit to a mono-exponential decay as is with **3**$^-$. 2D IR Spectra of **4**$^-$ were also acquired, however, owing to the fact that they are so similar qualitatively and quantitatively to **3**$^-$ and ***5***$^-$, they have not been included here. The meaningful spectral data compiled thus far has been presented. Interpretation of these spectra will be presented in the following section.

Table 4.1 Vibrational lifetime time constants derived from kinetic traces of low frequency diagonal peaks. **1***=[$Ru_3O(OAc)_6$(dmap)(^{13}CO)-pz-(CO)(dmap)$(OAc)_6Ru_3O$] and **2*** = [$Ru_3O(OAc)_6$(cpy)(^{13}CO)-pz-(CO)(cpy)$(OAc)_6Ru_3O$], since these complexes are neutral no electron transfer is expected. Rates for electron transfer were obtained by Bloch lineshape analysis with the program *VibexGL*.[13]

Complex	τ_1(ps)	τ_2(ps)	Estimated k_{et} (ps)
1$^-$	2.3 ± 1.3	9.2 ± 3.5	0.55
2$^-$	2.6 ± 0.6	9.8 ± 3.4	0.91
3$^-$	10.0 ± 0.9	–	2.5
5$^-$	20.6 ± 1	–	2.59
1*	13.0 ± 0.2	–	–
2*	14.1 ± 0.2	–	–

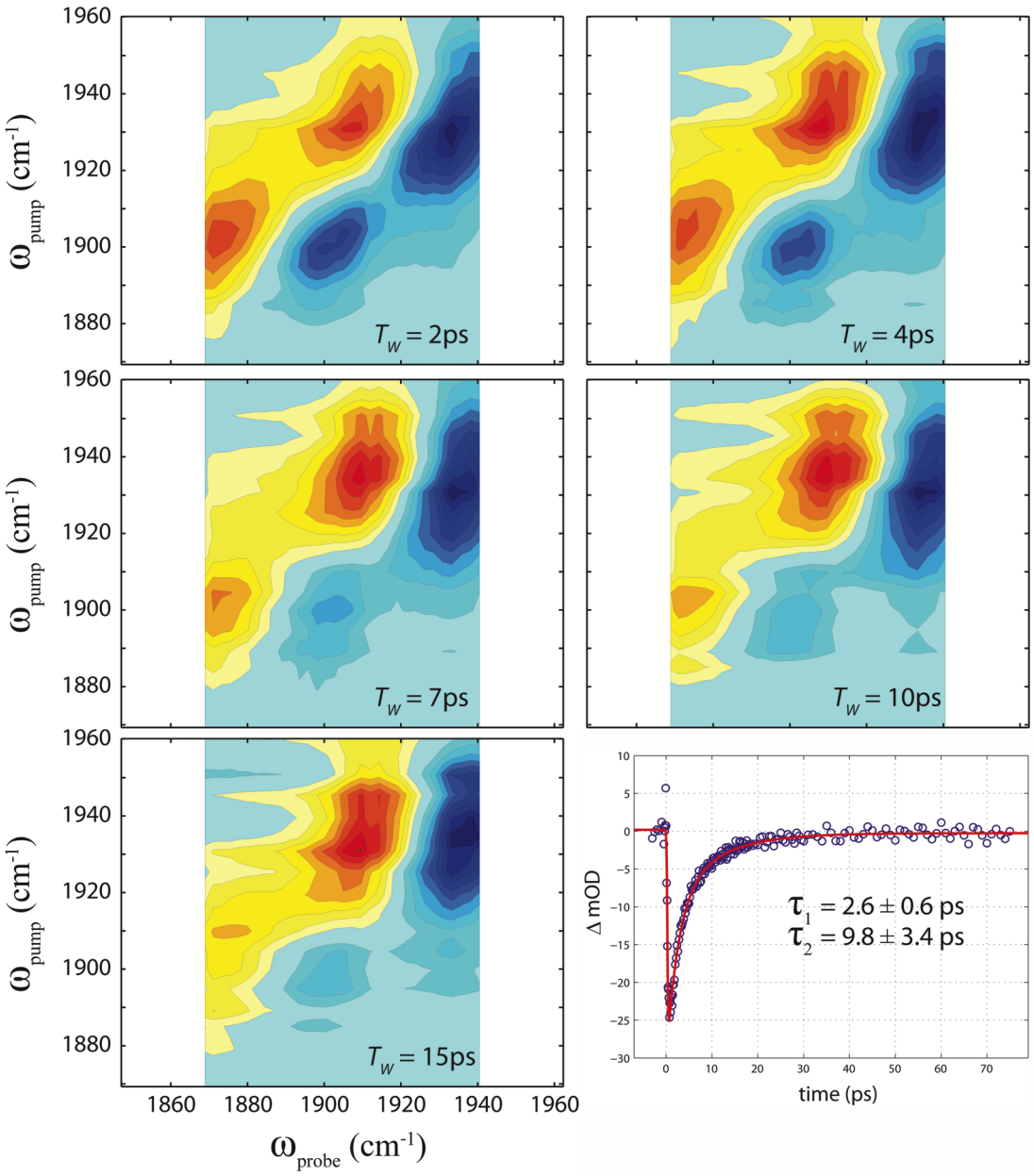

Figure 4.6. 2D spectra of mixed valence dimer **2**$^-$ in methylene chloride where the time between the pump and probe pulse (T_w) are 2, 4, 7, 10, and 15 picoseconds. The kinetics plot corresponds to the vibrational lifetime of the low frequency diagonal peak at ca.1900 cm^{-1}.

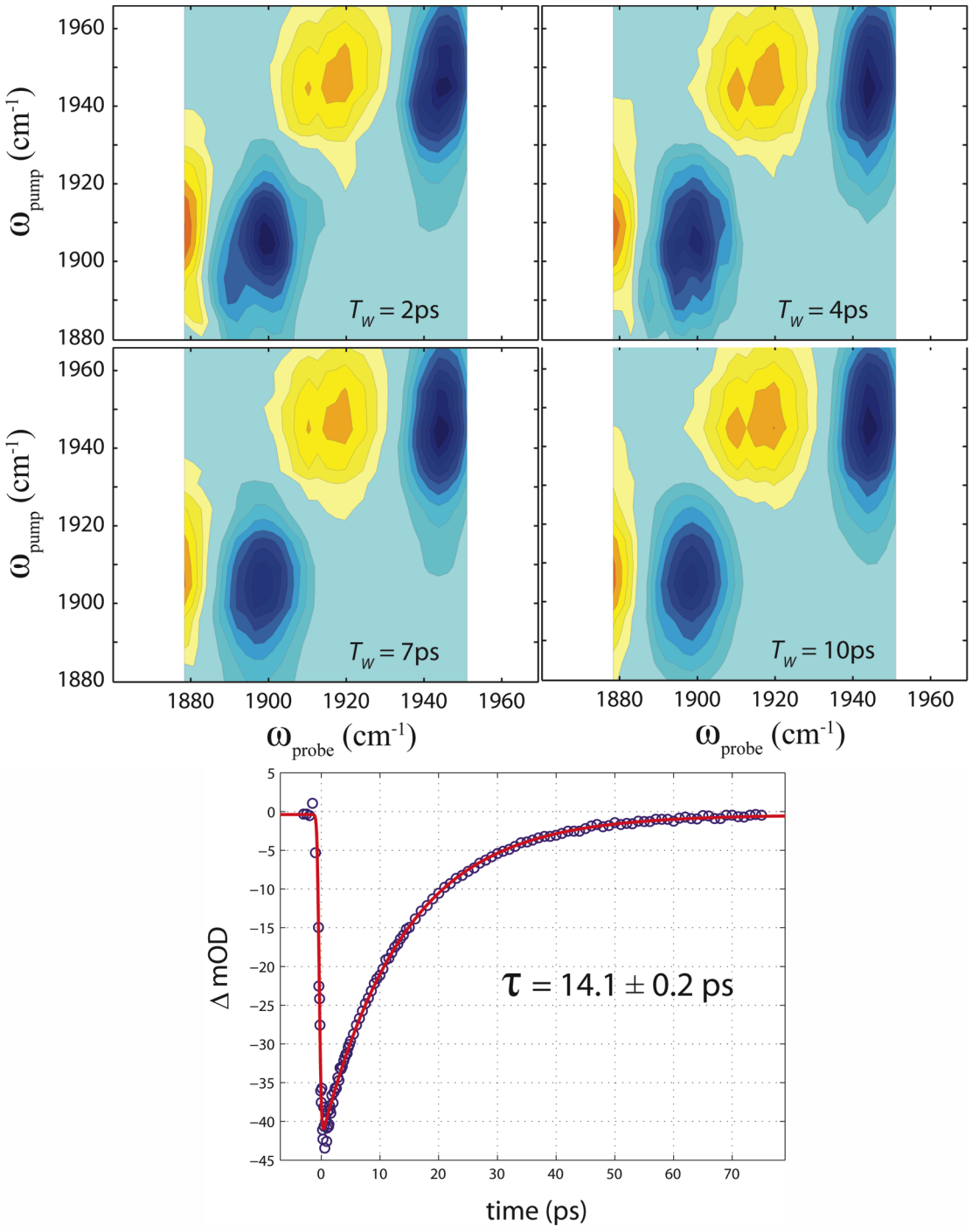

Figure 4.7. 2D spectra are shown for the neutral isotopically labeled dimer [$Ru_3O(OAc)_6(cpy)(^{13}CO)$-pz-$(CO)(cpy)(OAc)_6Ru_3O$] in methylene chloride after 2, 4, 7, and 10 picosecond waiting times. The kinetics trace is recorded for the low frequency diagonal peak at ca. 1898 cm-1. The low frequency diagonal peak in these spectra correspond to the $\nu(^{13}CO)$ band, and not from a reduced species.

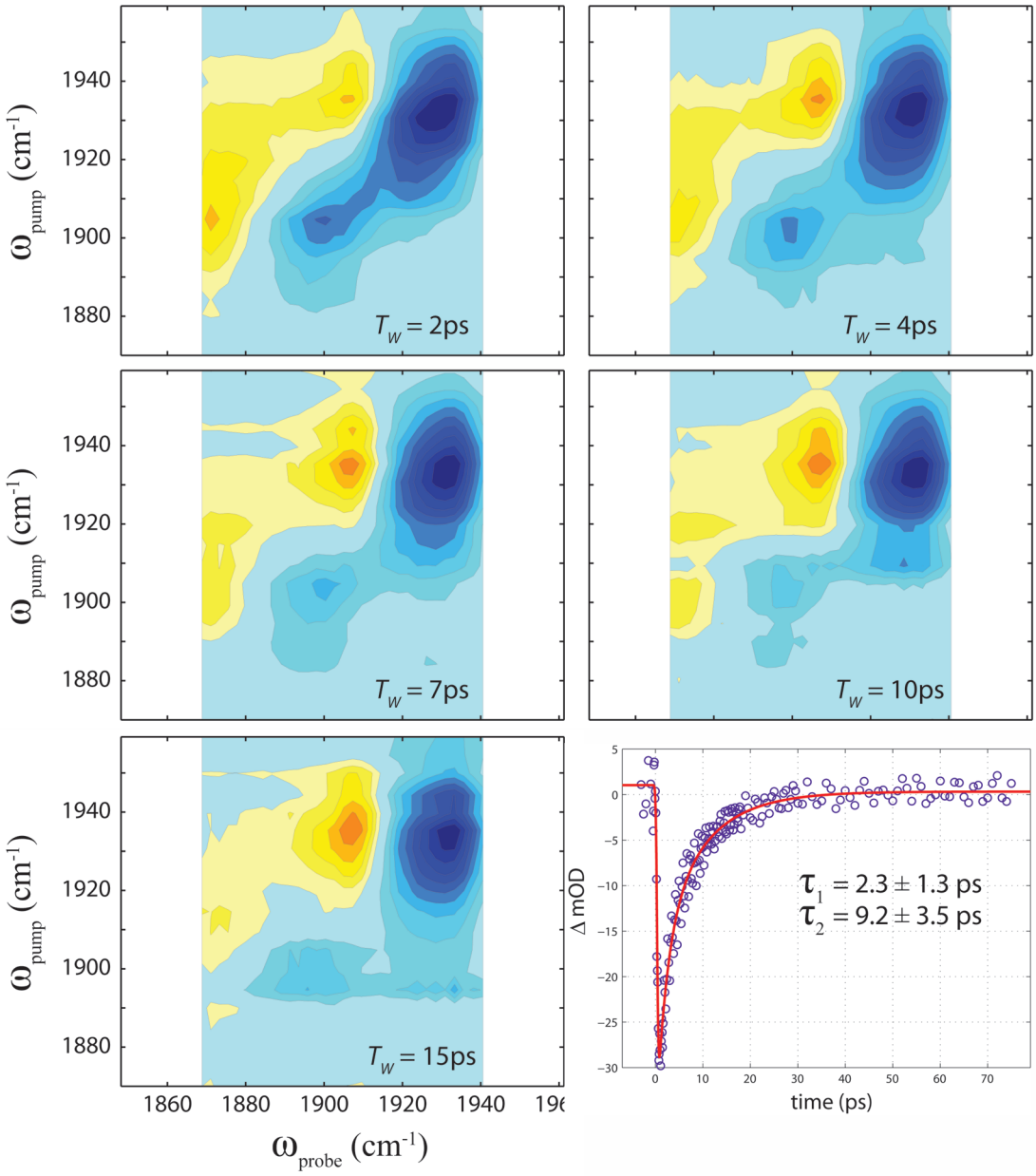

Figure 4.8. 2D spectra of mixed valence dimer **1**$^-$ in methylene chloride where the time between the pump and probe pulse (T_w) are 2, 4, 7, 10, and 15 picoseconds. The kinetics plot corresponds to the vibrational lifetime of the low frequency diagonal peak at ca.1898 cm^{-1}.

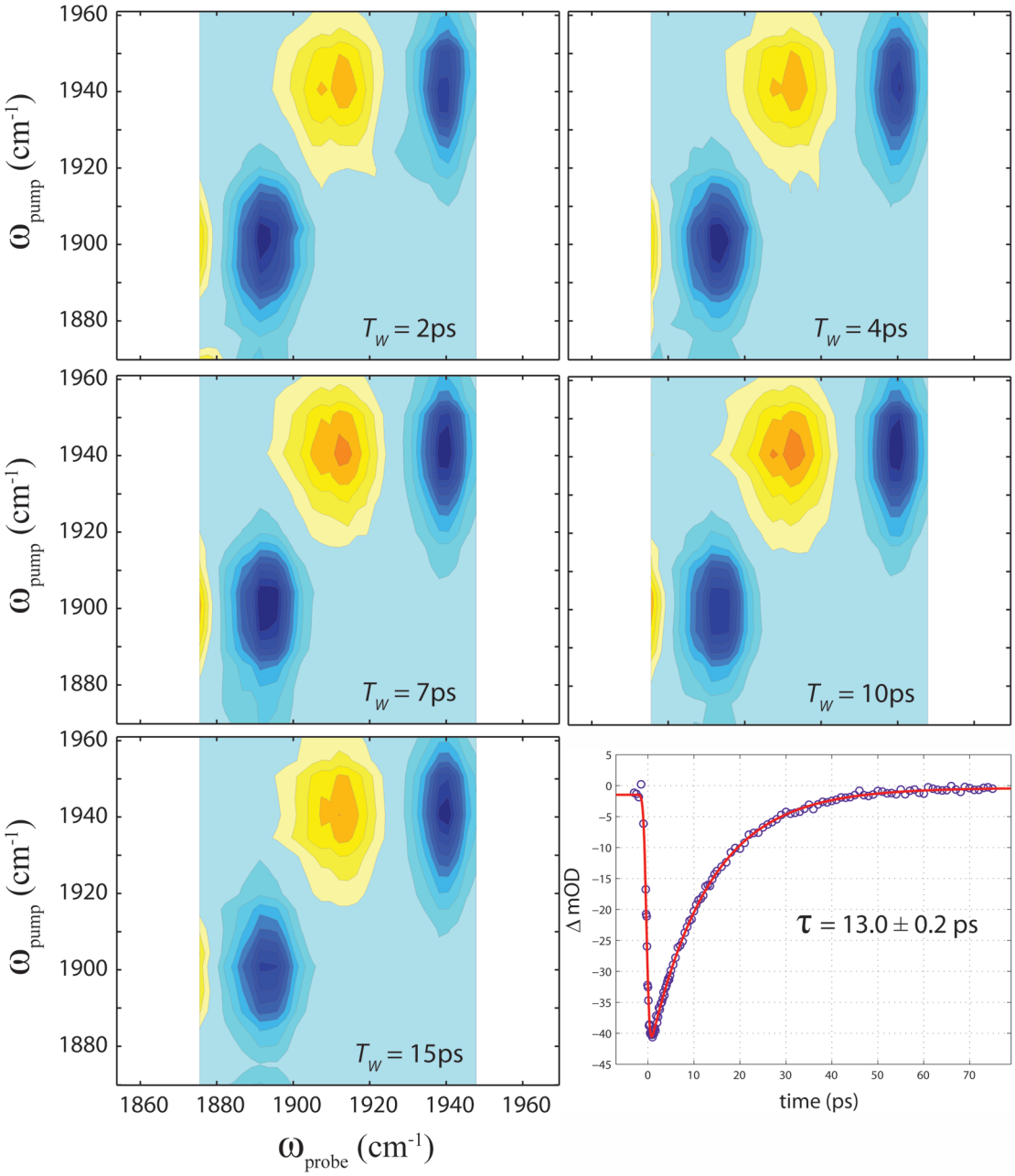

Figure 4.9. 2D spectra are shown for the neutral isotopically labeled dimer [$Ru_3O(OAc)_6(dmap)(^{13}CO)$-pz-$(CO)(dmap)(OAc)_6Ru_3O$] in methylene chloride after 2, 4, 7,10, and 15 picosecond waiting times. The kinetics trace is recorded for the low frequency diagonal peak at ca. 1895 cm^{-1}. The low frequency diagonal peak in these spectra correspond to the ν(^{13}CO) band, and not from a reduced species.

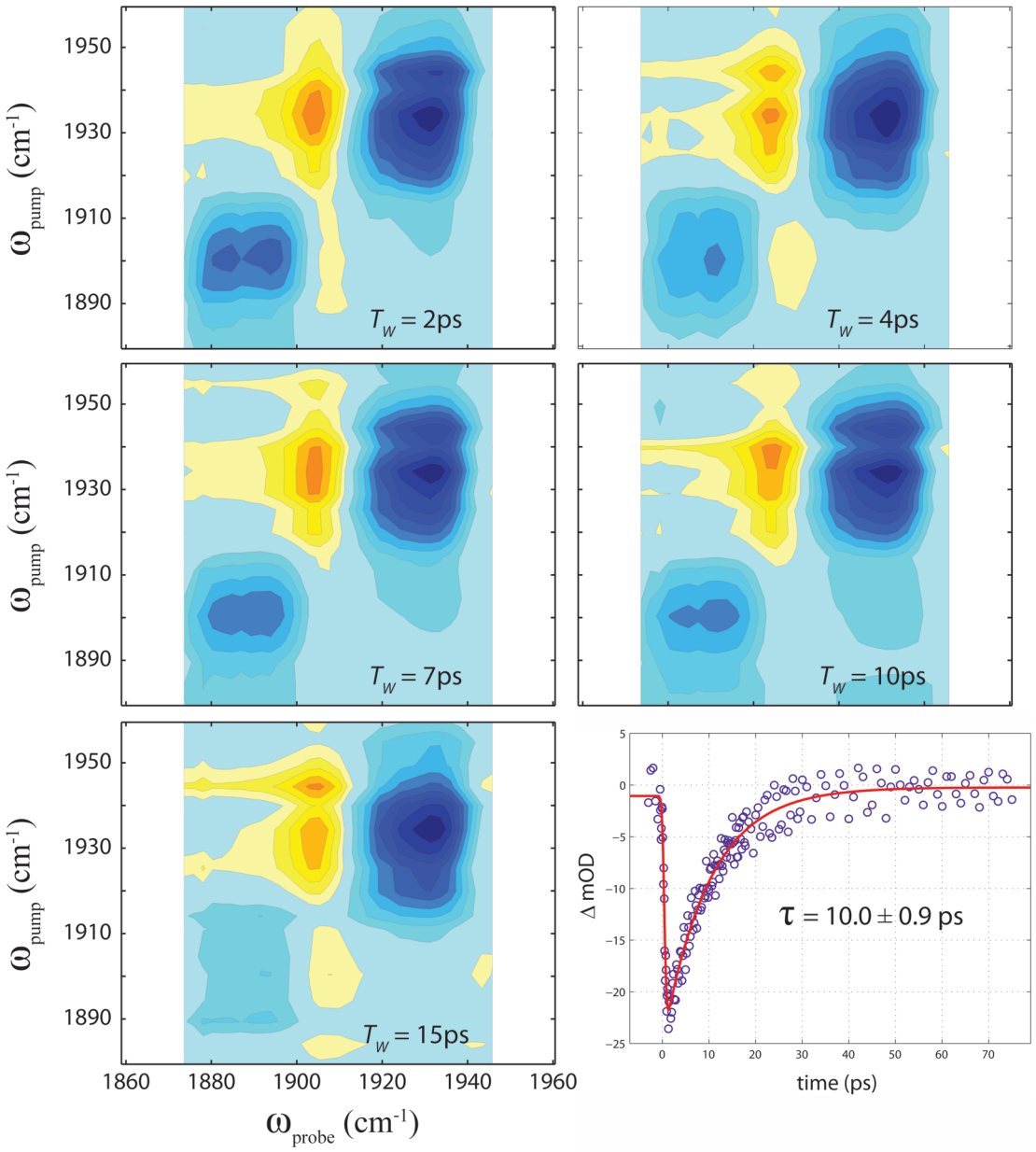

Figure 4.10. 2D spectra are shown for the dimer **3**$^{-}$ in methylene chloride after 2, 4, 7, 10 and 15 picosecond waiting times. The kinetics trace is recorded for the low frequency diagonal peak at ca. 1890 cm-1. The vibrational lifetime of the low frequency mode is 10 picoseconds.

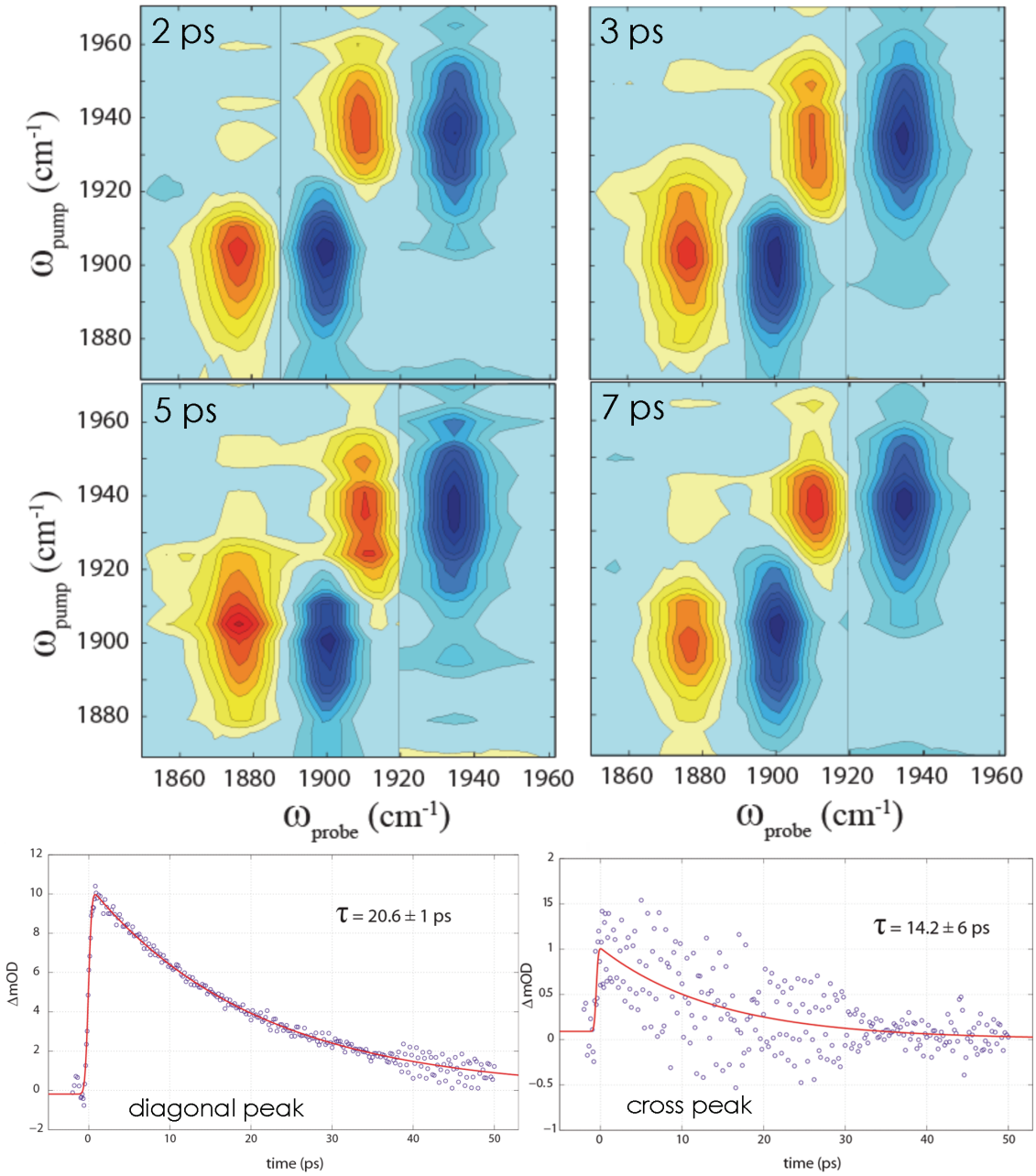

Figure 4.11. 2D spectra are shown for the dimer **5**$^{-}$ in methylene chloride after 2, 3, 5, and 7 picosecond waiting times. The kinetics trace is recorded for the low frequency diagonal peak at ca. 1875 cm^{-1}. The vibrational lifetime of the low frequency $\nu = 1 \rightarrow 2$ mode is 20.6 picoseconds. Lifetime kinetics were also recorded in the cross peak region of the spectrum at ca. 1880 cm^{-1} following an excitation pulse at 1936 cm^{-1}. The change in optical density of the cross peak trace is 10 times less than that of the diagonal peak.

4.4 Interpretation of 2D IR spectra lacking cross peaks

The 1D IR spectra of complexes **1**$^-$ – **5**$^-$, and others dimers like them, have been a key feature in studies of our mixed valence systems.[14] The coalesced quality of the ν(CO) spectra have been attributed to the fact that electron exchange is occurring with picosecond (vibrational) frequency.[1,4,14] This has been verified by numerous accompanying investigations into the electrochemical,[15] vibronic,[16,17] solvent dynamic and temperature dependent[18-20] properties of electron transfer in these systems. Furthermore, we can reliably predict the degree of coalescence, and by extension the relative rate of electron transfer, by knowing the electron donating ability of the ancillary ligands and relative bridge π^* orbital energies. With tunable ultrafast electron transfer rates, and the strong metal-carbonyl probe, these systems seem to be ideal for a 2D IR study.

Spectra shown in Figures 4.6 – 4.11, however, do not show cross peaks on the timescale of the 2D IR experiment. The timescale is of a 2D IR experiment is limited by the vibrational lifetime of excited vibrational mode. From the kinetics traces shown in Figures 4.6 – 4.11, the window of vibrational lifetime is approximately 10 – 15 ps for **1**$^-$ – **5**$^-$. This is a disconcerting result, as other metal carbonyl systems exhibiting fluxional behavior show strong cross peaks on the picosecond timescale.[12,21] For example, in the case of iron pentacarbonyl, in the 1D IR spectrum, e' and a_2" modes do not display a large degree of bandshape coalescence at high or low temperatures.[12] Double resonance 2D IR study of $Fe(CO)_5$ has revealed an 8 ps pseudo-rotation of the carbonyls, where this analysis was made possible by time resolved cross peak qunatification.

It is quite alarming that though mixed valence dimers display a high degree of coalescence, they do not exhibit cross peaks in 2D spectra. In the 2D spectra for **5**$^-$ there is a very small intensity in the cross peak region of the spectra for 3 and 5 ps

waiting times. Kinetics traces of spectral intensity in this region, however, show that this intensity is no larger than the noise baseline in spectra. This feature of the cross peak intensity becomes clear upon comparison to the kinetics trace of the off diagonal peak for the $v = 1 \rightarrow 2$ transition, Figure 4.11. The intense off diagonal peak kinetic trace for **5**$^-$ has approximately 1 ΔmOD of noise which can be clearly seen at 40 – 70 ps range of waiting times. This is in comparison to the kinetics trace of the cross peak region where the maximum intensity is approximately 1 ΔmOD in the T_w = 0 -10 ps range. Because each 2D spectrum is normalized to the peak of greatest intensity,[12] the noise baseline in a 2D spectrum can appear enhanced, especially at longer waiting times. So in the case of Figure 4.11 the small intensities in the cross peak region of the spectrum that was measured in the kinetics trace is likely an artifact of baseline noise. This assignment is strengthened by the fact that the maximum intensity from the kinetics plot in the cross peak region is the same as the noise level recorded for the diagaonal peak (Figure 4.11).

Spectra for **1**$^-$ and **2**$^-$, the fastest electron transfer systems, do not show cross peaks and neither do spectra for the non-exchanging experimental control systems (**1*** and **2***). Despite the lack of cross peaks in all mixed valence species, the kinetic traces display notable differences that deserve comment.

Table 4.1 summarizes kinetic lifetimes for low ν(CO) frequency modes of dimers in this study. For mixed valence dimers that show a high degree of coalescence in the 1D IR ν(CO) region **1**$^-$ and **2**$^-$, the lifetimes exhibit bi-exponential decay. Bi-exponential kinetics implies that there are two pathways for relaxation in faster systems. For dimers that have non-coalesced ν(CO) spectra, the lifetimes show mono-exponential decay, which indicates a single relaxation pathway. Without cross peak analysis it is not possible to make a definitive assignment as to the dynamic processes contributing to faster and slower relaxation pathways in **1**$^-$ and **2**$^-$. However, because the only

difference between **1**$^-$ and **2**$^-$ and the other species studied is the presence of a nearly delocalized exchanging electron, it is difficult to imagine a scenario where the additional faster pathway is not at least related to an effect of vibrationally fast mixed valency.

The fact that neutral non-exchanging dimers **1*** and **2*** have similarly behaved relaxation kinetics to the slow exchange systems **3**$^-$ and **5**$^-$ is strong evidence that the vibrational relaxation is not due to electron exchange and that k_{et} for these two slow systems is longer than 10 - 20 ps (i.e. the vibrational lifetime). The fact that the rate of electron transfer in **5**$^-$ is slower than the vibrational carbonyl lifetime is consistent with its lack of solvent dynamical dependence. Recall from Chapter 3 that **5**$^-$ was independent of solvent dynamical interactions. Due to the kinetic similarities between **1*** and **2*** and **3**$^-$ and **5**$^-$, it probable that any interesting dynamical information regarding electron transfer in these two mixed valence systems is slower than the applicable timescale for 2D IR.

We know from solvent and temperature dependent studies that in our highly electronically coupled mixed valence dimers (**1**$^-$ and **2**$^-$) that k_{et} is controlled by solvent dipolar reorientations in fluid solution.[19,20] This correlation of k_{et} with solvent dynamical modes is compelling evidence of picosecond electron transfer rates. Despite our evidence for picosecond electron transfer, there are no detectible cross peaks at any of the waiting times chosen for the hole burning experiment. The only evidence that something faster than 10 - 20 ps is occurring is from the additional faster time constant present in kinetic traces of diagonal peaks in 2D spectra. The fact that this time constant is not present in any but the solvent coupled, more coalesced samples, could be the result of faster vibrational relaxation due to some electron transfer pathway or related solvent coupling. That is to say that in the mixed valence state where

electronic communication is sufficient, there is some additional pathway which can divert excited state vibrational energy away from the carbonyl.

It is unfortunate, that with such a seemingly ideal system for a hole burning study, we cannot clearly identify dynamics in play especially those pertaining electron exchange. There could be a number of reasons why the dynamic hole burning experiment has failed to reveal the details we desire. Perhaps the simplest explanation for the lack of cross peaks is that the electron transfer lifetime is slower than 10 picoseconds, or rather that the exchanging electron in **1**$^-$ and **2**$^-$ is localized during the vibrational lifetime of the carbonyl probe. Was this the case, then some mechanism (not electron transfer) would have to explain such a marked degree of coalescence in 1D spectra. To our knowledge there is no other type of mechanism that could cause such overlap and coalescence of the bandshapes in complexes like **1**$^-$. Furthermore, electrochemical, resonance Raman, temperature dependent IR and UV-Vis-NIR, all point to extensive electronic communication, vibronic bridge mediated and solvent dynamic dependence on electron transfer rates. These investigations all point to preexponentially fast k_{et}'s, which is in contrast to the notion that $k_{et}^{-1} > 10$ ps.

It is also possible that no cross peaks may be observed for **1**$^-$ – **5**$^-$, irregardless of electron transfer, because effective intramolecular communication (via an intramolecular energy redistribution mechanisms[22]) between carbonyl probes is severely limited by the distance and number of bonds that separates them. A vibrationally excited carbonyl in the dimer system will achieve relaxation by energy transfer pathways into the cluster and into the solvent medium in the immediate surroundings. Because through bond separation is ~20 Å and through space separation is ~16 Å, and there are (3N-6) degrees of freedom by which vibrational relaxation can occur, it is unlikely that a significant amount of vibrational energy will be

shared between carbonyls in the dimer systems. This much was certainly verified in the neutral spectra of 1* and 2*.

Despite the great distance between the vibrational probes, could it still be possible that sufficiently fast transfer of electron density between dimer clusters will lead to carbonyl off diagonal peaks? The carbonyl is a "sensor" of electron density on the cluster, and as such should feel the effects of the transferring electron density on th cluster to which it is attached. This alone, however, will not yield cross peaks in the 2D spectrum. An excited CO mode will vibrationally decay into the bath (surrounding solvent) and $Ru_3(OAc)_6$ unit (which is large enough to be a bath in its own right). It is the fact that vibrational energy from one excited carbonyl will never reach the neighboring carbonyl that will not permit the formation of cross peaks. Though an excited carbonyl mode can observe electron density leaving the cluster to which it is attached, it will have no information as to whether the accompanying carbonyl of the other cluster has recognized the newly incoming electron density.

For perspective, consider the same dynamic hole burning 2D IR experiment regarding the exchange reaction of $Fe(CO)_5$. This system displays very strong cross peaks in 2D spectra. Only a single iron atom separates the exchanging carbonyls and all IR active modes are directed through the iron center. It is easy to see that energy transfer between the different active carbonyl modes is highly energetically coupled. The probability that an initially excited (pumped) mode will transfer energy to a final normal mode (probed) has been calculated for $Fe(CO)_5$.[12] For example, $Fe(CO)_5$ has three vibrational modes of consequence, a_2" and e', and an inactive a_1' mode. From the calculation, an excited axial carbonyl a_2" mode will theoretically have 100% probability of energy transfer to equatorial e' mode, and from an initially excited equatorial e' (degenerate) mode 44% probability of energy transfer to e', 55% probability of energy transfer to a_1' mode, and 100% probability of energy transfer to

a_2" mode. With such efficient means of energy transfer between active modes, it is no surprise that cross-peaks are evident in 2D spectra. Considering the substantial difference in the number of bonds separating carbonyl modes in $Fe(CO)_5$ versus $[Ru_3O(OAc)_6(CO)(dmap)$ -pz- $(dmap)(CO)(OAc)_6Ru_3O]$, the probability of substantial energy transfer in the latter is expected to be critically diminished.

Another notable difference between metal-carbonyls and mixed valence dimer-of-trimer systems, is that the active modes of metal carbonyls are *participating* in exchange and not *spectating* an exchange process. Although participation of vibrational modes in a given exchange process is not necessarily a requirement for cross-peak formation, it is a lucid pathway for intramolecular energy transfer. In contrast, although a spectator mode can be used to detect regional differences in structure or oxidation state, there is no guarantee that spectators will "collectively" "realize" that exchange has taken place. Although in the case of dimer-of-trimer

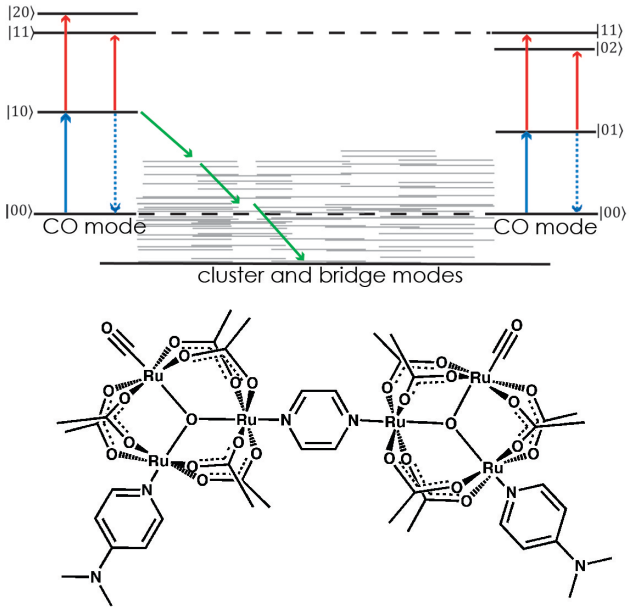

Figure 4.12 A schematic showing cluster and bridge modes in mixed valence dimers like **1**$^-$ – **5**$^-$ acting as a vibrational energy sink to which excited carbonyls may transfer energy.

systems there likely one large nearly delocalized ground electronic state shared over the entire molecule (which acts as a conduit for electron transfer), this does not imply that vibrational energy transfer can travel freely between clusters.

The effect of long-range vibrational energy loss has been studied by a group at Tulane University, where a relaxation-assisted (RA) 2D IR spectroscopy for the enhancement of cross-peak amplitude in weakly coupled modes has been developed.[22,23] RA 2D IR is a two-color heterodyne photon echo method that enhances a weakly coupled mode by tuning the laser frequency of the first and second pulses to the initial mode and tuning the third pulse to the frequency of the final mode. With this technique enhanced cross-peaks have been observed for modes spatially separated by 11 Å and it is believed that coupling between modes exceeding 10 – 15 Å in distance could be observed with RA 2D IR.[22]

4.5 Conclusions

There are very few examples of electron transfer studied by 2D IR in the literature.[24-28] There are no 2D IR studies of a ground state electron transfer reactions in the literature. What may me learned from a 2D IR study of electron transfer dynamics in **1**$^{-}$ – **5**$^{-}$ is of great interest to the vibrational spectroscopic and electron transfer communities. The study here proved to be a quite an undertaking and did not readily providing the desired dynamic information. It would seem also, that studying electron transfer in **1**$^{-}$ – **5**$^{-}$ tested the experimental limitations of this vibrational spectroscopy, and the accompanying computational methods. 2D spectra lacking the conventional metric for exchange, cross-peaks, *may* call into question the ultrafast electron transfer behavior in **1**$^{-}$ – **5**$^{-}$. Specifically it challenges the presently assigned electron transfer lifetime of ~1 ps, and could lead to the assumption that electron transfer rates are at least an order of magnitude slower their currently assigned rate.

Given what is known of the mixed valence character from previous compelling studies, and especially the solvent dynamic response of these systems, it seems quite unlikely that k_{et}^{-1} is slower than 10 - 15 ps. Rather, the metal-carbonyl framework of **1**$^-$ – **5**$^-$ is such that an investigation via a correlation spectroscopic method is severely hindered by the lack of correlation of the probe functional groups. There are currently DFT calculations underway to learn about anharmonicities and probabilities of vibrational energy transfer in **1**$^-$ – **5**$^-$. These calculations may shed light on the complexities of the mixed valence system.

Although there is great appeal in a metal-carbonyl study, there are other viable modes in the mixed valence dimers that may be investigated. For instance, appearing in the 1700 – 1450 cm^{-1} region of the FTIR, are acetate modes and the pyrazine ν_{8a} mode. It is known from the vibronic enhancement of the ν_{8a} band in mixed valence species that this mode is an active player in electron transfer. The ν_{8a} mode results in a formally a forbidden IR transition (possessing A_g symmetry), and in electronically symmetric, neutral and minus two oxidation states, there is little to no IR intensity. In the mixed valence state, where there is electronic asymmetry, the ν_{8a} mode is quite intense making it amenable to study by IR spectroscopy. The spatial and through bond proximity of cluster acetates and the bridging pyrazine may alleviate the issue of vibrational energy redistribution which is likely the mechanism limiting the study of electron transfer by vibrationally excited carbonyls. Another interesting avenue of study would involve a NIR pump – IR probe experiment of mixed valence systems. Pumping a mixed valence dimer at the MBCT band will excite an electron from the ground state to excited bridge state. Subsequent probing of the pyrazine ν_{8a} for relaxation kinetics may provide information about the rate at which the bridge is releasing an electron to a Ru_3O cluster. There is currently no hole-burning data for the dimer $[Ru_3O(OAc)_6(py)(CO)\text{-}pz\text{-}(CO)(py)(OAc)_6Ru_3O]^-$. Should a pump-probe study of

the low frequency diagonal peak of this dimer have intermediate relaxation kinetics with respect to **1**$^-$ and **2**$^-$, the argument that the faster time constant is due to electron transfer would be strengthened. It is interesting that dimers exhibiting a dynamic solvent dependence are those that exhibit the additional faster vibrational relaxation time constant. A study of the solvent dependence of vibrational relaxation could also be very fruitful. Future 2D IR experiments could include a study on electron transfer dynamics in dimer systems as mediated by a participating bridging mode.

4.6 Experimental

Neutral dimers were prepared by following the "cluster as complex, cluster as ligand" scheme reported previously. [1,14,29]

Preparation of the mixed valence monoanions was performed in nitrogen filled glovebox. 1.1 equivalents of cobaltocene solution were titrated into solutions of **5**$^-$, **4**$^-$, **3**$^-$, and **2**$^-$ to produce the mixed valence state. 1.1 equivalents of decamethylcobaltocene solution were titrated into a solution of **1**$^-$ to produce the

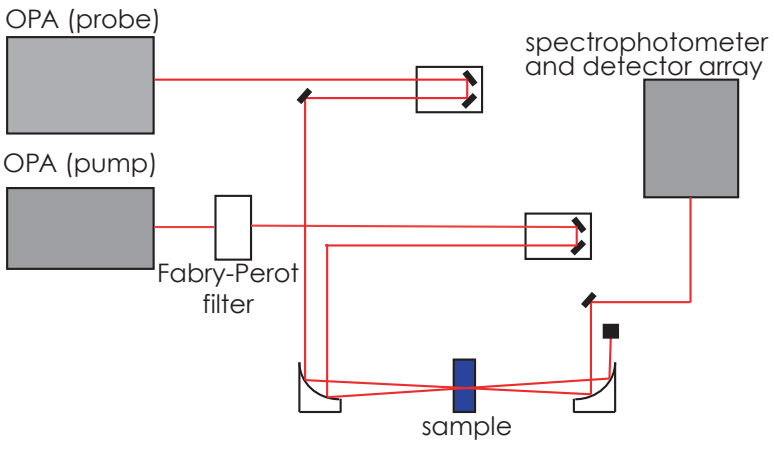

Figure 4.13 The schematic shows a two color hole burning set up. The pump and probe frequencies can be tuned to interrogate modes that are separated by a greater frequency (ca. ~100 cm^{-1}) than is feasible to obtain with a single color set up.

mixed valence state. Solutions of mixed valence dimer were transferred to sealed liquid IR cells (Specac model number 20502) of pathlength 0.5 mm with CaF_2 crystal optic windows. Samples contained in these air-free cells were stable at room temperature for greater than 24 hours. Details of the dynamic hole burning experimental set up have been reported previously.[12] A schematic of the experimental set up is shown in Figure 4.13.

4.7 References

(1) Ito, T.; Hamaguchi, T.; Nagino, H.; Yamaguchi, T.; Washington, J.; Kubiak, C. P. *Science* **1997**, *277*, 660.

(2) Grevels, F. W.; Kerpen, K.; Klotzbucher, W. E.; McClung, R. E. D.; Russell, G.; Viotte, M.; Schaffner, K. *J. Am. Chem. Soc.* **1998**, *120*, 10423.

(3) Turner, J. J.; Gordon, C. M.; Howdle, S. M. *J. Phys. Chem.* **1995**, *99*, 17532.

(4) Turner, J. J. In *Handbook of vibrational spectroscopy*; John Wiley and Sons Ltd. : 2002; Vol. 1, p 101.

(5) Macphail, R. A.; Strauss, H. L. *J. Chem. Phys.* **1985**, *82*, 1156.

(6) Wood, K. A.; Strauss, H. L. *Ber. Bunsen Phys. Chem.* **1989**, *93*, 615.

(7) Wood, K. A.; Strauss, H. L. *J. Phys. Chem.* **1990**, *94*, 5677.

(8) Noda, I. *J. Am. Chem. Soc.* **1989**, *111*, 8116.

(9) Zheng, J.; Kwak, K.; Fayer, M. D. *Acc. Chem. Res.* **2007**, *40*, 75.

(10) Cervetto, V.; Helbing, J.; Bredenbeck, J.; Hamm, P. *J. Chem. Phys.* **2004**, *121*, 5935.

(11) Hochstrasser, R. M.; Ge, N. H.; Gnanakaran, S.; Zanni, M. T. *Bull. Chem. Soc. Jap.* **2002**, *75*, 1103.

(12) Cahoon, J. F.; Sawyer, K. R.; Schlegel, J. P.; Harris, C. B. *Science* **2008**, *319*, 1820.

(13) McClung, R. E. D. In *Program for the simulation of IR spectra of exchanging systems*.

(14) Salsman, J. C.; Ronco, S.; Londergan, C. H.; Kubiak, C. P. *Inorg. Chem.* **2006**, *45*, 547.

(15) Ito, T.; Hamaguchi, T.; Nagino, H.; Yamaguchi, T.; Kido, H.; Zavarine, I. S.; Richmond, T.; Washington, J.; Kubiak, C. P. *J. Am. Chem. Soc.* **1999**, *121*, 4625.

(16) Londergan, C. H.; Kubiak, C. P. *J. Phys. Chem. A* **2003**, *107*, 9301.

(17) Londergan, C. H.; Rocha, R. C.; Brown, M. G.; Shreve, A. P.; Kubiak, C. P. *J. Am. Chem. Soc.* **2003**, *125*, 13912.

(18) Glover, S. D.; Goeltz, J. C.; Lear, B. J.; Kubiak, C. P. *Coord. Chem. Rev.* **2010**, *254*, 331.

(19) Glover, S. D.; Lear, B. J.; Salsman, C.; Londergan, C. H.; Kubiak, C. P. *Phil.Trans. Roy. Soc. A* **2008**, *366*, 177.

(20) Lear, B. J.; Glover, S. D.; Salsman, J. C.; Londergan, C. H.; Kubiak, C. P. *J. Am. Chem. Soc.* **2007**, *129*, 12772.

(21) Baiz, C. R.; Mcrobbie, P. L.; Anna, J. M.; Geva, E.; Kubarych, K. J. *Acc. Chem. Res.* **2009**, *42*, 1395.

(22) Rubtsov, I. V. *Acc. Chem. Res.* **2009**, *42*, 1385.

(23) Kurochkin, D. V.; Naraharisetty, S. R. G.; Rubtsov, I. V. *P. Natl. Acad. Sci.* **2007**, *104*, 14209.

(24) Rubtsov, I. V.; Kang, Y. K.; Redmore, N. P.; Allen, R. M.; Zheng, J. R.; Beratan, D. N.; Therien, M. J. *J. Am. Chem. Soc.* **2004**, *126*, 5022.

(25) Rubtsov, I. V.; Redmore, N. P.; Hochstrasser, R. M.; Therien, M. J. *J. Am. Chem. Soc.* **2004**, *126*, 2684.

(26) Barbour, L. W.; Hegadorn, M.; Asbury, J. B. *J. Am. Chem. Soc.* **2007**, *129*, 15884.

(27) Xiong, W.; Laaser, J. E.; Paoprasert, P.; Franking, R. A.; Hamers, R. J.; Gopalan, P.; Zanni, M. T. *J .Am. Chem. Soc.* **2009**, *131*, 18040.

(28) Cahoon, J. F.; Kling, M. F.; Sawyer, K. R.; Andersen, L. K.; Harris, C. B. *J. Mol. Struct.* **2008**, *890*, 328.

(29) Yamaguchi, T.; Imai, N.; Ito, T.; Kubiak, C. P. *Bull. Chem. Soc. Jap.* **2000**, *73*, 1205.

Note: The experiments reported here were preformed in collaboration with Matthew C. Zoerb of the Charles B. Harris Group at University of California, Berkeley.

Chapter 5

Picosecond exchange or pseudo-collapse? Ultrafast isomerization dynamics in $Ru(S_2C_4F_6)(PPh_3)_2(CO)$

5.1 Introduction

The primary focus of the first four chapters of this thesis has been the ultrafast dynamics of electron transfer, where the exchange is so fast that carbonyl stretches in large dimeric complexes collapse into a single coalesced bandshape.[1] As mentioned briefly in the preceding chapter, other types of ultrafast molecular dynamics can give rise to bandshape coalescence.[2-4] One famous example of this type of behavior has been demonstrated in (η^4-diene)iron$(CO)_3$ systems where carbonyls are presumed to undergo turnstile exchange on the picosecond timescale.[3] This chapter is an investigation of the ultrafast dynamic isomerization of a square pyramidal 1,2-dithiolene-ruthenium complex first discovered by Miller and Balch in 1971.[5] Physical characterization of the complex in the solid state is very straightforward,[5] however, in fluid solution the complex exhibits dynamic behavior that has proven to be a challenge to interpret.

The square pyramidal complex $Ru(S_2C_4F_6)(PPh_3)_2(CO)$, where PPh_3 = triphenylphosphine, can exist in the two stable isomeric forms shown in Figure 5.1. In the solid state both of the isomers have distinct spectroscopic properties by which they may be readily identified. The form of the complex with the carbonyl in the apical position, $Ru(S_2C_4F_6)(PPh_3)_2(CO_{apical})$, gives orange crystals and has a carbonyl stretch at 1944 cm^{-1}.[5] When the carbonyl resides in the equatorial position the complex, $Ru(S_2C_4F_6)(PPh_3)_2(CO_{eq})$, displays a carbonyl stretching frequency at 1973 cm^{-1}.[5] Electronic spectra of solid state isomers in a KBr pellet presents MLCT at 466 nm for the orange isomer and 571 nm for the violet isomer (Figure 5.1b). IR and electronic spectroscopy will be used to understand the isomerization dynamics of this particular square pyramidal system.

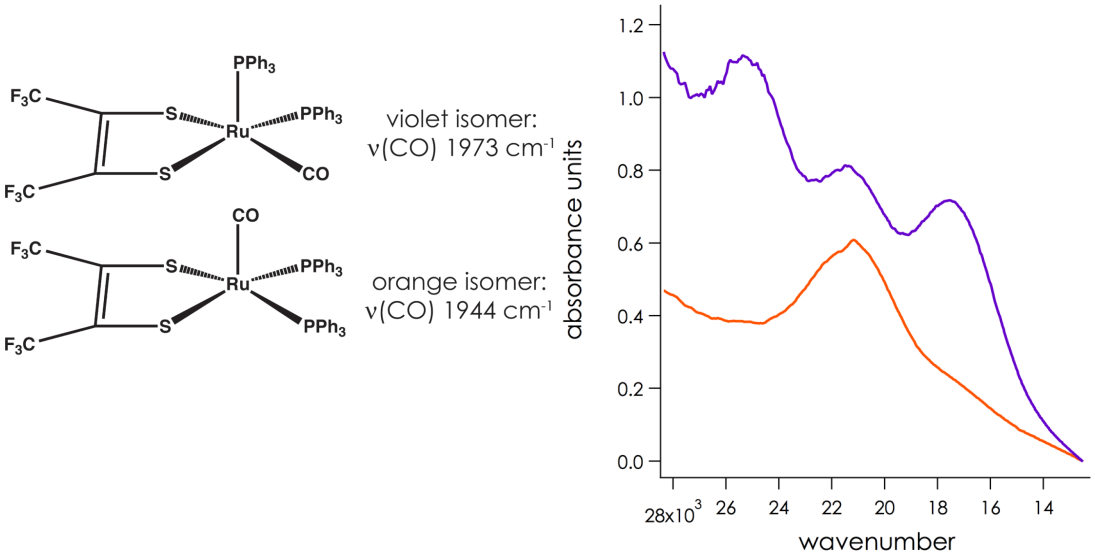

Figure 5.1 a) Two isomeric forms of $Ru(S_2C_4F_6)(PPh_3)_2(CO)$ where PPh_3 = triphenylphosphine. The carbonyl stretching frequencies correspond to solid state IR spectra. **b)** Solid state electronic spectra taken in a KBr pellet. The orange isomer has a single intensity at 21460 cm^{-1} and the violet isomer has two transitions at 25250 cm^{-1} and 17510 cm^{-1}. The third transition (at 21460 cm^{-1}) is due to an impurity of the orange isomer in the sample. Crystallization of violet isomer is typically seeded by growth atop the orange isomer, which makes the violet isomer difficult to isolate.

When either of the pure isomeric forms, orange or violet, of the complex is dissolved in a solvent, it is clear that both isomers are present in solution.[5] Varying the solvent system and the temperature in which the complex is studied demonstrates that the ratio of orange to violet isomer is in an equilibrium that depends on the outer sphere (vide infra). Temperature dependent ^{31}P NMR of the complex in methylene chloride-d_2 revealed the appearance of a single resonance indicating that cluster bound triphenylphospine ligands experience an identical environment.[6] This can only be so if the fluxional behavior of PPh_3 groups faster than NMR can resolve, i.e. the rate of isomerization is faster than10^6 s^{-1}. In all solvents studied (acetonitrile, n-butylnitrile, methylene chloride, 1,2-ethylene dichloride, and 2-methyltetrahydrofuran (2MTHF)) the ν(CO) region of the infrared spectrum shows a broad coalesced peak. The carbonyl bandshapes are reminiscent of the bandshapes observed for mixed valence dimer-of-trimer systems and (η^4-diene)iron$(CO)_3$ systems. This spectroscopic behavior suggests dynamic averaging on the IR (picosecond) timescale enabled by a very low activation barrier to exchange.

5.2 Utrafast exchange and vibrational dephasing: two sources of IR bandshape coalescence

The dimers discussed in Chapters 1 – 4 are examples of a system where the difference in oxidation state of Ru_3O clusters is so fast that attached carbonyls sense an identical environment on the vibrational timescale. The carbonyls are not themselves exchanging, but are acute observers of the electron transfer process. The challenge presented in this chapter is to learn if the coalescence is due to picosecond dynamic isomerization (like a pseudorotation, shown below) or an intrawell torsional mechanism.

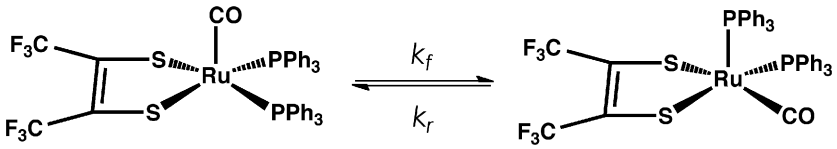

(η^4-diene)iron$(CO)_3$ systems, similar to those shown above, have received considerable attention in the inorganic and physical chemistry communities concerning their dynamic behavior.[3,4,7-12] These systems exhibit vibrationally averaged spectra, upon which the physical mechanism has not yet been unambiguously determined. For example $(CO)_3$(η^4-1,4-cyclooctadiene)iron at room temperature exhibits a sharp ν(CO) band at 2030 cm^{-1} and a broad ν(CO) band at 1960 cm^{-1}.[3] Upon cooling the solution down to 113 K three ν(CO) bands can be resolved. If the carbonyl structure of $(CO)_3$(η^4-1,4-cyclooctadiene)iron is assumed to be static, the three carbonyls have C_s symmetry, meaning there will be two A' bands and one A" band present. If the carbonyls exhibit sufficiently fast fluxional behavior (which depends on the time scale of the spectroscopic method), then the carbonyl experience a C_{3v} environment, giving rise to *A* and *E* IR active modes. The original interpretation of infrared spectra is that the carbonyls are undergoing a dynamic turnstile rotation (interwell) where the carbonyls exchange positions.[3,7,10] The deeply coalesced lineshapes imply very fast rates of exchange with a very low activation barrier of ~1 kcal/mol. Grevels and coworkers applied Bloch lineshape analysis to simulate rate constants on the order of 1 ps.[10]

This interpretation was challenged by Strauss and coworkers who asserted that carbonyl torsional (intrawell) mechanism was the root cause of spectral ν (CO) coalescence and not site exchange.[8,11,12] A heated debate ensued for over a decade as to whether the bandshapes were due to interwell or intrawell dynamics. These two different schemes are shown in Figure 5.2. In the intrawell dynamic

mechanism, bandshape coalescence is achieved by the carbonyls accessing different torsional levels within a particular potential well. Because of anharmonicity the difference in energetic spacing between torsional hot bands (0 → 1, 1 → 2, 2 → 3, etc.) decreases leading to broadening, or dephasing, of the two vibrational transitions. From the intrawell analysis a fully coalesced bandshape can be fit by two Gaussian. Lineshape analysis with the interwell mechanism, on the other hand, predicts the appearance of an exchange band centered at the average frequency of the two exchanging bands. This centered frequency exchange band is also realized in Bloch lineshape analysis in applied to NMR spectra.

To use Bloch equations to simulate exchange for vibrational systems one must account for the angle between the dipole moments of the two exchanging modes.[9,10] This need not be considered in an NMR experiment because the large external magnetic field orients all nuclei regardless of the site they occupy therefore the change in dipole moment is zero.

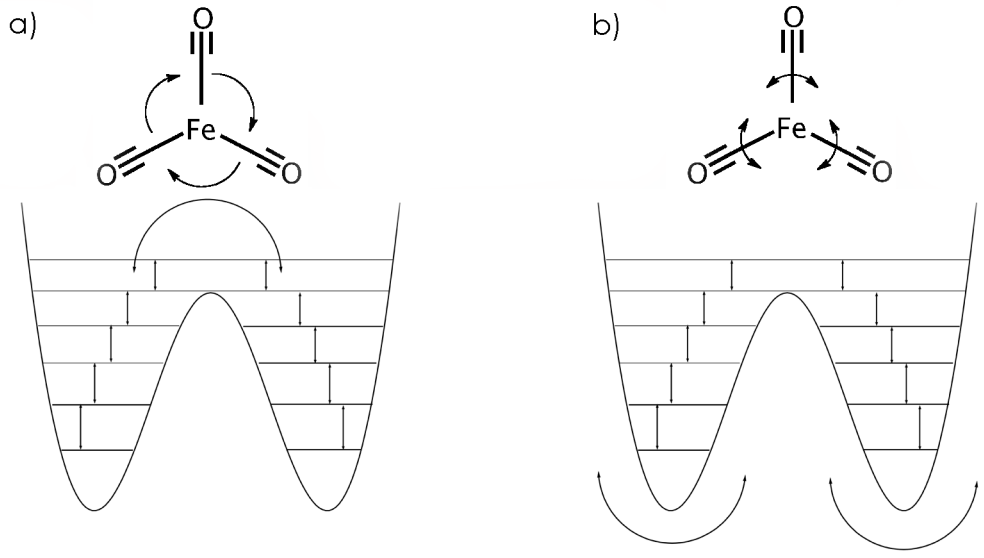

Figure 5.2 a) The interwell mechanism for vibrationally induced site exchange. **b)** intrawell mechanism for site exchage where carbonyls experience dephasing by accessing hot bands between torsional levels.

It should be noted that the energy levels depicted within the potential wells in Figure 5.2 are torsional quantum states,[9,10] not vibrational levels, and there is sufficient energy in the case of (η^4-1,4-cyclooctadiene)iron$(CO)_3$ to have a Boltzmann population the ν = 1 vibrational level, well above the activation barrier. An activation barrier of 1 kcal/mol translates to ~500 cm-1 of energy, which is one third of the energy necessary to induce the vibrational $\nu = 0 \rightarrow 1$ transition for a metal bound carbonyl. It is possible that in cases of a very low activation energy for site exchange that both interwell and intrawell dynamics are occuring simultaneously. This can further cloud the interpretations of bandshape behavior.

Owing to recent fruitful studies of iron pentacarbonyl by dynamic hole burning 2D IR, the Harris group is investigating a number of $(CO)_3$(η^4-diene)iron systems in order to determine if dynamic site exchange is occurring via an interwell mechanism and to learn the associated rate. The work is currently unpublished, however, preliminary results reveal that interwell dynamics are in play.[13] Understanding the mechansim of coalescence in $Ru(S_2C_4F_6)(CO)(PPh_3)_2$ is important, as it provides another system, to the few that are known, that can shed light on the inter/intrawell debate.

5.3 Infrared Spectral coalescence in $Ru(S_2C_4F_6)(CO)(PPh_3)_2$

As previously mentioned, dissolving the pure isomeric form of $Ru(S_2C_4F_6)(PPh_3)_2(CO)$ into a solvent will produce a mixture of isomers, which can be verified by electronic and IR spectroscopy. Figure 5.4 shows the temperature dependent infrared spectra of the carbonyl region of $Ru(S_2C_4F_6)(PPh_3)_2(CO)$ in acetonitrile.

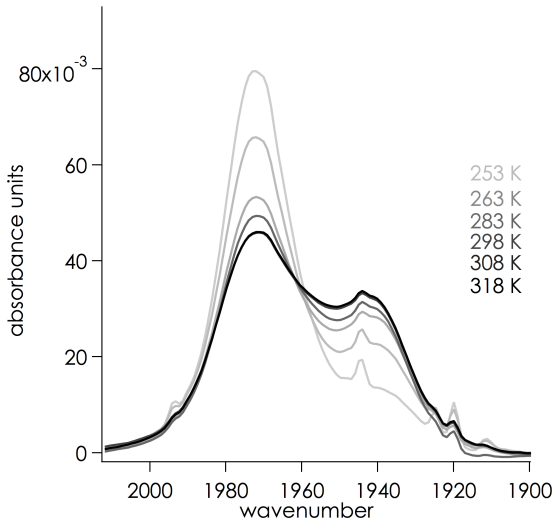

Figure 5.3 Temperature dependent spectra of $Ru(S_2C_4F_6)(CO)(PPh_3)_2$ in acetonitrile. At colder temperatures the violet isomer is favored. The small spike in the low frequency peak is due to a water overtone, which was an artifact from solvent subtraction.

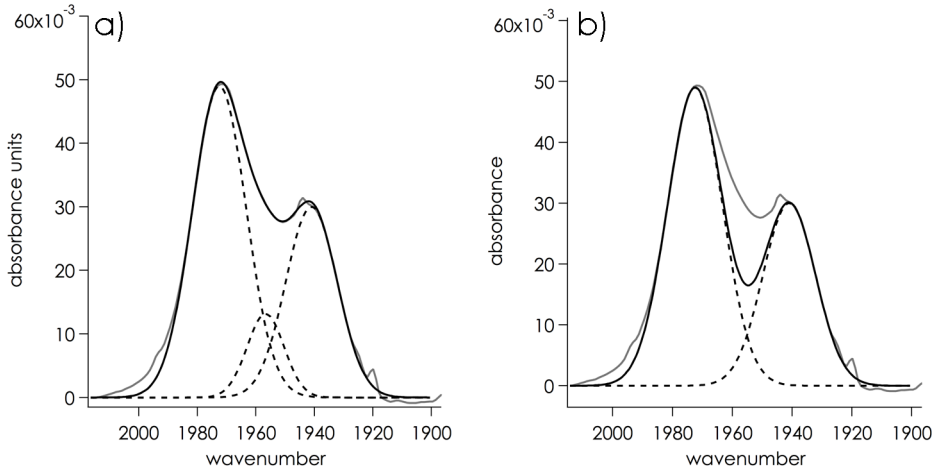

Figure 5.4 a) Gaussian curve fit for ν(CO) banshape (black) with three Gaussian intensities (dotted lines)for the spectrum of $Ru(S_2C_4F_6)(PPh_3)_2(CO)$ (grey) in acetonitrile at 298 K. **b)** Gaussian curve fit for for ν(CO) banshape with two intensities for the spectrum of $Ru(S_2C_4F_6)(PPh_3)_2(CO)$ in acetonitrile at 298 K. It is clear that two Gaussians are insufficient for curve fitting these bandshapes.

At 318 K both isomers are present in solution with the violet isomer being favored. Decreasing the temperature of the solution pushes the equilibrium towards violet isomer, $Ru(S_2C_4F_6)(PPh_3)_2(CO_{eq})$. Upon warming the solution back to 318 K, the

two isomers return to their original populations implying that this isomerization is completely reversible. Figure 5.4 shows the effect of fitting the carbonyl spectrum taken in acetonitrile to three (5.4a) or two (5.4b) Gaussians. The spectrum fit to three Gaussians, clearly the better fit has a small Gaussian in the center that corresponds to the exchange intensity[10] that is predicted by Bloch analysis for a system undergoing very fast exchange. When the spectrum is fit with two Gaussians as in Figure 5.4(b) there is a distinct lack of intensity in the center of the spectrum.

Figure 5.5a shows the IR spectra of $Ru(S_2C_4F_6)(PPh_3)_2(CO)$ in n-butyronitrile which forms a glass upon freezing at 161 K. A striking feature of this set of spectra is that beyond the freezing point of n-butyronitrile vibrational dynamics are apparently still occurring. At temperatures 173, 153 and 113 K the isomer mixture is primarily violet, and curve fitting reveals that the ν(CO) intensity corresponding to the violet isomer continues to grow while the ν(CO) band of the orange isomer diminishes.

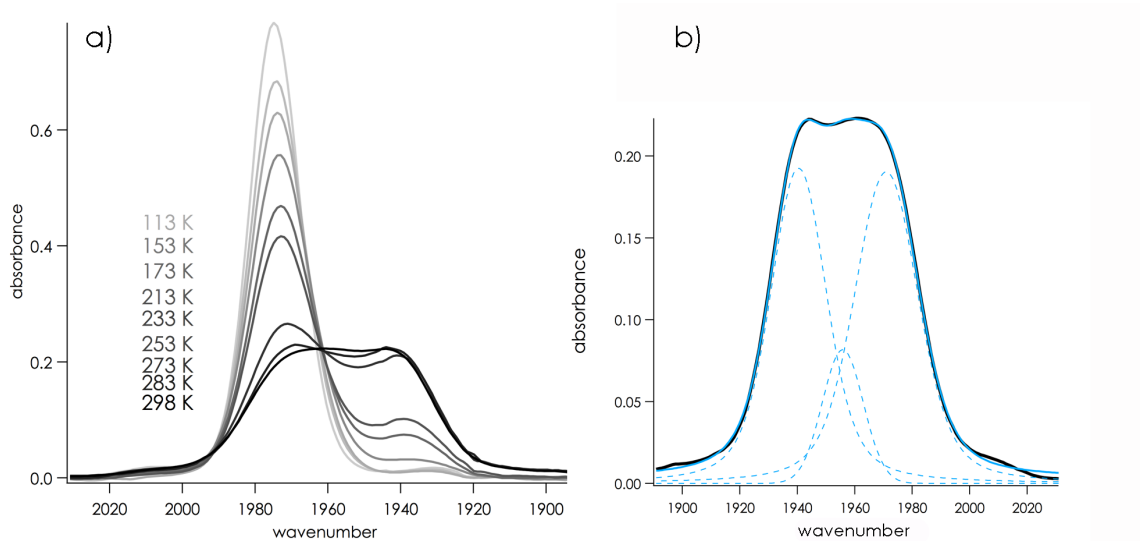

Figure 5.5 a) The temperature dependence of $Ru(S_2C_4F_6)(CO)(PPh_3)_2$ isomerization was followed in n-butyronitrile (freezing point 161 K) through the glass transition. It can be seen that isomerization dynamics are still occurring even after the solvent becomes a frozen glass. **b)** The ν(CO) peak at 298 K cannot be fit to two Gaussian lineshapes, but must include a third peak which corresponds to an exchange intensity.

Figure 5.5b shows a Gaussian curve fit for the ν (CO) region of $Ru(S_2C_4F_6)(PPh_3)_2(CO)$ in n-butyronitrile at 298 K. It is important to note that, once again, only two Gaussian peaks cannot simulate this curve, as fitting with only two Gaussians underestimates the intensity in the center of the band. The third intensity located at 1956 cm^{-1} lies at an average energy of the two primary bands.

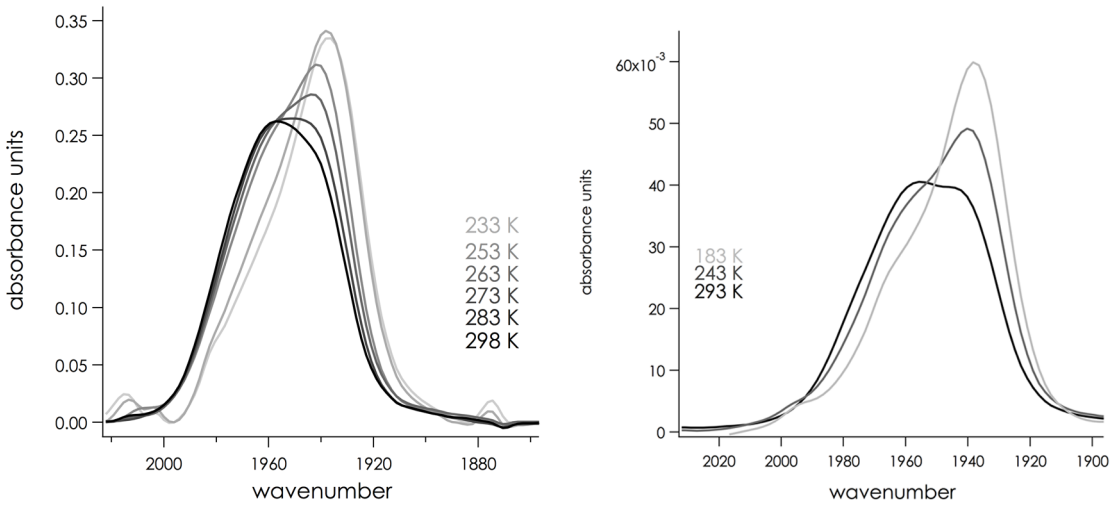

Figure 5.6 a) Temperature dependent IR spectra of $Ru(S_2C_4F_6)(PPh_3)_2(CO)$ dichloromethane (left) and **b)** temperature dependent IR spectra of the carbonyl region for $Ru(S_2C_4F_6)(PPh_3)_2(CO)$ in dichloromethane. In both of these solvents the orange $Ru(S_2C_4F_6)(PPh_3)_2(CO_{apical})$ isomer is favored at lower temperatures.

Figure 5.6 shows temperature dependent spectra of the complex in a) 1,2-dichloroethane and b) dichloromethane. At colder temperatures the orange isomer is favored. This is the opposite behavior that is observed for the complex in acetonitrile and n-butyronitrile. Figure 5.7 shows the ν(CO) spectra for $Ru(S_2C_4F_6)(PPh_3)_2(CO)$ in 2MTHF. The spectra in Figure 5.7 cannot be treated quantitatively due a persistent solvent residual at 1955 cm^{-1}. These spectra are included to demonstrate that in this solvent at decreasing temperatures the orange isomer is favored.

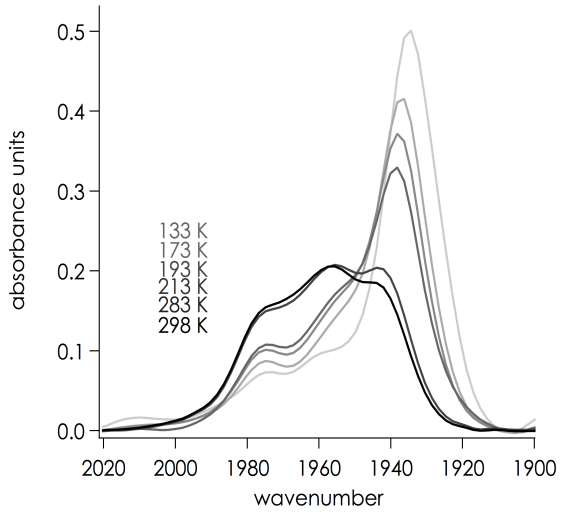

Figure 5.7 a) Temperature dependent IR of the carbonyl region of $Ru(S_2C_4F_6)(CO)(PPh_3)_2$ in 2MTHF. As with methylene chloride and dichloroethane, the orange isomer is favored at lower temperatures. The extra intensity in the center of the band is due to a solvent residual that could not be subtracted.

5.4 Solvent and temperature dependence of electronic spectra

The last section showed that $Ru(S_2C_4F_6)(PPh_3)_2(CO)$ exists in a dynamic equilibrium in solution depending on solvent and temperature that can be detected by IR. This behavior can also be observed by electronic spectroscopy. Figures 5.8a and b show temperature dependent electronic spectra in dichloromethane[14] and 2MTHF, respectively. The trend toward $Ru(S_2C_4F_6)(PPh_3)_2(CO_{apical})$ as temperature is decreased compliments the assignments made by ν(CO) IR analysis. Here, in both solvent systems, the 465 nm band intensifies (i.e. a greater population of $Ru(S_2C_4F_6)(PPh_3)_2(CO_{apical})$ is present) and the 575 band diminishes. These temperature dependent UV-Visible spectra again verify that equilibrium populations are in flux when upon changes in temperature.

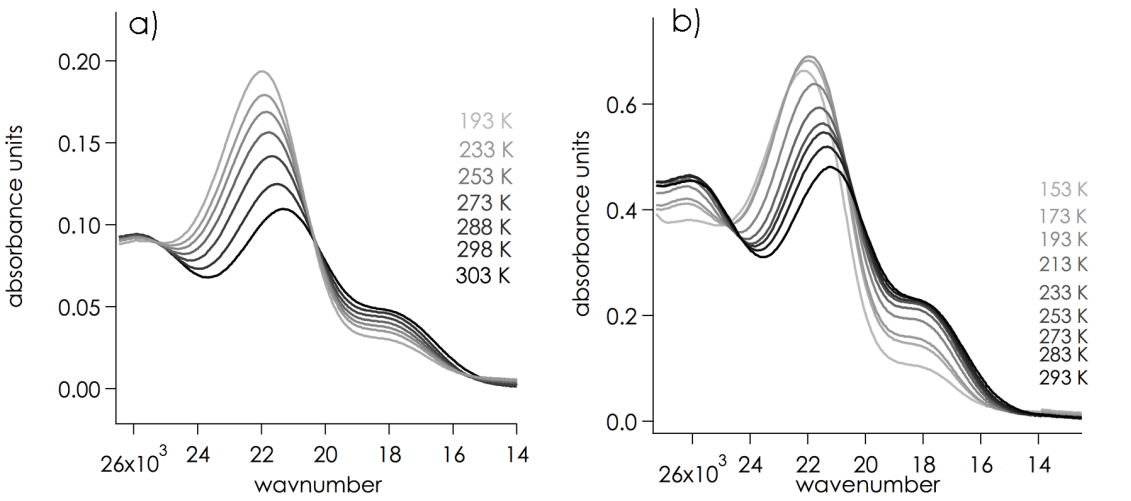

Figure 5.8. Temperature dependent electronic spectra of $Ru(S_2C_4F_6)(CO)(PPh_3)_2$ in **a)** dichloromethane, and **b)** 2MTHF. The band at 465 nm intensifies and the band at 575 diminishes implying the equilibrium favors the orange isomer at colder temperatures.

5.5 2D IR studies on $Ru(S_2C_4F_6)(PPh_3)_2(CO_{apical}) \leftrightarrow Ru(S_2C_4F_6)(PPh_3)_2(CO_{eq})$ isomerization.

Where ruthenium dimers-of-trimers were not suited for 2D IR studies, this system appears to be ideal; the vibrational modes of interest $\nu(CO_{apical})$ and $\nu(CO_{eq})$ are both directed through the metal center, as in $Fe(CO)_5$. This makes pumped vibrational energy more likely to be devoted to exchange and not to intramolecular vibrational relaxation pathways. This system has preliminarily been investigated by heterodyne 2D IR photon echo spectroscopy. These results were inconclusive for several reasons.[15] Firstly, the complex was not stable for the timescale of the experiment (several hours) in acetonitrile, as additional carbonyl bands were detected suggesting the formation of a different complex. Secondly, in methylene chloride, the deeply coalesced nature of the carbonyl bands made resolution of the cross-peak region of the 2D spectrum very difficult. It may be the case that hole burning 2D IR is a more effective probe of the carbonyl dynamics in this system because the excitation frequencies can be selected

to 10 – 15 cm^{-1} FWHM,[16] which can be employed to excite a single mode of interest, whereas the heterodyne experiment will excite all modes within a ~200 cm^{-1} width. The ability to selectively excite a single mode may alleviate the challenge of overlapping diagonal and off diagonal peaks that was observed in the heterodyne technique. It may be very interesting then, to undertake a study of this complex by the hole burning 2D IR technique. The vibrational lifetimes of $\nu(CO_{eq})$ and $\nu(CO_{apical})$ in acetonitrile are 41.8 and 30.5 ps, respectively. This is a reasonably long vibrational window (when compared with the dimer systems of Chapters 4) by which dynamics may be detected. Further 2D IR studies are forthcoming. A complete 2D IR study can confirm the mechanism for coalescence definitively. Although it appears at the current level of analysis employed that coalescence is due to genuine ultrafast exchange, it could be the case that intrawell dynamics are the cause of the observed bandshapes. Either way, the answer is of interest because $Ru(S_2C_4F_6)(PPh_3)_2(CO)$ is one of few chemical systems that can contribute to the exchange – versus – pseudo collapse debate.

5.6 Thermodynamic parameters of isomerization.

Owing to the temperature dependence of isomer populations, thermodynamic parameters can be obtained for the equilibrium reaction. Since the ν (CO) coalescence can provide rate information, the activation energy (E_a) for the isomerization process can be estimated.[3] This analysis has already been done for $Ru(S_2C_4F_6)(PPh_3)_2(CO)$ in methylene chloride and will not be repeated here.[14] To summarize, when $Ru(S_2C_4F_6)(PPh_3)_2(CO)$ was studied in methylene chloride, a plot of $\ln(K_{eq})$ versus 1/T (K^{-1}) gave $\Delta H = -1.2$ kcal mol^{-1} and $\Delta S = -3$ e.u. Plotting k_{isom} (s^{-1}) versus 1/T (K^{-1}) gave $E_a = 1.7$ kcal mol^{-1} and an Arrhenius factor of 2.0×10^{13} s^{-1}. This is consistent with a very low barrier to carbonyl site exchange. Instead, the analysis will

be done for $Ru(S_2C_4F_6)(PPh_3)_2(CO)$ in n-butylnitrile, because when the temperature is lowered the violet (not the orange) isomer is favored.

From the infrared spectra of the carbonyl region in Figure 5.5 a, the populations of orange and violet isomer can be extracted by curve fitting as in Figure 5.5b. The K_{eq} valued determined at each temperature are given along with ν_{max} for each peak in Table 5.3. Plotting $\ln(K_{eq})$ versus 1/T gave a slope off $\Delta H = -2.48 \pm 0.19$ kcal mol^{-1} and an intercept of $\Delta S = -7.8 \pm 1$ e.u and $\Delta G^{298} = 0.13$ kcal mol^{-1}, Figure 5.10.

Table 5.1 Peak maxima for orange and purple isomers as a function of temperature in units of cm^{-1}, the difference in peak maxima are given by $\Delta\nu_{max}$ and the equilibrium constant, K_{eq} which is taken to be the ratio of violet : orange isomers.

Temperature (K)	ν_{max}(orange)	ν_{max}(violet)	$\Delta\nu_{max}$	K_{eq}
298	1942.6	1969.1	26.5	1.06
283	1941.4	1969.2	28.1	1.16
273	1941.1	1970.4	29.3	1.30
253	1941.6	1972.5	31.4	3.03
233	1942.3	1972.7	30.4	4.55
213	1938	1972.9	34.9	12.40
173	1938	1973.4	35.4	43.6
153	1935	1973.9	38.9	47.2
113	1930	1974.5	44.5	174

Table 5.2 Estimated rate constants ($\pm$0.02)for isomerization, k_{isom}, in units of 10^{12} s^{-1} as a function of temperature (in Kelvins) are given.

Temp	298	283	273	253	233	213	173	153	113
k_{isom}	1.25	0.9	0.895	0.56	0.47	0.38	0.276	0.211	0.20

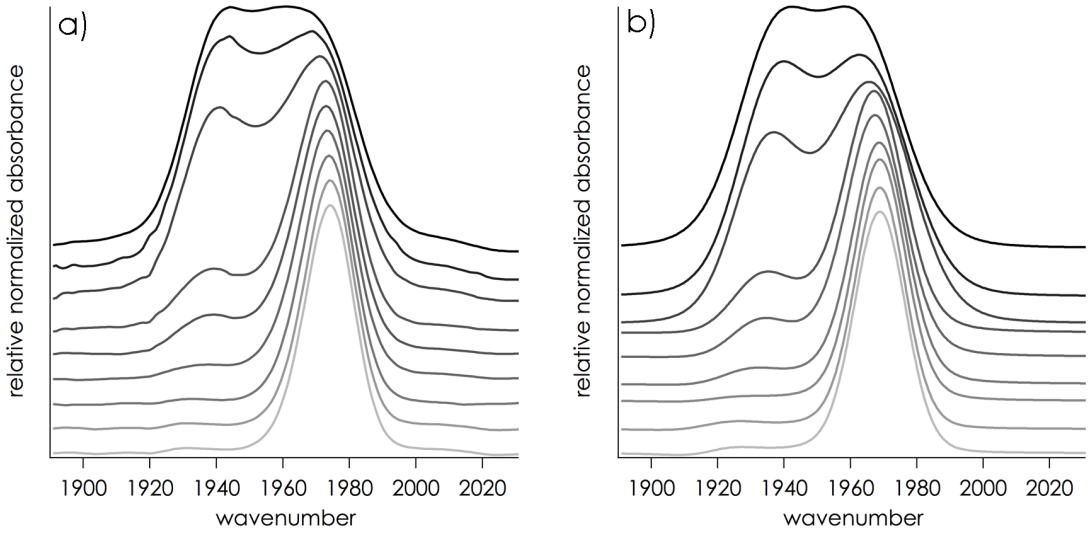

Figure 5.9 a) Normalized ν(CO) bands for $Ru(S_2C_4F_6)(CO)(PPh_3)_2$ in n-butyronitrile as the temperature is cooled from 298 to 113 K. **b)** Simulated ν (CO) bandshapes for $Ru(S_2C_4F_6)(CO)(PPh_3)_2$ in n-butyronitrile. From these simulations the rate constant for isomerization, k_{isom}, was estimated. The k_{isom} rate constants are given in Table 5.2.

Determination of rate constants for the isomerization, k_{isom}, was achieved by fitting the carbonyl region of spectra in *VibexGL*[17] modeling software for exchanging systems. The normalized ν(CO) spectra for the complex are shown in Figure 5.9a. Figure 5.9b shows the simulated spectra from which isomerization rate constants were extracted. It is very satisfying that the spectra in 5.9a and 5.9b are nearly indistinguishable. Table 5.2 summarizes the rate constants at the temperatures probed in the IR. Plotting ln(k_{isom}) versus the inverse temperature gives a slope of E_a = 1.12 kcal mol^{-1} and intercept corresponding to the Arrhenius factor, A = 7.4×10^{12} s^{-1}, Figure 5.10. These data, as expected, are consistent with a very low activation barrier between $Ru(S_2C_4F_6)(PPh_3)_2(CO_{apical}) \leftrightarrow Ru(S_2C_4F_6)(PPh_3)_2(CO_{eq})$.

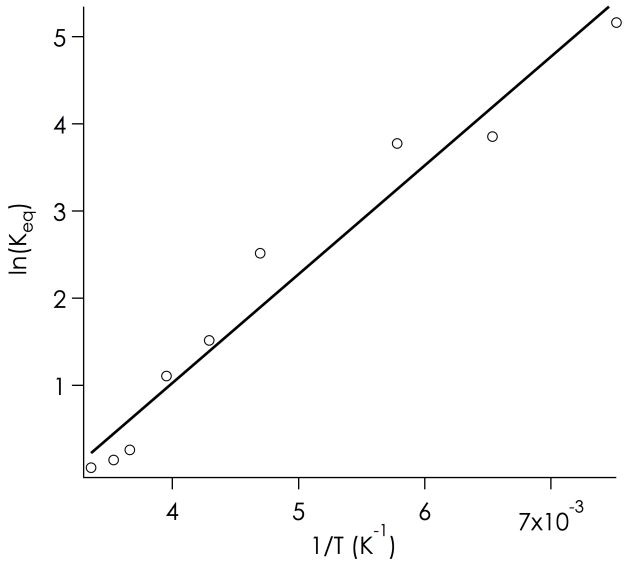

Figure 5.10 A plot of $\ln(K_{eq})$ versus 1/T, gives ΔH = -2.48 ± 0.19 kcal mol^{-1} and an intercept of ΔS = -7.8 ± 1 e.u and ΔG^{298} = 0.13 kcal mol^{-1}.

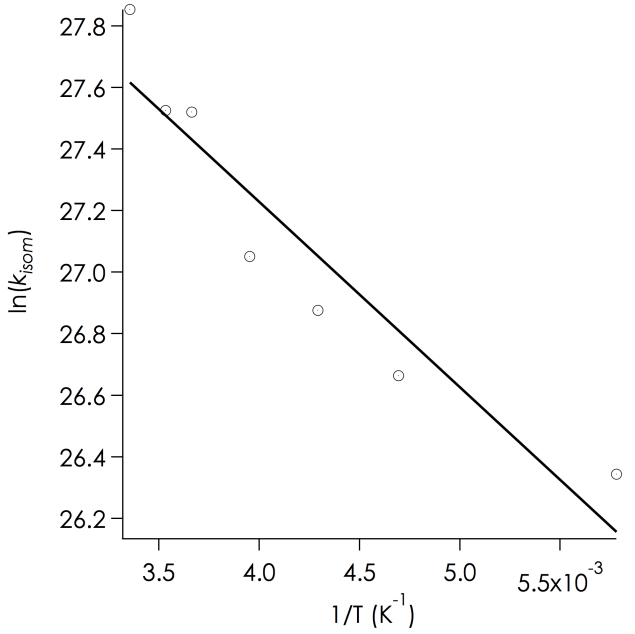

Figure 5.11 A plot of $\ln(k_{isom})$ verses inverse temperature in Kelvins. The slope gives an activation energy of E_a = 1.12 kcal mol^{-1} and an intercept corresponding to an Arrhenius parameter of A = 7.4 ×10^{12} s^{-1}. The temperatures corresponding to when the solvent is frozen have been omitted from the plot as the collisional frequency is expected to be smaller once the solvent is solid. However, were they to be included the fit would predict E_a = 0.84 kcal mol^{-1} and A = 3.6 ×10^{12} s^{-1}.

5.7 Crystallographic determination of $Ru(S_2C_4F_6)(CO)(PPh_3)_2$

Crystallographic characterization of the two isomers was preformed in 1973 and 1977.[18,19] To ensure isomeric purity of products and achieve greater structural refinement, crystallographic determination was repeated at the UCSD crystallography facility. There were some interesting differences between the previously reported crystal structures and those collected more recently that are worth mentioning.

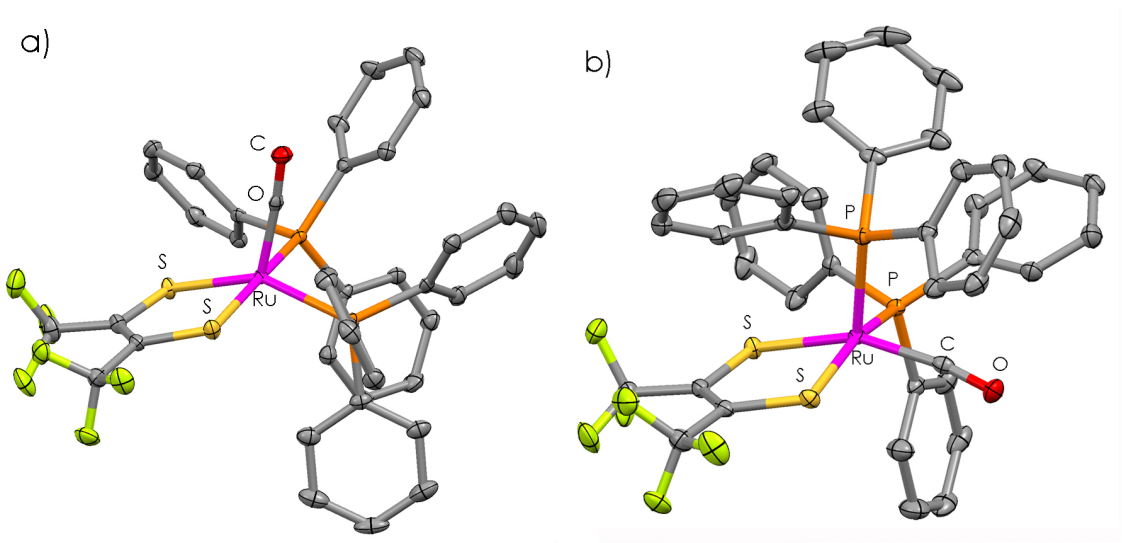

Figure 5.12 Crystallographic structures of the **a)** orange with the carbonyl in the apical position and **b)** violet isomers with the carbonyl in the equatorial position. These complexes exhibit a distorted square pyramidal geometry.

Table 5.3 Selected crystallographic unit cell parameters for recently obtained (2008) crystal structures and crystal structures collected over 30 years ago.

	orange (1973)[18]	orange (UCSD)	violet (1977)[19]	violet (UCSD)
r-factor	0.047	0.035	0.055	0.0227
space group	$P_{21/c}$	$P_{21/n}$	P_{bca}	$C_{2/c}$
Z	4	4	8	8
Z'	1	1	1	1

Table 5.3 Selected crystallographic unit cell parameters for recently obtained (2008) crystal structures and crystal structures collected over 30 years ago, continued.

Temp (K)	295	100	295	100
a	10.147	10.088	22.394	38.777
b	10.081	10.014	19.107	10.0596
c	38.627	37.515	17.48	21.6413
α	90	90	90	90
β	102.27	93.296	90	118.678
γ	90	90	90	90
volume($Å^3$)	3860.971	3784	7479.38	7406.4

Table 5.4 Selected crystallographic bond lengths for orange and violet isomers. These values have been obtained from the crystal structures solved at UCSD crystallography facility.

Bond type	distances (orange isomer)/Å	distances (violet isomer)/ Å
Ru–C	1.822	1.873
Ru–S	2.294	2.312
Ru–S	2.332	2.295
Ru–P	2.363 (equatorial)	2.369(equatorial)
Ru–P	2.378 (equatorial)	2.291 (axial)
C–O	1.162	1.149

The selected core bond distances from recently collected structural analysis are not greatly different from those collected for the orange and violet isomers by other research groups. A general difference is that in the more recently solved structures many of the bond lengths are shorter presumably due to the collection of

reflective data at a temperature 195 K colder. The newer data for the violet isomer refined to different space groups, $C_{2/c}$ (versus P_{cba} from the 1977 structure). P_{cba} possesses higher symmetry than $C_{2/c}$, and it may be that cooling of solid crystals in the violet isomer caused a contraction such that there was loss of symmetry.

From Table 5.1 it can be seen that there is a small difference in Ru–C distance between $Ru(S_2C_4F_6)(PPh_3)_2(CO_{apical})$ and $Ru(S_2C_4F_6)(PPh_3)_2(CO_{eq})$ that is worth mention. When the carbonyl is in the axial position of the square pyramid the Ru–C bond distance is 1.822 A, while in the violet isomer the Ru–C distance is 1.873. A shorter distance between the carbon and metal center can facilitate greater Ru–dπ to CO–π^* backbonding. Comparison of the C–O distances for the two different isomeric forms shows that the orange isomer has a C–O bond distance of 1.162 A while the violet isomer has a shorter bond distance of 1.149 A. The longer C–O bond distance in the orange isomer is consistent with greater π backbonding from ruthenium and justifies the lower frequency of ν(CO) stretch in the infrared spectrum.

5.8 DFT studies of vibrational and electronic properties

In order to ascertain the details of the pseudo rotation mechanism, different transition states that are reasonably accessible at temperatures of 298-113 K will need to be realized. DFT can be of assistance in this area, by calculation of energies and frequencies of possible transition states, wherein a lucid vibrationally induced mechanism can emerge.[20,21] Owing to the predicted low barrier of activation, it is probable that the vibrational modes of the molecule are sufficient to induce isomerization. A vibrational DFT study would aid in mechanistic determination by allowing for the calculation of structural intermediates that otherwise cannot be detected by vibrational spectroscopy. With a firm understanding of realistic

vibrational modes, single point calculations can then be carried out on reasonable structural intermediates.

Using the coordinates obtained from crystallography, geometry optimizations and frequency calculations have been undertaken. Frequency calculations take some time, and this aspect of our inquiry has not at this time been fully realized. From the geometry optimized structures for $Ru(S_2C_4F_6)(PPh_3)_2(CO_{apical})$ and $Ru(S_2C_4F_6)$-$(PPh_3)_2(CO_{eq})$ HOMO and LUMO energies as well as probable molecular orbitals for each isomer were calculated. DFT of $Ru(S_2C_4F_6)$ $(PPh_3)_2(CO_{apical})$determined the energy of the HOMO is -118 kcal mol^{-1} with a total bonding energy of -12203.48 kcal mol^{-1}. In comparison, the HOMO of $Ru(S_2C_4F_6)(PPh_3)_2(CO_{eq})$ was calculated to be -113 kcal mol^{-1} with a total bonding energy of -12202.91 kcal mol^{-1}. The difference in total bonding energy between the two isomers, ~0.5 kcal mol^{-1} (or ~ 175 cm^{-1}), speaks to the viability of isomerization at room temperature.

It is curious even though the violet isomer is not energetically favored, it is apparently the more stable isomer at colder temperatures in acetonitrile and n-butylnitrile. It may be that there is a favorable interaction between coordinating solvents and the free coordination site on the ruthenium metal center. Were a solvent to interact with the metal, steric interactions of the PPh_3 groups would favor having the carbonyl in the equatorial position. The non-coordinating solvents 2MTHF, CH_2Cl_2, and CH_2ClCH_2Cl, are not likely to interact with the empty site on the metal center, therefore the more energetically stable isomer (orange) should persist at colder temperatures.

Forthcoming work with DFT will include implementation of single point calculations on isomer intermediates to identify reasonable transition state structures that can be realized by inner sphere vibrational modes.

5.9 Conclusions.

Despite intensive study of $Ru(S_2C_4F_6)(PPh_3)_2(CO)$ dynamics, there is still no definitive answer as to the timescale of isomerization. The temperature dependent study in two different solvent systems yielded very low activation energies from estimated rate constants. It is unfortunate that the 2D IR studies to date were inconclusive due mainly to the inability to resolve any crosspeaks (if there were any) from the broad diagonal features. The temperature dependent analysis of $Ru(S_2C_4F_6)(PPh_3)_2(CO)$ in n-butyronitrile by IR spectroscopy not only displayed population of isomers in dynamic equilibrium, but also a de-coalescence of ν(CO) band. Specifically, the $\Delta\nu_{max}$ for the ν(CO) bands increased by ~20 cm^{-1} as the temperature of the solution was cooled from 298 K to 113 K. De-coalescence in (η^4-cyclooctadiene)iron$(CO)_3$ was observed at colder temperatures and was attributed to a decrease in isomerization rate. The averaged ν (CO) bandshape and thermodynamic data presented in this chapter are convincing evidence that in CH_2Cl_2 and n-butylnitrile an ultrafast interwell mechanism is occuring. However, the possibility of an intrawell mechanism, or a combination of both mechanisms cannot be entirely ruled out. A further dynamic hole burning 2D IR study coupled with DFT is likely to resolve this issue.

5.10 Experimental details.

Cryostatic UV-vis spectra were collected with a Shimadzu 3600. Samples were contained in Specac sealed liquid IR cells with CaF_2 crystal optic windows with a pathlength of 0.50 or 1.00 mm. Solvent UV-vis spectra were collected in the same sealed liquid IR cell and were used as background subtractions for the sample spectra. Cryostatic IR was carried out in similar fashion as above in a Bruker Equinox FTIR. Spectral curve fitting to obtain population ratios of $Ru(S_2C_4F_6)(PPh_3)_2(CO_{eq})$ and

$Ru(S_2C_4F_6)(PPh_3)_2(CO_{apical})$ was carried out in IGORpro 6.12. The best fits were obtained by fitting ν(CO) bandshapes to three Gaussians. Estimated rate constants were obtained by employing Bloch lineshape analysis with VibexGL.

Synthesis of the compounds has been reported previously. Orange crystals were grown from 50:50::methylene chloride:hexanes solution over the course of five days. A mixture of orange and violet crystals can be obtained from recrystallization from 50:50::chloroform:hexanes solution. Growing crystals at 283 K favored formation of violet crystals. Most often, this method of crystallization produced violet plates, which protruded from orange blocks. Successful isomeric purification required manually separating the isomers under a microscope.

DFT calculations were carried out in Amsterdam Density Functional (ADF) program suite,[23,24] version 2007.[25] The triple-zeta Slater-type orbital (TZ2P, ADF basis set) employed for all atoms and assumed a frozen core for the innermost atomic shells. The density functionals were defined as follows. Exchange correlation potentials were realized by local density approximation (LDA) with the VWN[26] correction for the parameterization for an electron gas. Employed also, was the generalized gradient approximation (GGA) as described by Becke[27] and Perdew.[28-30] To account for relativistic effects the (ZORA) zero-order regular approximation routine[31,32] was included in the calculation. MO visualizations and their energies were obtained from the ADF graphical user interface.

Details of the crystallographic determination are as follows. For $Ru(S_2C_4F_6)(PPh_3)_2(CO_{eq})$, a purple plate 0.18 x 0.14 x 0.09 mm in size was mounted on a Cryoloop with Paratone oil. Data were collected in a nitrogen gas stream at 100(2) K using and scans. Crystal-to-detector distance was 60 mm and exposure time was 20 seconds per frame using a scan width of 1.0°. Data collection was 98.0% complete to 66.59° in q. A total of 23043 reflections were collected covering the indices, -45<=*h*<=46, -8<=*k*<=11, -

24<=*l*<=25. 6405 reflections were found to be symmetry independent, with an R_{int} of 0.0307. Indexing and unit cell refinement indicated a c-centered, monoclinic lattice. The space group was found to be $C_{2/c}$ (No. 15).

For $Ru(S_2C_4F_6)(PPh_3)_2(CO_{apical})$ an orange block 0.20 x 0.10 x 0.10 mm in size was mounted on a Cryoloop with Paratone oil. Data were collected in a nitrogen gas stream at 100(2) K using and scans. Crystal-to-detector distance was 60 mm and exposure time was 10 seconds per frame using a scan width of 0.3°. Data collection was 99.6% complete to 25.00° in q. A total of 67205 reflections were collected covering the indices, -12<=*h*<=12, -12<=*k*<=12, -45<=*l*<=45. 6930 reflections were found to be symmetry independent, with an R_{int} of 0.0881. Indexing and unit cell refinement indicated a primitive, monoclinic lattice. The space group was found to be $P_{2(1)/n}$ (No. 14).

The data for both $Ru(S_2C_4F_6)(PPh_3)_2(CO_{eq})$ and $Ru(S_2C_4F_6)(PPh_3)_2(CO_{apical})$ were integrated using the Bruker SAINT software program and scaled using the SADABS software program. Solution by direct methods (SHELXS-97)[22] produced a complete heavy-atom phasing model consistent with the proposed structure. All non-hydrogen atoms were refined anisotropically by full-matrix least-squares (SHELXL-97). All hydrogen atoms were placed using a riding model. Their positions were constrained relative to their parent atom using the appropriate HFIX command in SHELXL-97.

Table 5.5 Crystal data and structure refinement for $Ru(S_2C_4F_6)(PPh_3)_2(CO_{apical})$.

Empirical formula	$C_{41}H_{30}F_6OP_2RuS_2$
Formula weight	879.78
Temperature	100(2) K
Wavelength	0.71073 Å
Crystal system	Monoclinic

Table 5.5 Crystal data and structure refinement for $Ru(S_2C_4F_6)(PPh_3)_2(CO_{apical})$, continued.

Space group	$P2_{(1)/n}$	
Unit cell dimensions	a = 10.088(3) Å	α= 90°.
	b = 10.014(3) Å	β= 93.296(4)°.
	c = 37.515(12) Å	γ = 90°.
Volume	3784(2) $Å^3$	
Z	4	
Density (calculated)	1.544 Mg/m^3	
Absorption coefficient	0.672 mm^{-1}	
F(000)	1776	
Crystal size	0.20 x 0.10 x 0.10 mm^3	
Crystal color/habit	orange block	
Theta range for data collection	1.09 to 25.42°.	
Index ranges	-12<=h<=12, -12<=k<=12, -45<=l<=45	
Reflections collected	67205	
Independent reflections	6930 [R(int) = 0.0881]	
Completeness to theta = 25.00°	99.6 %	
Absorption correction Semi-empirical from equivalents Max. and min. transmission	0.9358 and 0.8773	
Refinement method	Full-matrix least-squares on F2	
Data / restraints / parameters	6930 / 0 / 478	
Goodness-of-fit on F2	1.075	
Final R indices [I>2sigma(I)]	R1 = 0.0350, wR2 = 0.0892	
R indices (all data)	R1 = 0.0368, wR2 = 0.0905	

Table 5.5 Crystal data and structure refinement for $Ru(S_2C_4F_6)(PPh_3)_2(CO_{apical})$, continued.

Largest diff. peak and hole	0.587 and -0.561 e.Å^{-3}

Table 5.6 Bond lengths [Å] and angles [°] for $Ru(S_2C_4F_6)(PPh_3)_2(CO_{apical})$.

C(1)-C(2)	1.353(4)
C(1)-C(3)	1.513(4)
C(1)-S(1)	1.740(3)
C(2)-C(4)	1.516(4)
C(2)-S(2)	1.732(3)
C(3)-F(3)	1.336(3)
C(3)-F(2)	1.340(3)
C(3)-F(1)	1.350(3)
C(4)-F(6)	1.331(3)
C(4)-F(5)	1.347(3)
C(4)-F(4)	1.352(3)
C(5)-O(1)	1.161(3)
C(5)-Ru(1)	1.822(3)
C(6)-C(11)	1.398(4)
C(6)-C(7)	1.403(3)
C(6)-P(4)	1.829(3)
C(7)-C(8)	1.384(4)
C(7)-H(7)	0.9500
C(8)-C(9)	1.385(4)

Table 5.6 Bond lengths [Å] and angles [°] for $Ru(S_2C_4F_6)(PPh_3)_2(CO_{apical})$, continued.

C(8)-H(8)	0.9500
C(9)-C(10)	1.396(4)
C(9)-H(9)	0.9500
C(10)-C(11)	1.394(4)
C(10)-H(10)	0.9500
C(11)-H(11)	0.9500
C(12)-C(17)	1.390(4)
C(12)-C(13)	1.406(4)
C(12)-P(4)	1.839(3)
C(13)-C(14)	1.390(4)
C(13)-H(13)	0.9500
C(14)-C(15)	1.381(4)
C(14)-H(14)	0.9500
C(15)-C(16)	1.389(4)
C(15)-H(15)	0.9500
C(16)-C(17)	1.400(4)
C(16)-H(16)	0.9500
C(17)-H(17)	0.9500
C(18)-C(19)	1.393(3)
C(18)-C(23)	1.399(4)
C(18)-P(4)	1.827(2)
C(19)-C(20)	1.392(4)
C(19)-H(19)	0.9500
C(20)-C(21)	1.387(4)
C(20)-H(20)	0.9500

Table 5.6 Bond lengths [Å] and angles [°] for $Ru(S_2C_4F_6)(PPh_3)_2(CO_{apical})$, continued.

C(21)-C(22)	1.388(4)
C(21)-H(21)	0.9500
C(22)-C(23)	1.388(4)
C(22)-H(22)	0.9500
C(23)-H(23)	0.9500
C(24)-C(29)	1.400(4)
C(24)-C(25)	1.402(4)
C(24)-P(5)	1.837(3)
C(25)-C(26)	1.393(4)
C(25)-H(25)	0.9500
C(26)-C(27)	1.384(5)
C(26)-H(26)	0.9500
C(27)-C(28)	1.377(5)
C(27)-H(27)	0.9500
C(28)-C(29)	1.395(4)
C(28)-H(28)	0.9500
C(29)-H(29)	0.9500
C(30)-C(35)	1.396(4)
C(30)-C(31)	1.402(4)
C(30)-P(5)	1.841(3)
C(31)-C(32)	1.391(4)
C(31)-H(31)	0.9500
C(32)-C(33)	1.377(5)
C(32)-H(32)	0.9500
C(33)-C(34)	1.384(5)

Table 5.6 Bond lengths [Å] and angles [°] for $Ru(S_2C_4F_6)(PPh_3)_2(CO_{apical})$, continued.

C(33)-H(33)	0.9500
C(34)-C(35)	1.389(4)
C(34)-H(34)	0.9500
C(35)-H(35)	0.9500
C(36)-C(41)	1.395(4)
C(36)-C(37)	1.399(4)
C(36)-P(5)	1.839(3)
C(37)-C(38)	1.394(4)
C(37)-H(37)	0.9500
C(38)-C(39)	1.387(4)
C(38)-H(38)	0.9500
C(39)-C(40)	1.386(4)
C(39)-H(39)	0.9500
C(40)-C(41)	1.395(4)
C(40)-H(40)	0.9500
C(41)-H(41)	0.9500
P(4)-Ru(1)	2.3776(8)
P(5)-Ru(1)	2.3626(8)
S(1)-Ru(1)	2.2943(8)
S(2)-Ru(1)	2.3316(8)
C(2)-C(1)-C(3)	124.5(2)
C(2)-C(1)-S(1)	120.48(19)
C(3)-C(1)-S(1)	114.97(19)
C(1)-C(2)-C(4)	124.1(2)
C(1)-C(2)-S(2) 1	21.08(19)

Table 5.6 Bond lengths [Å] and angles [°] for $Ru(S_2C_4F_6)(PPh_3)_2(CO_{apical})$, continued.

C(4)-C(2)-S(2)	114.76(19)
F(3)-C(3)-F(2)	105.8(2)
F(3)-C(3)-F(1)	106.2(2)
F(2)-C(3)-F(1)	106.4(2)
F(3)-C(3)-C(1)	112.2(2)
F(2)-C(3)-C(1)	113.6(2)
F(1)-C(3)-C(1)	112.0(2)
F(6)-C(4)-F(5)	106.3(2)
F(6)-C(4)-F(4)	106.1(2)
F(5)-C(4)-F(4)	106.5(2)
F(6)-C(4)-C(2)	112.6(2)
F(5)-C(4)-C(2)	112.1(2)
F(4)-C(4)-C(2)	112.7(2)
O(1)-C(5)-Ru(1)	175.3(2)
C(11)-C(6)-C(7)	119.1(2)
C(11)-C(6)-P(4)	121.79(19)
C(7)-C(6)-P(4)	118.80(19)
C(8)-C(7)-C(6)	120.5(2)
C(8)-C(7)-H(7)	119.8
C(6)-C(7)-H(7)	119.8
C(7)-C(8)-C(9)	120.1(3)
C(7)-C(8)-H(8)	119.9
C(9)-C(8)-H(8)	119.9
C(8)-C(9)-C(10)	120.2(2)

Table 5.6 Bond lengths [Å] and angles [°] for $Ru(S_2C_4F_6)(PPh_3)_2(CO_{apical})$, continued.

C(8)-C(9)-H(9)	119.9
C(10)-C(9)-H(9)	119.9
C(11)-C(10)-C(9)	119.9(3)
C(11)-C(10)-H(10)	120.1
C(9)-C(10)-H(10)	120.1
C(10)-C(11)-C(6)	120.2(2)
C(10)-C(11)-H(11)	119.9
C(6)-C(11)-H(11)	119.9
C(17)-C(12)-C(13)	118.5(2)
C(17)-C(12)-P(4)	121.30(19)
C(13)-C(12)-P(4)	120.2(2)
C(14)-C(13)-C(12)	120.8(3)
C(14)-C(13)-H(13)	119.6
C(12)-C(13)-H(13)	119.6
C(15)-C(14)-C(13)	119.9(3)
C(15)-C(14)-H(14)	120.0
C(13)-C(14)-H(14)	120.0
C(14)-C(15)-C(16)	120.3(3)
C(14)-C(15)-H(15)	119.9
C(16)-C(15)-H(15)	119.9
C(15)-C(16)-C(17)	119.8(3)
C(15)-C(16)-H(16)	120.1
C(17)-C(16)-H(16)	120.1
C(12)-C(17)-C(16)	120.7(2)
C(12)-C(17)-H(17)	119.7

Table 5.6 Bond lengths [Å] and angles [°] for $Ru(S_2C_4F_6)(PPh_3)_2(CO_{apical})$, continued.

C(16)-C(17)-H(17)	119.7
C(19)-C(18)-C(23)	119.5(2)
C(19)-C(18)-P(4)	122.63(19)
C(23)-C(18)-P(4)	117.83(18)
C(20)-C(19)-C(18)	119.9(2)
C(20)-C(19)-H(19)	120.0
C(18)-C(19)-H(19)	120.0
C(21)-C(20)-C(19)	120.2(2)
C(21)-C(20)-H(20)	119.9
C(19)-C(20)-H(20)	119.9
C(20)-C(21)-C(22)	120.3(2)
C(20)-C(21)-H(21)	119.8
C(22)-C(21)-H(21)	119.8
C(23)-C(22)-C(21)	119.7(3)
C(23)-C(22)-H(22)	120.1
C(21)-C(22)-H(22)	120.1
C(22)-C(23)-C(18)	120.3(2)
C(22)-C(23)-H(23)	119.8
C(18)-C(23)-H(23)	119.8
C(29)-C(24)-C(25)	118.9(2)
C(29)-C(24)-P(5)	120.7(2)
C(25)-C(24)-P(5)	120.3(2)
C(26)-C(25)-C(24)	120.1(3)
C(26)-C(25)-H(25)	120.0
C(24)-C(25)-H(25)	120.0

Table 5.6 Bond lengths [Å] and angles [°] for $Ru(S_2C_4F_6)(PPh_3)_2(CO_{apical})$, continued.

C(27)-C(26)-C(25)	120.3(3)
C(27)-C(26)-H(26)	119.8
C(25)-C(26)-H(26)	119.8
C(28)-C(27)-C(26)	120.2(3)
C(28)-C(27)-H(27)	119.9
C(26)-C(27)-H(27)	119.9
C(27)-C(28)-C(29)	120.2(3)
C(27)-C(28)-H(28)	119.9
C(29)-C(28)-H(28)	119.9
C(28)-C(29)-C(24)	120.3(3)
C(28)-C(29)-H(29)	119.9
C(24)-C(29)-H(29)	119.9
C(35)-C(30)-C(31)	118.3(2)
C(35)-C(30)-P(5)	119.4(2)
C(31)-C(30)-P(5)	122.2(2)
C(32)-C(31)-C(30)	120.3(3)
C(32)-C(31)-H(31)	119.9
C(30)-C(31)-H(31)	119.9
C(33)-C(32)-C(31)	120.7(3)
C(33)-C(32)-H(32)	119.7
C(31)-C(32)-H(32)	119.7
C(32)-C(33)-C(34)	119.7(3)
C(32)-C(33)-H(33)	120.1
C(34)-C(33)-H(33)	120.1
C(33)-C(34)-C(35)	120.2(3)

Table 5.6 Bond lengths [Å] and angles [°] for $Ru(S_2C_4F_6)(PPh_3)_2(CO_{apical})$, continued.

C(33)-C(34)-H(34)	119.9
C(35)-C(34)-H(34)	119.9
C(34)-C(35)-C(30)	120.9(3)
C(34)-C(35)-H(35)	119.6
C(30)-C(35)-H(35)	119.6
C(41)-C(36)-C(37)	118.4(2)
C(41)-C(36)-P(5)	120.23(19)
C(37)-C(36)-P(5)	121.30(19)
C(38)-C(37)-C(36)	120.4(2)
C(38)-C(37)-H(37)	119.8
C(36)-C(37)-H(37)	119.8
C(39)-C(38)-C(37)	120.4(2)
C(39)-C(38)-H(38)	119.8
C(37)-C(38)-H(38)	119.8
C(40)-C(39)-C(38)	119.8(2)
C(40)-C(39)-H(39)	120.1
C(38)-C(39)-H(39)	120.1
C(39)-C(40)-C(41)	119.9(3)
C(39)-C(40)-H(40)	120.1
C(41)-C(40)-H(40)	120.1
C(36)-C(41)-C(40)	121.0(2)
C(36)-C(41)-H(41)	119.5
C(40)-C(41)-H(41)	119.5
C(18)-P(4)-C(6)	102.98(11)
C(18)-P(4)-C(12)	104.32(11)

Table 5.6 Bond lengths [Å] and angles [°] for $Ru(S_2C_4F_6)(PPh_3)_2(CO_{apical})$, continued.

C(6)-P(4)-C(12)	99.11(11)
C(18)-P(4)-Ru(1)	112.83(8)
C(6)-P(4)-Ru(1)	113.93(8)
C(12)-P(4)-Ru(1)	121.34(8)
C(24)-P(5)-C(36)	102.01(12)
C(24)-P(5)-C(30)	104.23(12)
C(36)-P(5)-C(30)	103.84(11)
C(24)-P(5)-Ru(1)	120.60(8)
C(36)-P(5)-Ru(1)	113.18(8)
C(30)-P(5)-Ru(1)	111.26(9)
C(1)-S(1)-Ru(1)	107.04(9)
C(2)-S(2)-Ru(1)	106.07(9)
C(5)-Ru(1)-S(1)	118.06(8)
C(5)-Ru(1)-S(2)	101.10(8)
S(1)-Ru(1)-S(2)	85.16(3)
C(5)-Ru(1)-P(5)	91.89(8)
S(1)-Ru(1)-P(5)	149.62(2)
S(2)-Ru(1)-P(5)	84.04(3)
C(5)-Ru(1)-P(4)	89.36(8)
S(1)-Ru(1)-P(4)	85.75(3)
S(2)-Ru(1)-P(4)	168.52(2)
P(5)-Ru(1)-P(4)	100.47(3)

Table 5.7 Crystal data and structure refinement for $Ru(S_2C_4F_6)(PPh_3)_2(CO_{equitorial})$.

Empirical formula	$C_{41}H_{30}F_6OP_2RuS_2$	
Formula weight	879.78	
Temperature	100(2) K	
Wavelength	1.54184 Å	
Crystal system	Monoclinic	
Space group	$C_{2/c}$	
Unit cell dimensions	a = 38.777(2) Å	α= 90°.
	b = 10.0596(7) Å	β= 118.678(2)°.
	c = 21.6413(14) Å	γ = 90°.
Volume	7406.4(8) $Å^3$	
Z	8	
Density (calculated)	1.578 Mg/m^3	
Absorption coefficient	5.854 mm^{-1}	
F(000)	3552	
Crystal size	0.18 x 0.14 x 0.09 mm^3	
Crystal color/habit	purple plate	
Theta range for data collection	4.58 to 66.59°.	
Index ranges	-45<=h<=46, -8<=k<=11, -24<=l<=25	
Reflections collected	23043	
Independent reflections	6405 [R(int) = 0.0307]	
Completeness to theta = 66.59°	98.0 %	
Absorption correction Semi-empirical		
from equivalents		
Max. and min. transmission	0.6209 and 0.4188	

Table 5.7 Crystal data and structure refinement for $Ru(S_2C_4F_6)(PPh_3)_2(CO_{equitorial})$, continued.

Refinement method	Full-matrix least-squares on F2
Data / restraints / parameters	6405 / 0 / 478
Goodness-of-fit on F2	1.019
Final R indices [I>2sigma(I)]	R1 = 0.0227, wR2 = 0.0543
R indices (all data)	R1 = 0.0264, wR2 = 0.0560
Largest diff. peak and hole	0.329 and -0.545 e.Å^{-3}

Table 5.8 Bond lengths [Å] and angles [°] for $Ru(S_2C_4F_6)(PPh_3)_2(CO_{equitorial})$.

C(1)-C(2)	1.355(3)
C(1)-C(3)	1.504(3)
C(1)-S(1)	1.7316(19)
C(2)-C(4)	1.512(3)
C(2)-S(2)	1.725(2)
C(3)-F(2)	1.330(2)
C(3)-F(1)	1.337(3)
C(3)-F(3)	1.351(2)
C(4)-F(6)	1.334(3)
C(4)-F(4)	1.339(3)
C(4)-F(5)	1.350(3)
C(5)-O(1)	1.149(2)
C(5)-Ru(1)	1.873(2)
C(6)-C(7)	1.395(3)
C(6)-C(11)	1.396(3)

Table 5.8 Bond lengths [Å] and angles [°] for $Ru(S_2C_4F_6)(PPh_3)_2(CO_{equitorial})$, continued.

C(6)-P(1)	1.841(2)
C(7)-C(8)	1.389(3)
C(7)-H(7)	0.9500
C(8)-C(9)	1.383(4)
C(8)-H(8)	0.9500
C(9)-C(10)	1.380(4)
C(9)-H(9)	0.9500
C(10)-C(11)	1.390(3)
C(10)-H(10)	0.9500
C(11)-H(11)	0.9500
C(12)-C(13)	1.395(3)
C(12)-C(17)	1.401(3)
C(12)-P(1)	1.827(2)
C(13)-C(14)	1.382(3)
C(13)-H(13)	0.9500
C(14)-C(15)	1.384(3)
C(14)-H(14)	0.9500
C(15)-C(16)	1.382(4)
C(15)-H(15)	0.9500
C(16)-C(17)	1.382(3)
C(16)-H(16)	0.9500
C(17)-H(17)	0.9500
C(18)-C(23)	1.393(3)
C(18)-C(19)	1.397(3)
C(18)-P(1)	1.822(2)

Table 5.8 Bond lengths [Å] and angles [°] for $Ru(S_2C_4F_6)(PPh_3)_2(CO_{equitorial})$, continued.

C(19)-C(20)	1.389(3)
C(19)-H(19)	0.9500
C(20)-C(21)	1.371(4)
C(20)-H(20)	0.9500
C(21)-C(22)	1.383(4)
C(21)-H(21)	0.9500
C(22)-C(23)	1.392(3)
C(22)-H(22)	0.9500
C(23)-H(23)	0.9500
C(24)-C(25)	1.390(3)
C(24)-C(29)	1.389(3)
C(24)-P(2)	1.831(2)
C(25)-C(26)	1.386(3)
C(25)-H(25)	0.9500
C(26)-C(27)	1.387(3)
C(26)-H(26)	0.9500
C(27)-C(28)	1.378(3)
C(27)-H(27)	0.9500
C(28)-C(29)	1.388(3)
C(28)-H(28)	0.9500
C(29)-H(29)	0.9500
C(30)-C(35)	1.390(3)
C(30)-C(31)	1.397(3)
C(30)-P(2)	1.833(2)
C(31)-C(32)	1.383(3)

Table 5.8 Bond lengths [Å] and angles [°] for $Ru(S_2C_4F_6)(PPh_3)_2(CO_{equitorial})$, continued.

C(31)-H(31)	0.9500
C(32)-C(33)	1.385(4)
C(32)-H(32)	0.9500
C(33)-C(34)	1.375(4)
C(33)-H(33)	0.9500
C(34)-C(35)	1.387(3)
C(34)-H(34)	0.9500
C(35)-H(35)	0.9500
C(36)-C(37)	1.380(3)
C(36)-C(41)	1.384(3)
C(36)-P(2)	1.826(2)
C(37)-C(38)	1.393(3)
C(37)-H(37)	0.9500
C(38)-C(39)	1.374(3)
C(38)-H(38)	0.9500
C(39)-C(40)	1.377(3)
C(39)-H(39)	0.9500
C(40)-C(41)	1.388(3)
C(40)-H(40)	0.9500
C(41)-H(41)	0.9500
P(1)-Ru(1)	2.2911(5)
P(2)-Ru(1)	2.3691(5)
S(1)-Ru(1)	2.2949(5)
S(2)-Ru(1)	2.3115(5)

Table 5.8 Bond lengths [Å] and angles [°] for $Ru(S_2C_4F_6)(PPh_3)_2(CO_{equitorial})$, continued.

C(2)-C(1)-C(3)	126.49(18)
C(2)-C(1)-S(1)	121.33(16)
C(3)-C(1)-S(1)	112.01(14)
C(1)-C(2)-C(4)	123.99(18)
C(1)-C(2)-S(2)	120.91(15)
C(4)-C(2)-S(2)	115.10(15)
F(2)-C(3)-F(1)	105.97(18)
F(2)-C(3)-F(3)	105.93(17)
F(1)-C(3)-F(3)	105.91(17)
F(2)-C(3)-C(1)	115.62(17)
F(1)-C(3)-C(1)	111.96(17)
F(3)-C(3)-C(1)	110.80(18)
F(6)-C(4)-F(4)	105.97(17)
F(6)-C(4)-F(5)	105.86(17)
F(4)-C(4)-F(5)	107.10(17)
F(6)-C(4)-C(2)	112.56(18)
F(4)-C(4)-C(2)	112.93(18)
F(5)-C(4)-C(2)	111.93(17)
O(1)-C(5)-Ru(1)	171.10(18)
C(7)-C(6)-C(11)	118.72(19)
C(7)-C(6)-P(1)	120.45(16)
C(11)-C(6)-P(1)	120.82(16)
C(8)-C(7)-C(6)	120.5(2)
C(8)-C(7)-H(7)	119.8
C(6)-C(7)-H(7)	119.8

Table 5.8 Bond lengths [Å] and angles [°] for $Ru(S_2C_4F_6)(PPh_3)_2(CO_{equitorial})$, continued.

C(9)-C(8)-C(7)	120.3(2)
C(9)-C(8)-H(8)	119.9
C(7)-C(8)-H(8)	119.9
C(10)-C(9)-C(8)	119.8(2)
C(10)-C(9)-H(9)	120.1
C(8)-C(9)-H(9)	120.1
C(9)-C(10)-C(11)	120.4(2)
C(9)-C(10)-H(10)	119.8
C(11)-C(10)-H(10)	119.8
C(10)-C(11)-C(6)	120.3(2)
C(10)-C(11)-H(11)	119.8
C(6)-C(11)-H(11)	119.8
C(13)-C(12)-C(17)	118.8(2)
C(13)-C(12)-P(1)	118.08(16)
C(17)-C(12)-P(1)	122.46(16)
C(14)-C(13)-C(12)	120.7(2)
C(14)-C(13)-H(13)	119.7
C(12)-C(13)-H(13)	119.7
C(15)-C(14)-C(13)	120.1(2)
C(15)-C(14)-H(14)	120.0
C(13)-C(14)-H(14)	120.0
C(14)-C(15)-C(16)	119.8(2)
C(14)-C(15)-H(15)	120.1
C(16)-C(15)-H(15)	120.1

Table 5.8 Bond lengths [Å] and angles [°] for $Ru(S_2C_4F_6)(PPh_3)_2(CO_{equitorial})$, continued.

C(17)-C(16)-C(15)	120.7(2)
C(17)-C(16)-H(16)	119.7
C(15)-C(16)-H(16)	119.7
C(16)-C(17)-C(12)	120.0(2)
C(16)-C(17)-H(17)	120.0
C(12)-C(17)-H(17)	120.0
C(23)-C(18)-C(19)	118.9(2)
C(23)-C(18)-P(1)	119.88(17)
C(19)-C(18)-P(1)	121.25(17)
C(20)-C(19)-C(18)	120.4(2)
C(20)-C(19)-H(19)	119.8
C(18)-C(19)-H(19)	119.8
C(21)-C(20)-C(19)	120.3(3)
C(21)-C(20)-H(20)	119.8
C(19)-C(20)-H(20)	119.8
C(20)-C(21)-C(22)	120.0(2)
C(20)-C(21)-H(21)	120.0
C(22)-C(21)-H(21)	120.0
C(21)-C(22)-C(23)	120.4(2)
C(21)-C(22)-H(22)	119.8
C(23)-C(22)-H(22)	119.8
C(18)-C(23)-C(22)	120.0(2)
C(18)-C(23)-H(23)	120.0
C(22)-C(23)-H(23)	120.0

Table 5.8 Bond lengths [Å] and angles [°] for $Ru(S_2C_4F_6)(PPh_3)_2(CO_{equitorial})$, continued.

C(25)-C(24)-C(29)	118.76(19)
C(25)-C(24)-P(2)	118.62(15)
C(29)-C(24)-P(2)	122.58(16)
C(26)-C(25)-C(24)	120.4(2)
C(26)-C(25)-H(25)	119.8
C(24)-C(25)-H(25)	119.8
C(25)-C(26)-C(27)	120.3(2)
C(25)-C(26)-H(26)	119.8
C(27)-C(26)-H(26)	119.8
C(28)-C(27)-C(26)	119.6(2)
C(28)-C(27)-H(27)	120.2
C(26)-C(27)-H(27)	120.2
C(27)-C(28)-C(29)	120.2(2)
C(27)-C(28)-H(28)	119.9
C(29)-C(28)-H(28)	119.9
C(28)-C(29)-C(24)	120.7(2)
C(28)-C(29)-H(29)	119.6
C(24)-C(29)-H(29)	119.6
C(35)-C(30)-C(31)	118.5(2)
C(35)-C(30)-P(2)	121.33(16)
C(31)-C(30)-P(2)	120.20(16)
C(32)-C(31)-C(30)	120.6(2)
C(32)-C(31)-H(31)	119.7
C(30)-C(31)-H(31)	119.7
C(31)-C(32)-C(33)	120.1(2)

Table 5.8 Bond lengths [Å] and angles [°] for $Ru(S_2C_4F_6)(PPh_3)_2(CO_{equitorial})$, continued.

C(31)-C(32)-H(32)	120.0
C(33)-C(32)-H(32)	120.0
C(34)-C(33)-C(32)	120.0(2)
C(34)-C(33)-H(33)	120.0
C(32)-C(33)-H(33)	120.0
C(33)-C(34)-C(35)	120.1(2)
C(33)-C(34)-H(34)	120.0
C(35)-C(34)-H(34)	120.0
C(34)-C(35)-C(30)	120.8(2)
C(34)-C(35)-H(35)	119.6
C(30)-C(35)-H(35)	119.6
C(37)-C(36)-C(41)	119.22(19)
C(37)-C(36)-P(2)	123.57(16)
C(41)-C(36)-P(2)	117.13(16)
C(36)-C(37)-C(38)	119.9(2)
C(36)-C(37)-H(37)	120.1
C(38)-C(37)-H(37)	120.1
C(39)-C(38)-C(37)	120.7(2)
C(39)-C(38)-H(38)	119.7
C(37)-C(38)-H(38)	119.7
C(38)-C(39)-C(40)	119.6(2)
C(38)-C(39)-H(39)	120.2
C(40)-C(39)-H(39)	120.2
C(39)-C(40)-C(41)	120.0(2)
C(39)-C(40)-H(40)	120.0

Table 5.8 Bond lengths [Å] and angles [°] for $Ru(S_2C_4F_6)(PPh_3)_2(CO_{equitorial})$, continued.

C(41)-C(40)-H(40)	120.0
C(36)-C(41)-C(40)	120.6(2)
C(36)-C(41)-H(41)	119.7
C(40)-C(41)-H(41)	119.7
C(18)-P(1)-C(12)	103.70(10)
C(18)-P(1)-C(6)	102.71(9)
C(12)-P(1)-C(6)	100.88(9)
C(18)-P(1)-Ru(1)	118.84(7)
C(12)-P(1)-Ru(1)	117.16(7)
C(6)-P(1)-Ru(1)	111.19(7)
C(36)-P(2)-C(24)	103.51(9)
C(36)-P(2)-C(30)	103.75(9)
C(24)-P(2)-C(30)	100.77(9)
C(36)-P(2)-Ru(1)	113.71(6)
C(24)-P(2)-Ru(1)	123.27(7)
C(30)-P(2)-Ru(1)	109.56(7)
C(1)-S(1)-Ru(1)	105.66(7)
C(2)-S(2)-Ru(1)	105.50(7)
C(5)-Ru(1)-P(1)	92.86(6)
C(5)-Ru(1)-S(1)	155.39(6)
P(1)-Ru(1)-S(1)	111.558(19)
C(5)-Ru(1)-S(2)	89.00(6)
P(1)-Ru(1)-S(2)	94.739(18)
S(1)-Ru(1)-S(2)	86.049(17)
C(5)-Ru(1)-P(2)	93.03(6)

Table 5.8 Bond lengths [Å] and angles [°] for $Ru(S_2C_4F_6)(PPh_3)_2(CO_{equitorial})$, continued.

P(1)-Ru(1)-P(2)	104.865(18)
S(1)-Ru(1)-P(2)	83.915(17)
S(2)-Ru(1)-P(2)	160.152(19)

5.11 References

(1) Ito, T.; Hamaguchi, T.; Nagino, H.; Yamaguchi, T.; Washington, J.; Kubiak, C. P. *Science* **1997**, *277*, 660.

(2) Cohen, B.; Weiss, S. *J. Chem. Phys.* **1980**, *72*, 6804.

(3) Grevels, F. W.; Jacke, J.; Klotzbucher, W. E.; Kruger, C.; Seevogel, K.; Tsay, Y. H. *Angew. Chem. Int. Ed.* **1987**, *26*, 885.

(4) Chen, Z.; Strauss, H. L. *J. Chem. Phys.* **1998**, *108*, 5522.

(5) Balch, A. L.; Miller, J. *Inorg. Chem.* **1971**, *10*, 1410.

(6) Hoffman, P. R.; Caulton, K. G. *J. Am. Chem. Soc.* **1975**, *97*, 4221.

(7) Grevels, F. W.; Kerpen, K.; Klotzbucher, W. E.; McClung, R. E. D.; Russell, G.; Viotte, M.; Schaffner, K. *J. Am. Chem. Soc.* **1998**, *120*, 10423.

(8) Macphail, R. A.; Strauss, H. L. *J. Chem. Phys.* **1985**, *82*, 1156.

(9) Turner, J. J. In *Handbook of vibrational spectroscopy*; John Wiley and Sons Ltd. : 2002; Vol. 1, p 101.

(10) Turner, J. J.; Gordon, C. M.; Howdle, S. M. *J. Phys. Chem.* **1995**, *99*, 17532.

(11) Wood, K. A.; Strauss, H. L. *Ber. Bunsen Phys. Chem.* **1989**, *93*, 615.

(12) Wood, K. A.; Strauss, H. L. *J. Phys. Chem.* **1990**, *94*, 5677.

(13) Personal communication with C.B. Harris Group at University of California Berkeley.

(14) Salsman, J. C., UCSD, 2005.

(15) Personal communication with Nien-Hui Ge at UC Irvine, S.

(16) Cervetto, V.; Helbing, J.; Bredenbeck, J.; Hamm, P. *J. Chem. Phys.* **2004**, *121*, 5935.

(17) McClung, R. E. D. In *Program for the simulation of IR spectra of exchanging systems*.

(18) Bernal, I.; Clearfie.A; Epstein, E. F.; Ricci, J. S.; Balch, A.; Miller, J. S. *J. Chem. Soc. Chem. Comm.* **1973**, 39.

(19) Clearfield, A.; Epstein, E. F.; Bernal, I. *J. Coord. Chem.* **1977**, *6*, 227.

(20) Buhl, M.; Thiel, W. *Inorg. Chem.* **1997**, *36*, 2922.

(21) Cahoon, J. F.; Sawyer, K. R.; Schlegel, J. P.; Harris, C. B. *Science* **2008**, *319*, 1820.

(22) Sheldrick, G. M. *Acta Crystallogr A* **2008**, *64*, 112.

(23) te Velde, G.; Bickelhaupt, F. M.; Baerends, E. J.; Fonseca Guerra, C.; van Gisbergen, S. J. A.; Snijders, J. G.; Ziegler, T. *J. Comput. Chem.* **2001**, *22*, 931.

(24) Fonseca Guerra, C.; Snijders, J. G.; te Velde, G.; Baerends, E. J. *Theor. Chem. Acc.* **1998**, *99*, 391.

(25) ADF 2007.01 ed.; SCM, Theoretical Chemistry, Vrije Universitet: Amsterdam, The Netherlands; www.scm.com: 2007.

(26) Vosko, S. H.; Wilk, L.; Nusair, M. *Can. J. Phys.* **1980**, *58*, 1200.

(27) Becke, A. D. *Phys. Rev. A* **1988**, *38*, 3098.

(28) Perdew, J. P. *Phys. Rev. B* **1986**, *34*, 7406.

(29) Perdew, J. P. *Phys. Rev. B* **1986**, *33*, 8822.

(30) Perdew, J. P.; Yue, W. *Phys. Rev. B* **1986**, *33*, 8800.

(31) van Lenthe, E.; Baerends, E. J.; Snijders, J. G. *J. Chem. Phys.* **1993**, 99, 4597.

(32) van Lenthe, E.; Snijders, J. G.; Baerends, E. J. *J. Chem. Phys.* **1996**, *105*, 6505.